UNIVERSITY OF
BIRMINGHAM

Micromachined Coupled Resonator Butler Matrix

Shuli Li

A thesis submitted to the University of Birmingham for the degree of

MASTER OF PHILOSOPHY

School of Electronic, Electrical and Computer Engineering

The University of Birmingham

September 2013

Abstract

This thesis presents the design and characterisation of a micromachined Butler Matrix operating at WR-3 band (220 GHz to 325 GHz). For this thesis a two port Butler matrix is used, here there are two input ports and two output ports. When signal is applied to one of the input ports then it is equally split between the output ports, but has a 90 degree phase shift. In general Butler matrices can have many ports. Conventionally transmission lines are used to make a Butler Matrix but in this thesis, the Butler Matrix is realised only in resonators. This technique is implemented by the appropriate couplings between resonators and the coupling between the resonators and the external ports. The method has the advantage of applying to any type of resonator can be used no matter what its physical structure. SU-8 photoresist micromachining technology is used for fabrication and three metal-coated SU-8 layers are used to implement this micromachined coupled resonator Butler Matrix. The fabrication process was not successful thus no useful measurement results had been made. Low loss bends are designed for the connections between the Butler Matrix and the loads and flanges. A two-element slotted waveguide antenna array is designed to be connected to the Butler Matrix to build a beamforming system and to verify the characterisation of the Butler Matrix.

Acknowledgements

I am extremely grateful for the guidance and support of my supervisor Prof. Mike Lancaster. He gave me many important advice and helpful suggestions during my study. I would also like to express my appreciation to Dr. Paul Smith and Dr. Fred Huang for their useful advice.

Many thanks for Dr. Yingtao Tian for the fabrication of the micromachined waveguide device and Dr. Xiaobang Shang for his help during the measurements. I am also grateful to Xianyue Wu for his help in the antenna design.

Thanks to my colleagues for their support and friendship in the Emerging Device Technology Research Group at the University of Birmingham. Finally, my sincere gratitude goes to my parents for their invaluable support and encouragement.

Table of Contents

Chapter 7 Micromachined Butlter Matrix with Antenna Arrays

Chapter 8 Conclustions and Future Work

Chapter 1 Introduction

1.1 Overview of the Background

There is a growing interest in the terahertz electromagnetic systems (from 100 GHz to 10 THz). This is a frequency range lies in the boundary region between radio waves and light. The terahertz waves have the characteristics as they could pass through many materials (e.g., thin plastic, a piece of paper and a thin layer of oil) and have a large absorption capability. Due to these characteristics, a large variety of applications, such as medical examinations, biometric security, and ultrafast wireless communication systems are expected to develop [1]. As the operating frequency goes higher, conventional machining technology based on milling, cutting and drilling is not sufficient for the comparatively small structures due to the limitation of the size of the machining tools. Also, the standard photolithographic technology developed for micro-electronic and VSDL (very large scale integration) circuits cannot generate 3D-structures with sizes up to several hundred microns [2]. Thus, the thick SU-8 photoresist technology is introduced to achieve high precision in fabricating small components for high-frequency applications. It has the advantages of high aspect ratio (>15:1), easily processed, relatively low cost with high performance and suitable for volume productions [3]. This project uses SU-8 photoresist technology to produce a micromachined coupled resonator Butler Matrix.

The Butler Matrix (BM) is a very attractive network recently used in microwave electronics. It is a beamforming network composed of microwave hybrids, crossovers and phase shifters. In general, the input power will be equally divided at the output, and the phase shift between adjacent output ports should be the same. By choosing different input port, the value of phase shift of output port varies [4]. The Butler Matrix is so widely used due to its ability to form orthogonal beams to increase the channel capacity limited by interference [5] and is easy to realize for its simple structure [6]. These unique properties of Butler Matrix result in a broad range of their applications in modern-day communications: such as beamforming networks with multibeam antennas [7-8], multichannel amplifiers [9-10], or systems for direction finding [11].

1.2 Objective of the Project

This project aims to study and implement a WR-3 band 2x2 Butler Matrix feeding a slotted waveguide (WG) antenna array. A schematic diagram of the Butler Matrix is shown in Figure 1.1 (a). The Butler Matrix will deliver two output signals with the same magnitude but a phase shift of ±90 degree by feeding the signal in different input ports (port 1 and port 4 in Figure 1.1 (a)). The whole structure is constructed by one 90 degree hybrid coupler and a two-element slotted waveguide antenna array. It is to be fabricated on metal-coated SU-8 thick resist and is designed to be built by three layers of SU-8. Such an assembly for the Butler Matrix is illustrated in Figure 1.1 (b).

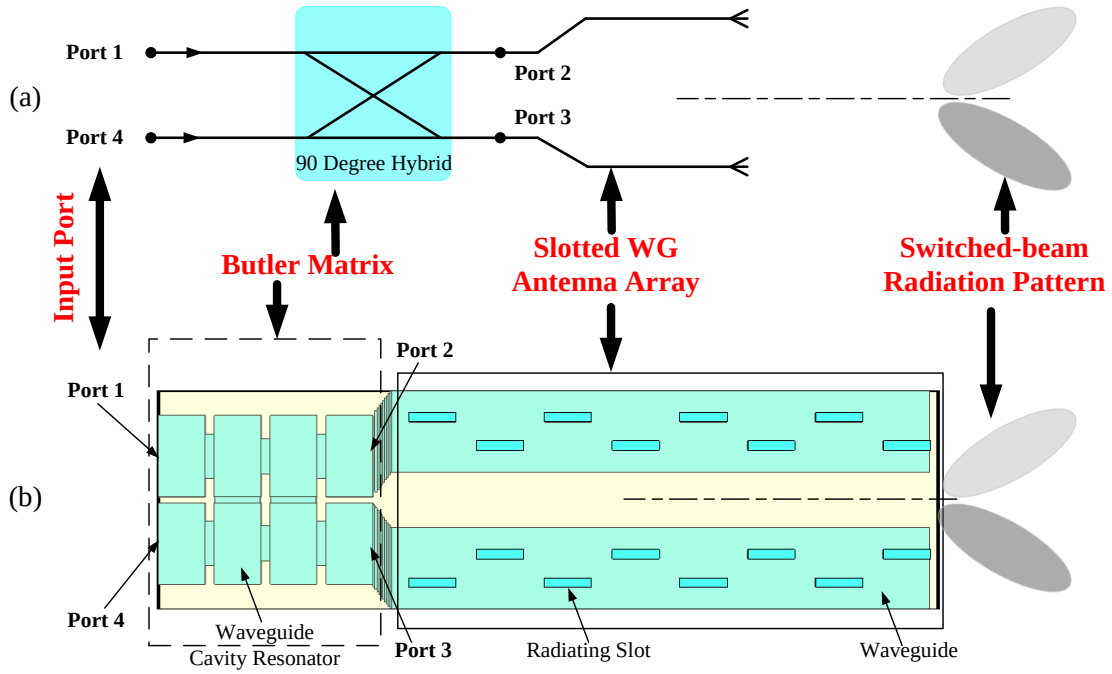

Figure 1.1 (a) the Schematic Diagram for a 2x2 Butler Matrix

(b) Assembly of the 2x2 Butler Matrix feeding a 2-element Slotted Waveguide Antenna Array

The antenna has been realized by slotted waveguide antenna array. This antenna array structure has two elements that are spaced by λ_0 at 270 GHz in order to fit the WR-3 band waveguide

dimensions and get orthogonal beams at the same time. The hybrid coupler shown in Figure 1.1 (b) is based on four waveguide cavity resonators coupled together.

1.3 Structure of the Thesis

The thesis contains nine chapters, while it can be divided into three major parts, which are resonator design, waveguide design and antenna design. The first three chapters explain a new method which is based on coupled resonator structure to implement a 90 degree hybrid coupler. Chapter four to Chapter six present the waveguide implementation of such a proposed structure. Chapter seven and Chapter eight provide the design of a micromachined slotted waveguide antenna array connected with the Butler Matrix. The details of what each chapter presents will be given below.

Chapter two gives an overview of the 90 degree hybrid coupler and some of its applications. An overview of how the coupled resonator structure being implemented in various types of microwave devices, such as filters, diplexers and the Butler Matrix is also discussed. This chapter also gives some examples of the Butler Matrix, already designed and demonstrated, using the micromachined rectangular coaxial cable at a frequency of about 60 GHz.

In Chapter three, the design of the coupled resonator hybrid coupler is presented. The coupling matrix concept is explained in detail. The coupling coefficients and external quality factors are derived and calculated in theory, and the scattering parameters of this coupled resonator 90 degree hybrid coupler are theoretically plotted for fractional bandwidths ranging from 5% to 1.5%.

Chapter four presents the waveguide implementation of the coupled resonator 90 degree hybrid coupler in WR-3 band. The waveguide cavity resonator is briefly introduced, and the methods of extraction of coupling coefficients and external quality factors for this kind of structure are provided in details. Final optimised results are compared with the theoretical calculations in Chapter three for analysis.

In Chapter five, the thick SU-8 photo-resist micromachining technology is introduced. The purpose of the bend design and the realization of the Butler Matrix with bends are explained in detail. The manufacturing process of the Butler Matrix is presented in general, and the measurements are taken. The results are compared with theoretical predictions as well as the simulations for analysis.

Chapter six deals with the design of micromachined slotted waveguide antenna array, the principles of slot radiators and the realisation of a waveguide antenna by these slot radiators. Dimensions of the slot radiators are calculated from theory at first. After this, the calculated results are treated as initial values in CST Microwave Studio for further optimisation. The optimised S_{11} parameter and 3D version of the radiation pattern are discussed.

Chapter seven presents the assembly of the beamforming network with antenna array. This network has been designed to fit for the WR-3 band waveguide dimensions. Thus, the ideal distance, which is half wavelength between the antennas, cannot be reached. Undesirable high-level sidelobes are introduced. Methods of sidelobe reduction are taken into consideration and are discussed in detail. The improved radiation patterns with the antenna array are plotted.

Chapter eight gives the conclusion of all the work done in this thesis. Some suggestions of future work in this project are listed.

Chapter 2 Literature review

2.1 Overview of the Directional Couplers

The directional coupler is a four port microwave network which delivers power from any port to the other three. The power flow can be represented by a diagram shown in Figure 2.1. From this figure, we can see that power incident into port 1 is coupled to port 2 and port 3. In the same way, power entering into port 4 is apportioned between port 2 and port 3. Making port 1 and port 4 uncoupled. Similarly, port 2 and port 3 are also uncoupled.

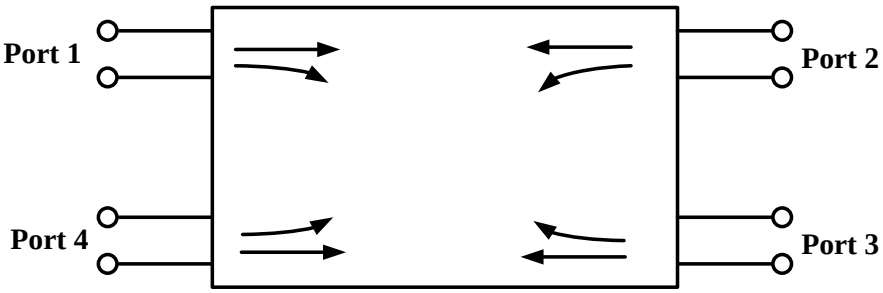

Figure 2.1 Diagram of the Directional Coupler

The scattering matrix [12] of such kind of device has the following properties:

$$S_{11} = S_{22} = S_{33} = S_{44} = 0 \tag{2.1}$$

$$S_{14} = S_{23} = 0 \tag{2.2}$$

The directional coupler is a reciprocal network (no active devices, plasmas or ferrites), therefore the scattering matrix should be a symmetrical and a unitary matrix [12], having the following form:

$$[S] = \begin{bmatrix} 0 & S_{12} & S_{13} & 0 \\ S_{12} & 0 & 0 & S_{24} \\ S_{13} & 0 & 0 & S_{34} \\ 0 & S_{24} & S_{34} & 0 \end{bmatrix} \tag{2.3}$$

Considering this is an ideal lossless network, the scattering matrix should have the following properties [13]:

$$\sum_{n=1}^{4} S_{nj} S_{nj}^{*} = 1 \quad (j=1, 2, 3, 4) \tag{2.4}$$

$$\sum_{n=1}^{4} S_{nj} S_{nk}^{*} = 0 \; (j, k=1,2,3,4; j \neq k) \tag{2.5}$$

The self-product of the rows of such a unitary scattering matrix will yield the following equations:

$$|S_{12}|^2 + |S_{13}|^2 = 1 \tag{2.6 a}$$

$$|S_{12}|^2 + |S_{24}|^2 = 1 \tag{2.6 b}$$

$$|S_{13}|^2 + |S_{34}|^2 = 1 \tag{2.6 c}$$

$$|S_{24}|^2 + |S_{34}|^2 = 1 \tag{2.6 d}$$

So that $|S_{13}| = |S_{24}|$ and $|S_{12}| = |S_{34}|$.

Selecting terminal planes at port 1 and port 4, so that S_{12} and S_{34} have zero phase, gives:

$$S_{12} = S_{34} = k_1 \tag{2.7}$$

In which, k_1 is a real positive number.

From Equation (2.5), choose $j = 1$ and $k = 4$ to get the following equation,

$$\sum_{n=1}^{4} S_{n1} S_{n4}^{*} = S_{12}^{*} S_{24} + S_{13}^{*} S_{34} = k_1 (S_{24} + S_{13}^{*}) = 0 \tag{2.8}$$

We set $S_{13} = k_2 e^{j\theta}$, with k_2 also a pure real positive number, for a 90 degree hybrid coupler, the phase constant of θ should be $\pi/2$, then Equation (2.8) implies that

$$S_{13} = S_{24} = k_2 e^{j\theta} = jk_2 \tag{2.9}$$

The 90 degree hybrid coupler is a special case of the directional coupler, which has the characteristic that power is equally divided at port 2 and port 3, making the coupling factor 3dB. The coupling factor can be derived from the equation below [12]:

$$Coupling = C = 10 \log \frac{P_1}{P_3} = -20 \log k_2 \; dB \tag{2.10}$$

This implies that $k_2 = 1/\sqrt{2}$, from Equation (2.6 a), the relationship between k_1 and k_2 should be

$$k_1^2 + k_2^2 = 1 \tag{2.11}$$

Thus, $k_1 = k_2 = 1/\sqrt{2}$, the [S] matrix has the following form:

$$[S] = \frac{1}{\sqrt{2}} \begin{bmatrix} 0 & 1 & j & 0 \\ 1 & 0 & 0 & j \\ j & 0 & 0 & 1 \\ 0 & j & 1 & 0 \end{bmatrix} \tag{2.12}$$

This scattering matrix indicates that the 90 degree hybrid has the property of delivering two output signals with same magnitude and 90 degree phase shift, but also implies that it has a high degree of symmetry, since any port can be treated as the input port, the output ports will always be the following two ports in the clockwise direction, the remaining one will be the isolation port.

Most hybrid couplers are composed of either transmission lines or waveguides. For example, the bethe hole coupler, which is coupled by suitable apertures [13] and the branch-line coupler, which can be made by microstrip or stripline, shown in Figure 2.2. It is consisted of four quarter-wavelength transmission lines and the couplings are provided by fringing fields of these transmission lines.

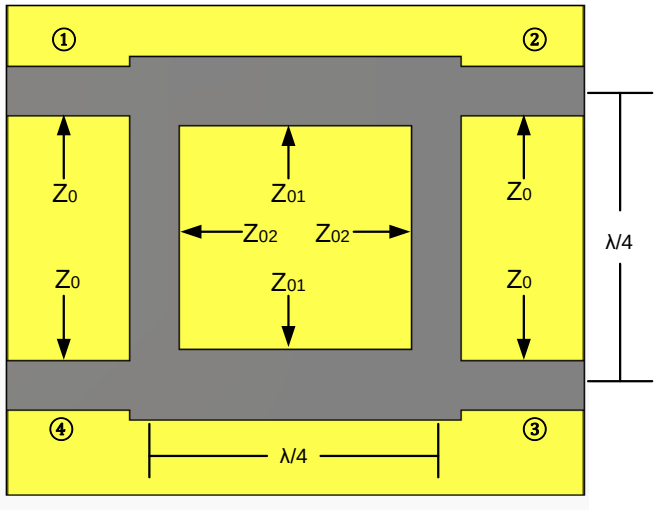

Figure 2.2 Geometry of a Branch-line Coupler

The operation of the branch-line coupler can also be illustrated in terms of phase shift with reference to Figure 2.3. Choosing the signal applied at port 1 as a reference, it is divided equally between port 2 and port 4, leaving a 90 degree phase lag relatively to the reference signal due to the equal quarter-wavelength transmission lines between each port. Then, the signals arrived at port 2 and port 4 will reach port 3 in phase, so that the signal at port 3 is reinforced and having a further 90 degree phase shift compared to the reference signal. In this way, port 2 and port 3 have a phase difference of 90 degree. On the contrary, the signals arrive at port 4 are from port 1 and port 3, which are out of phase. These signals are cancelled by each other, making port 4 an isolated port [29].

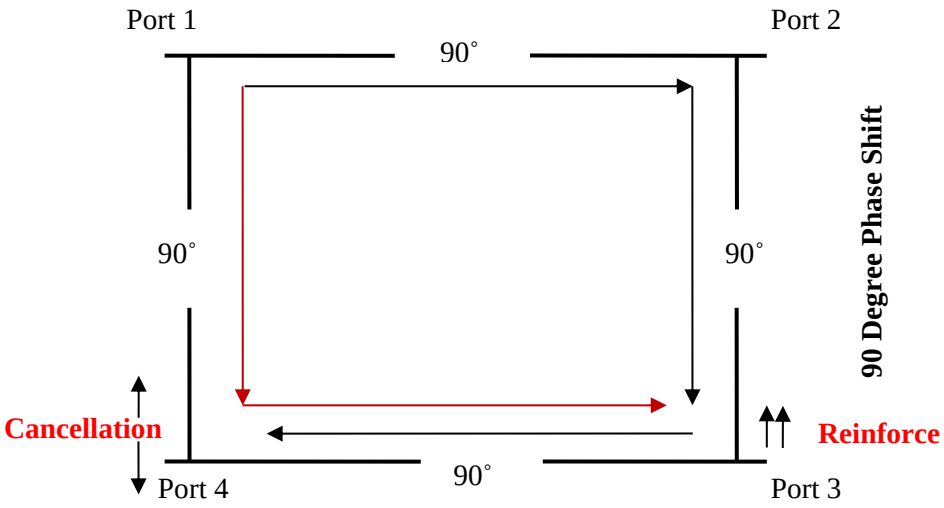

Figure 2.3 Schematic Diagram of Branch-line Coupler in Terms of Phase Shift

Directional couplers have a wide range of applications, such as in power dividers, mixers, and beamforming networks [14-15]. One of the most common applications is the use in multiple beam matrices, such as the Butler Matrix or the Blass Matrix. Here, a more detailed explanation about the Butler Matrix is given. For a standard N x N Butler Matrix, it should have N inputs and N outputs ($N=2^n$, where n is the matrix order). It should be composed of $n \cdot 2^{n-1}$ hybrids and $(n-1) \cdot 2^{n-1}$ phase shifters [6] and the number of crossovers has been reported in [16] as:

$$C_n = 2C_{n-1} + 2^{n-2}(2^{n-2} - 1) \tag{2.13}$$

In which, n should be equal or greater than 2 and $C_1 = 1$.

By applying the signal at each input port, it will produce output signals with equal power but a progressive phase shift compared to the reference port, the phase progression is given by:

$$\delta_i = 2\pi i / N \tag{2.14}$$

For i = ± 1/2, ± 3/2, ± 5/2… ± (N-1)/2.

As a result, the Butler Matrix can produce N orthogonal beams at the outputs when it is connected to the antenna array. Figure 2.4 is the schematic diagram of a 4x4 Butler Matrix with an antenna array.

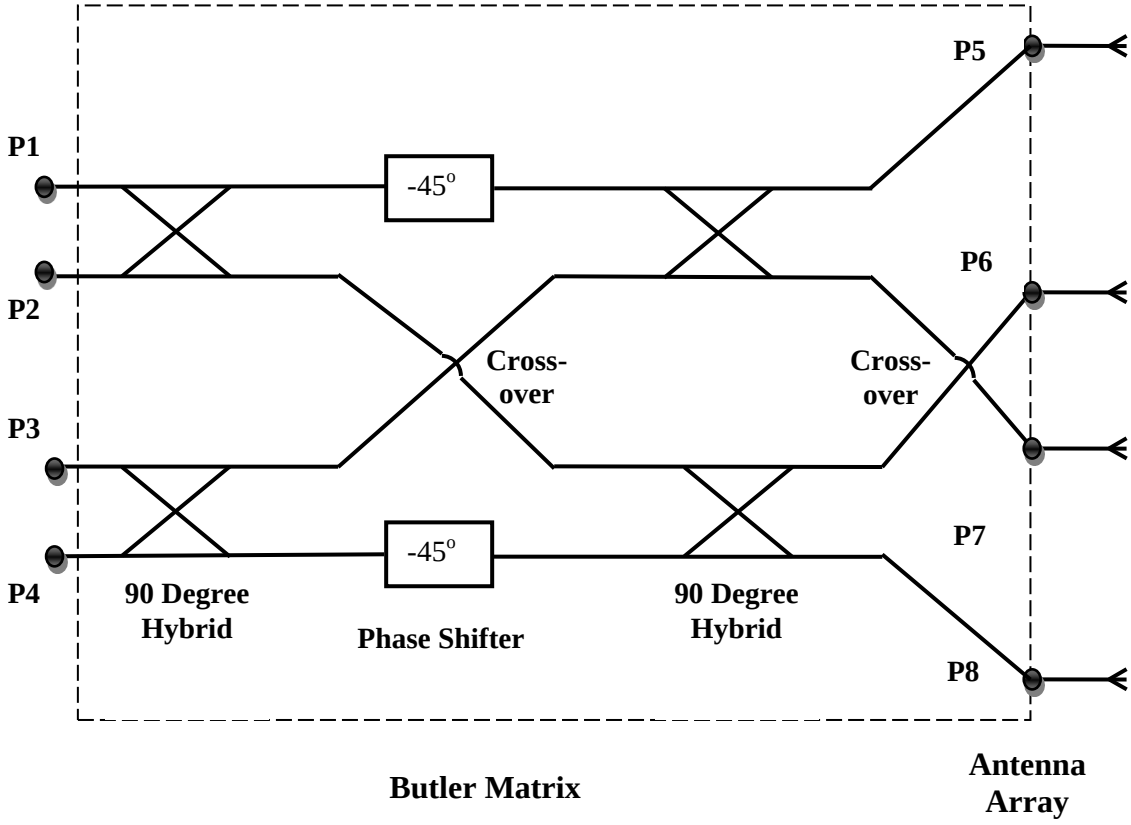

Figure 2.4 Schematic Diagram of a 4x4 Butler Matrix with Antenna Array

2.2 Overview of the Coupled Resonator Circuits

Coupled resonator circuits have an important role in the design of RF and microwave devices. This technology has the advantage that any type of resonator can be used whatever its physical structure is [17]. They have been applied to the design of waveguide filters [18-19], microstrip filters [20-22], multiple passband filters [23], waveguide diplexers [24] and more. These examples are respectively shown in Figure 2.3 (a)-(d).

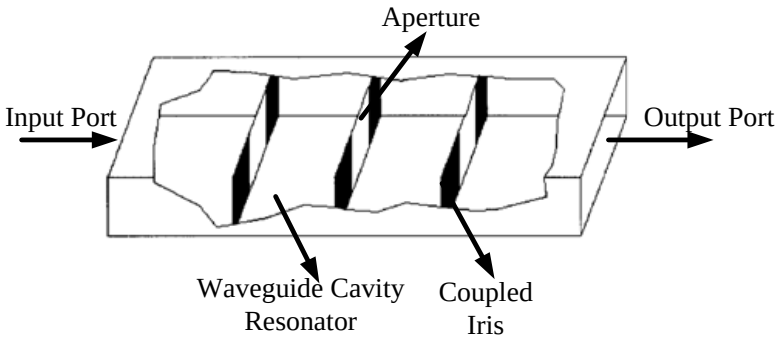
Aperture
Input Port
Output Port
Waveguide Cavity Resonator
Coupled Iris

(a)

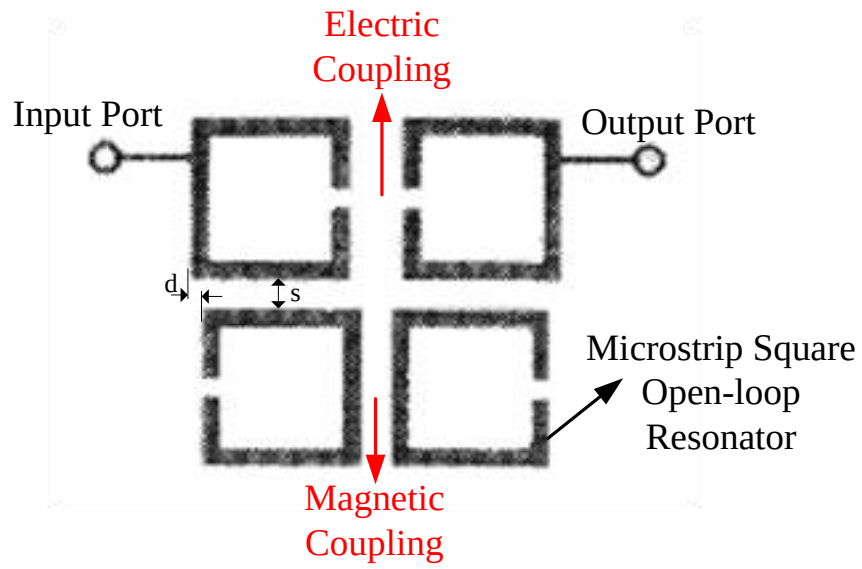
Electric Coupling
Input Port
Output Port
d
s
Microstrip Square Open-loop Resonator
Magnetic Coupling

(b)

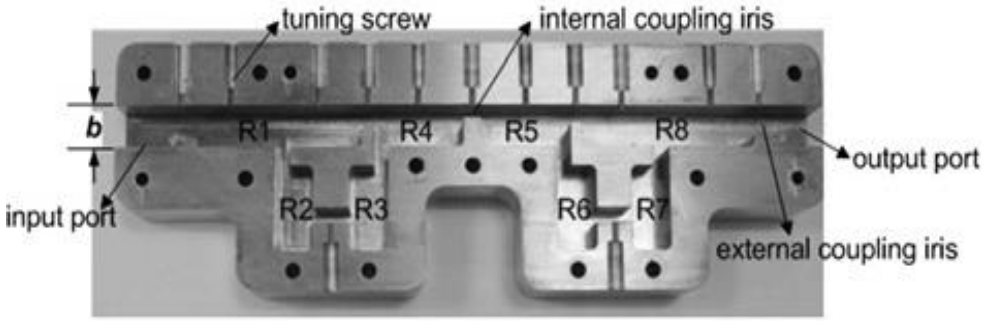
tuning screw
internal coupling iris
b
R1
R4
R5
R8
output port
input port
R2
R3
R6
R7
external coupling iris

(c)

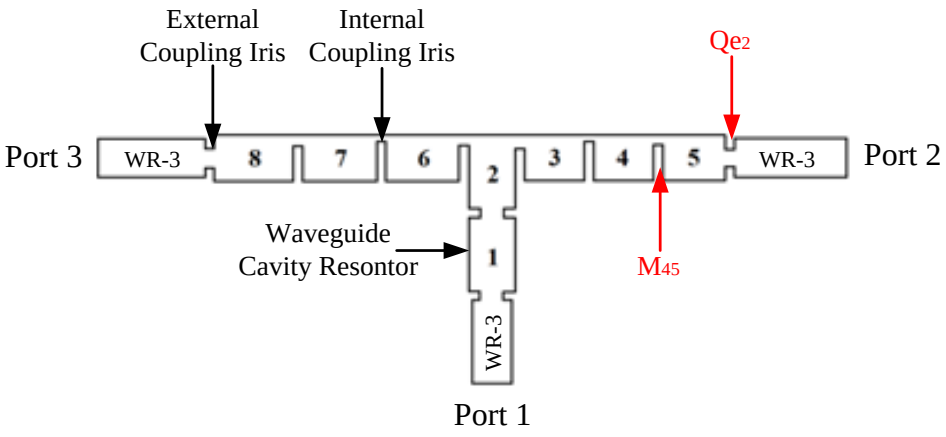

(d)

Figure 2.5 Configurations of Some Coupled Resonator RF and Microwave Devices

(a) Iris Coupled Waveguide Cavity Filter [18]. (b) Microstrip Square Open-Loop Resonator Coupled Filter [20]. (c) Eighth-order Dual-band Filter Coupled by Waveguide Cavity Resonators [23]. (d) Resonator Coupled Waveguide Diplexer [24].

In Figure 2.5 (a), a filter is constructed by coupled waveguide resonators, the resonators are coupled between each other and are coupled to the input and output ports by the apertures of the irises between them. The couplings are determined by the dimensions of these apertures.

Figure 2.5 (b) is the configuration of a planar filter composed of microstrip square open-loop resonators, these resonators are coupled by electric coupling, magnetic coupling or mixed coupling according to the position of the open-gap. The couplings are determined by the spacing s between resonators and are subject to the offset d.

In Figure 2.5 (c), an eighth-order dual-band filter is comprised of waveguide cavity resonators. It has eight waveguide cavity resonators denoted by R1, R2…R8 in the figure, the internal coupling iris affects the coupling between resonators, while the external coupling iris determines the coupling from external waveguide to the input or output port. The tuning screws are used for tuning the size of apertures during the measurement.

This design method is based on the coupling coefficients between resonators and the external quality factors of the input and output resonators. Take the device in Figure 2.5 (d) as an example. The coupling coefficient is determined by the internal coupling iris, denoted by Mij for the coupling coefficient between resonator i and resonator j. The external quality factor is determined by the external coupling iris between the resonator and I/O port, denoted by Qei for port i.

The most important concept of the coupled-resonator method is the coupling matrix [*m*]. It is generated either by a set of loop equations or a set of node equations [17]. Each element in the coupling matrix represents the coupling coefficient of relevant resonators. The *S* parameters of the proposed device are related to the coupling matrix [*m*] through the following formulas [17]:

$$S_{11} = \pm(1 - \frac{2}{q_{e1}}[A]_{11}^{-1}) \tag{2.15 a}$$

$$S_{21} = \frac{2}{\sqrt{q_{e1}q_{e2}}}[A]_{21}^{-1} \tag{2.15 b}$$

……

$$S_{n1} = \frac{2}{\sqrt{q_{e1}q_{en}}}[A]_{n1}^{-1} \tag{2.15 c}$$

Where [*A*] is the sum of three n x n matrices:

$$[A] = [q] + p[U] - j[m] \tag{2.16}$$

[*U*] is the n x n unit matrix, [*q*] is an n x n matrix with all elements zero except for $q_{11} = 1/q_{e1}$ and $q_{nn} = 1/q_{en}$, in which $q_{ei} = Q_{ei} \cdot FBW$ (*FBW* is the fractional bandwidth), and [*m*] is the coupling matrix. *p* is given by: $p = j\frac{1}{FBW}(\frac{\omega}{\omega_0} - \frac{\omega_0}{\omega})$.

Take an 8-order bandpass filter as an example, the coupling matrix is:

$$[m]=\begin{bmatrix} 0 & 0.80799 & 0 & -0.10066 & 0 & 0 & 0 & 0 \\ 0.80799 & 0 & 0.6514 & 0 & 0 & 0 & 0 & 0 \\ 0 & 0.6514 & 0 & 0.52387 & 0 & 0 & 0 & 0 \\ -0.10066 & 0 & 0.52387 & 0 & 0.53064 & 0 & 0 & 0 \\ 0 & 0 & 0 & 0.53064 & 0 & 0.49184 & 0 & -0.2346 \\ 0 & 0 & 0 & 0 & 0.49184 & 0 & 0.7355 & 0 \\ 0 & 0 & 0 & 0 & 0 & 0.7355 & 0 & 0.77967 \\ 0 & 0 & 0 & 0 & -0.2346 & 0 & 0.77967 & 0 \end{bmatrix} \quad (2.17)$$

The normalised external quality factors are qe_1 = 1.02828, qe_8 = 1.08282, and the fractional bandwidth is *FBW*=7.063%, the centre frequency is at 850 MHz. The *S* parameters of such a device can be plotted from the equations above:

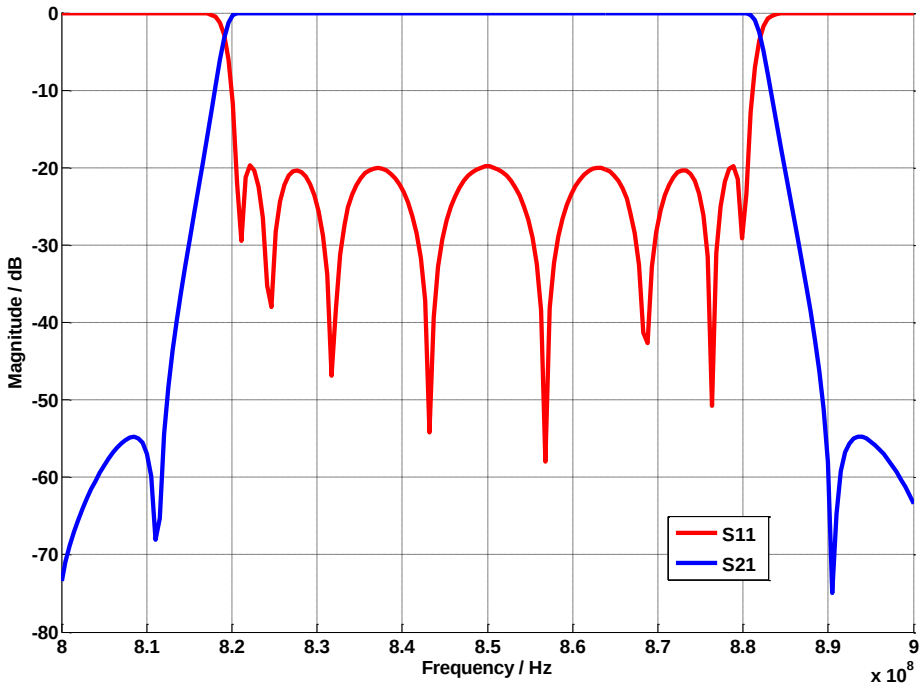

Figure 2.4 Frequency Response of the 8-order Bandpass Filter from Calculation

The coupled resonator method is used in the design of the Butler Matrix here. It is realized by appropriate coupling between the waveguide cavity resonators and the coupling to input and output ports from the external waveguide, which is a new kind of structure for implementing the

Butler Matrix. More details of the extraction of coupling coefficients and the external quality factors will be explained in Chapter 3 and Chapter 4.

2.3 Micromachined Butler Matrix with Antenna Array

There has been considerable researches into the Butler Matrix for wireless local area network (WLAN) applications around 60 GHz [25]. Due to the increased demand of high-speed wireless communications, systems now for higher frequencies are increasingly needed. The Butler Matrix working in the WR-3 frequency band is intended for use in the future, for example, in satellite systems, radio astronomy and others.

A micromachined 2 x 2 Butler Matrix with an antenna array based on a multi-layer structure has been demonstrated in our group [26]. It is made by air filled rectangular coaxial lines. The cross-section of an ideal air filled rectangular coaxial line is shown in Figure 2.5. It is constructed by five layers of gold coated SU-8 with a thickness of 0.2mm.

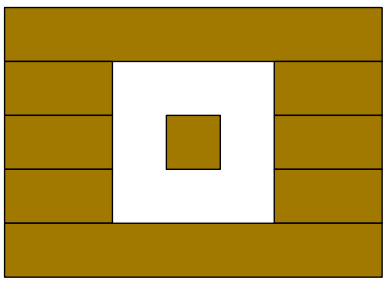

Figure 2.5 Cross-section of an Ideal Air Filled Rectangular Coaxial Line

The whole structure without the top layer that covers the Butler Matrix and the ports is shown in Figure 2.6. The output port of the coupler is connected to a patch antenna by a quarter wavelength transformer with matched impedance. Another 4 x 4 micromachined Butler Matrix operating in Ka-band has been designed based on this model, which is reported in [27].

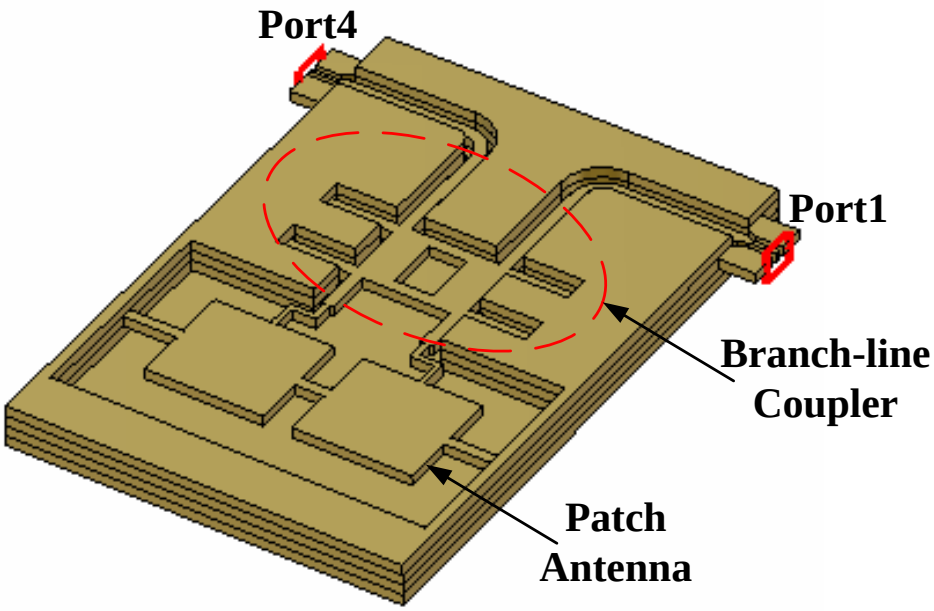

Figure 2.6 Layout of a 2x2 Butler Matrix Realized by Rectangular Coaxial Line

(This figure is reproduced from [26])

However, the design introduced in this thesis is in the frequency range of WR-3 band, much higher than previous designs. The higher frequency will lead to a much smaller size for the whole device; the difficulty of micromachining will increase accordingly. Moreover, it is based on waveguide cavity resonator structure, which is a new concept for Butler Matrix constructed by transmission lines and waveguides. Most importantly, the coupled resonator Butler Matrix fabricated by the SU-8 photo-resist technology is a breakthrough, since it has not been demonstrated before.

Chapter 3

Coupled Resonator 90 Degree Hybrid Coupler Design

3.1 Topology of the Coupled Resonator 90 Degree Hybrid Coupler

The 90 degree hybrid coupler in this design is based on waveguide cavity resonators. It is developed from the conventional branch-line coupler shown in Figure 3.1. The branch-line coupler is consisted of four quarter-wavelength transmission lines, two of which have the characteristic impedance Z_{01}, they are connected with the other two at both ends, which have the characteristic impedance Z_{02}. According to Figure 3.1, the branch-line coupler has four ports; each has the terminal impedance Z_0. By properly choosing the impedance values as: $Z_{01}=0.707Z_0$ and $Z_{02}=Z_0$ separately, this circuit can operate as a 90 degree hybrid coupler with equal power split at ports 2 and 3 [28].

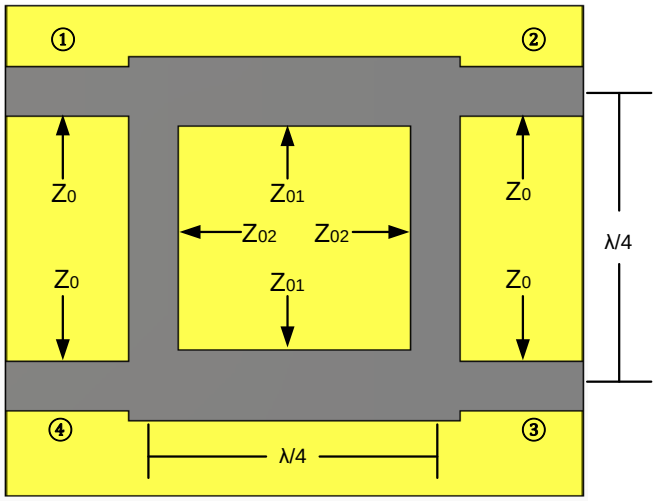

Figure 3.1 Geometry of a Branch-line Coupler

Replacing the quarter-wavelength transmission lines of the branch-line coupler by the couplings between resonators, a resonator based 90 degree hybrid coupler is implemented. Four resonators with appropriate couplings between each other are introduced [30]. The correct external quality factors (Qe) between ports and resonators are taken into consideration. The topology of this

hybrid coupler is shown in Figure 3.2. The circles represent the resonators, while the couplings are depicted by the lines between the circles. By using this technique, the coupling coefficients and quality factors can be changed for different requirements, thus will influence the fractional bandwidth (*FBW*), which is more flexible compared to the conventional branch-line coupler. Moreover, the bandwidth can be improved by increasing the number of resonators according the previous research [30].

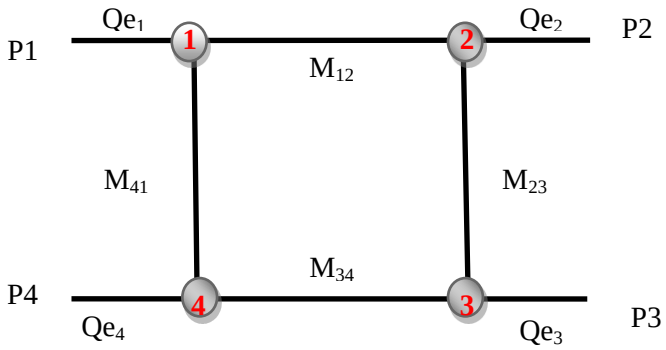

Figure 3.2 Topology of the Coupled Resonator 90 Degree Hybrid Coupler

3.2 Coupled Resonator 90 Degree Hybrid Coupler Design

3.2.1 Extraction of Coupling Coefficients and External Quality Factors

The coupling matrix is derived from basic circuit theories. The equivalent lumped circuit of this branch-line coupler is illustrated in Figure 3.3 [31].

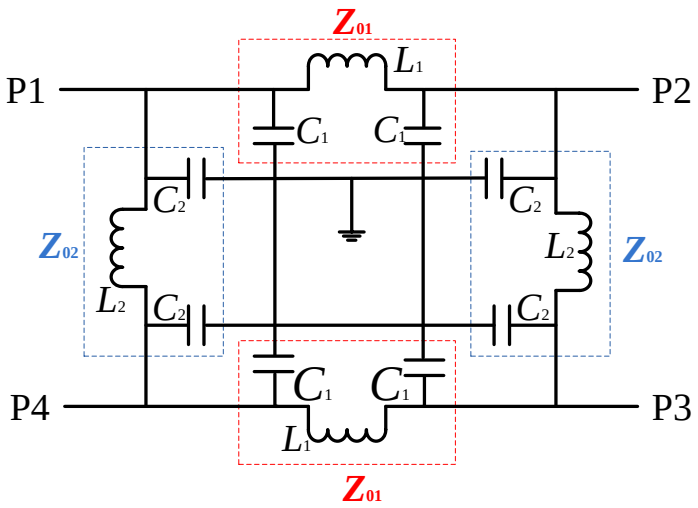

Figure 3.3 Equivalent Circuit of Microstrip Branch-Line Coupler [31]

The values of the inductors and capacitors in Figure 3.3 are given by:

$$L_1 = \frac{Z_{01}}{2\pi f} \qquad C_1 = \frac{1}{Z_{01} \cdot 2\pi f} \tag{3.1 a}$$

$$L_2 = \frac{Z_{02}}{2\pi f} \qquad C_2 = \frac{1}{Z_{02} \cdot 2\pi f} \tag{3.1 b}$$

In which, f is the centre frequency of the branch-line coupler. It is mentioned in chapter 3.1 that $Z_{01}=0.707Z_0$, $Z_{02}=Z_0$. Equation (3.1) can be unified as:

$$L_1 = \frac{Z_0}{\sqrt{2} \cdot 2\pi f} \qquad C_1 = \frac{\sqrt{2}}{Z_0 \cdot 2\pi f} \tag{3.2 a}$$

$$L_2 = \frac{Z_0}{2\pi f} \qquad C_2 = \frac{1}{Z_0 \cdot 2\pi f} \tag{3.2 b}$$

Taking a single branch with characteristic impedance Z_{01} from the hybrid in Figure 3.3, the equivalent circuit of this single quarter-wavelength transmission line is depicted in Figure 3.4. The inductance L_1 and capacitance C_1 can be calculated by Equation (3.1 a).

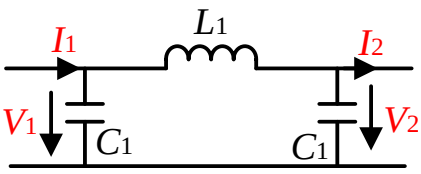

Figure 3.4 the Equivalent Circuit for a Quarter-wavelength Transmission Line

Applying the *ABCD* matrix to the two-port network in Figure 3.4, each element of this matrix can be calculated by [12]:

$$A = \left.\frac{V_1}{V_2}\right|_{I_2=0} = 0 \tag{3.3 a}$$

$$B = \left.\frac{V_1}{I_2}\right|_{V_2=0} = j\omega L_1 \tag{3.3 b}$$

$$C = \left.\frac{I_1}{V_2}\right|_{I_2=0} = j\omega C_1 \tag{3.3 c}$$

$$D = \left.\frac{I_1}{I_2}\right|_{V_2=0} = 0 \tag{3.3 d}$$

At the resonant frequency, the *ABCD* matrix for the circuit in Figure 3.4 has the following form:

$$\begin{bmatrix} A & B \\ C & D \end{bmatrix} = \begin{bmatrix} 0 & j\omega L_1 \\ j\omega C_1 & 0 \end{bmatrix} \tag{3.4}$$

Where ω is the angular frequency at resonant and is equal to $2\pi f$.

The quarter-wavelength transmission line is approximately equivalent to an impedance inverter (*K*-inverter), while the *K* value is relevant to the characteristic impedance of the transmission line [32]. Furthermore, the quarter-wavelength transmission line is taken place by the coupling between resonators. Therefore, the equivalent lumped-element circuit of the coupling between resonator 1 and resonator 2 in Figure 3.2 is given by:

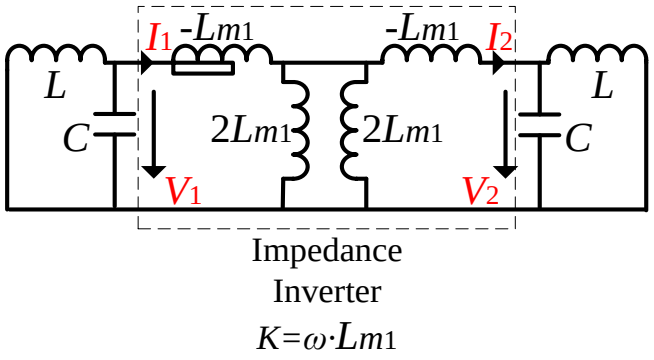

Figure 3.5 Equivalent Lumped-element Circuit for the Coupling between Resonator 1 and 2

L and C are self-inductance and self-capacitance of the resonator. L_{m1} represents the mutual inductance between resonator 1 and 2. The coupling coefficient between these two resonators denoted by kc_1 is defined as [33]:

$$kc_1 = \frac{1}{\omega CK} \tag{3.5}$$

The *ABCD* matrix of Figure 3.5 can be expressed by:

$$\begin{bmatrix} A & B \\ C & D \end{bmatrix} = \begin{bmatrix} 0 & j\omega L_{m1} \\ \dfrac{1}{j\omega L_{m1}} & 0 \end{bmatrix} \tag{3.6}$$

By equating the *ABCD* matrices of the two equivalent circuits, we can get:

$$\begin{bmatrix} A & B \\ C & D \end{bmatrix} = \begin{bmatrix} 0 & j\omega L_1 \\ j\omega C_1 & 0 \end{bmatrix} = \begin{bmatrix} 0 & j\omega L_{m1} \\ \dfrac{1}{j\omega L_{m1}} & 0 \end{bmatrix}$$

Equating each element of the matrices accordingly, gives:

$$j\omega L_1 = j\omega L_{m1} \tag{3.7 a}$$

$$j\omega C_1 = \frac{1}{j\omega L_{m1}} \tag{3.7 b}$$

In this way, we obtain:

$$L_{m1} = L_1 \tag{3.8}$$

Substituting Equation (3.2 a) into Equation (3.8) yields:

$$L_{m1} = L_1 = \frac{Z_0}{\sqrt{2} \cdot 2\pi f} = \frac{Z_0}{\sqrt{2} \cdot \omega} \tag{3.9}$$

Due to the high symmetry property of the hybrid coupler, the coupling coefficient between resonator 1 and resonator 2 is the same as the coupling coefficient between resonator 3 and resonator 4. Similarly, the coupling coefficients between resonator 2 and 3, resonator 4 and 1 are the same (denoted by kc_2). Substituting Equation (3.9) into Equation (3.5) yields:

$$kc_1 = \frac{1}{\omega CK} = \frac{1}{\omega^2 C \cdot L_{m1}} = \frac{\sqrt{2}}{\omega C Z_0} \tag{3.10 a}$$

$$kc_2 = \frac{1}{\omega CK} = \frac{1}{\omega^2 C \cdot L_{m2}} = \frac{1}{\omega C Z_0} \tag{3.10b}$$

The external quality factors can be obtained by the following equation [17]:

$$Q_{ei} = \frac{\omega C}{G_i} = \omega C Z_0 \quad \text{(for } i = 1, 2, 3, 4\text{)} \tag{3.11}$$

3.2.2 Coupling Matrix Representation

Each element in the coupling matrix represents the couplings between resonators. For the topology of the coupled resonator 90 degree hybrid coupler in Figure 3.2, the coupling matrix has the following form:

$$[m] = \begin{bmatrix} M_{11} & M_{12} & M_{13} & M_{14} \\ M_{21} & M_{22} & M_{23} & M_{24} \\ M_{31} & M_{32} & M_{33} & M_{34} \\ M_{41} & M_{42} & M_{43} & M_{44} \end{bmatrix} = \begin{bmatrix} 0 & kc_1 & 0 & kc_2 \\ kc_1 & 0 & kc_2 & 0 \\ 0 & kc_2 & 0 & kc_1 \\ kc_2 & 0 & kc_1 & 0 \end{bmatrix} \tag{3.12}$$

From Chapter 2, the coupling matrix can be used to derive the *S* parameters. From Equation (2.15), the *S* parameters of this coupled resonator 90 degree hybrid can be calculated by:

$$S_{11} = \frac{2}{q_{e1}}[A]_{11}^{-1} - 1 \tag{3.13 a}$$

$$S_{21} = \frac{2}{\sqrt{q_{e1} q_{e2}}} [A]_{21}^{-1} \tag{3.13 b}$$

$$S_{31} = \frac{2}{\sqrt{q_{e1} q_{e3}}} [A]_{31}^{-1} \tag{3.13 c}$$

$$S_{41} = \frac{2}{\sqrt{q_{e1} q_{e4}}} [A]_{41}^{-1} \tag{3.13 d}$$

Where [*A*] is the sum of three n x n matrices:

$$[A] = [q] + p[U] - j[m]$$

[*U*] is the n x n unit matrix, [*q*] is an n x n matrix with all elements zero except for $q_{11} = 1/q_{e1}$ and $q_{nn} = 1/q_{en}$, in which $q_{ei} = Q_{ei} \cdot FBW$ (*FBW* is the fractional bandwidth), and [*m*] is the coupling matrix. *p* is given by: $p = j\frac{1}{FBW}(\frac{\omega}{\omega_0} - \frac{\omega_0}{\omega})$.

The external quality factors are coarsely equal to the inverse of fractional bandwidth (*FBW*) for bandpass filters [32], this is also fit for the coupled resonator 90 degree hybrid, and thus we have:

$$Q_{ei} = \frac{1}{FBW} \tag{3.14}$$

In this design, the fractional bandwidth is chosen to be 5% to fit for the coupling coefficients that could be achieved by the waveguide cavity resonators. The coupling matrix has the following form:

$$[m] == \begin{bmatrix} 0 & kc_1 & 0 & kc_2 \\ kc_1 & 0 & kc_2 & 0 \\ 0 & kc_2 & 0 & kc_1 \\ kc_2 & 0 & kc_1 & 0 \end{bmatrix} = \begin{bmatrix} 0 & 0.0707 & 0 & 0.05 \\ 0.0707 & 0 & 0.05 & 0 \\ 0 & 0.05 & 0 & 0.0707 \\ 0.05 & 0 & 0.0707 & 0 \end{bmatrix}$$

3.3 Theoretical Frequency Response

Figure 3.6 (a) shows the frequency response of this 90 degree hybrid coupler with the centre frequency 270 GHz, and *FBW*=0.05. Figure 3.6 (b) is the phase difference between port 2 and port 3.

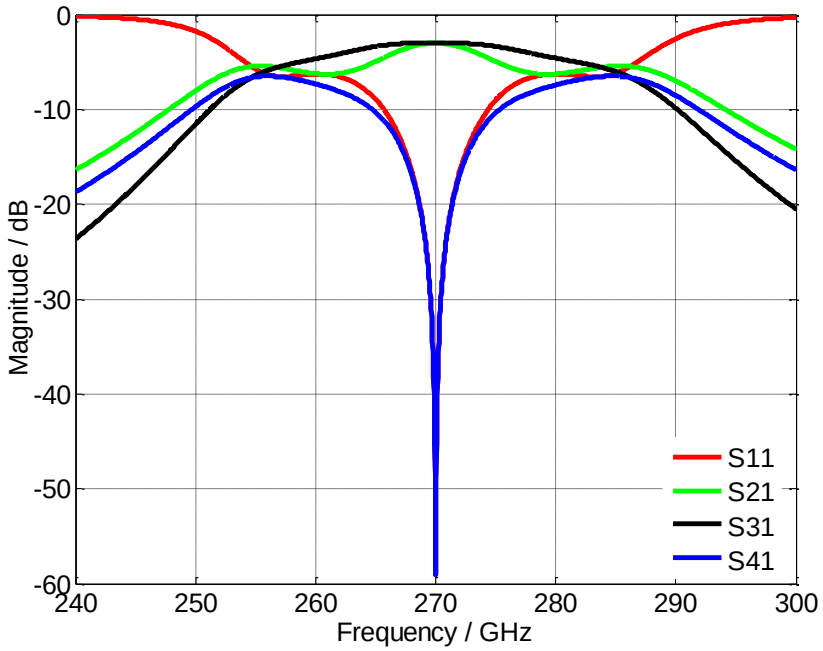

(a)

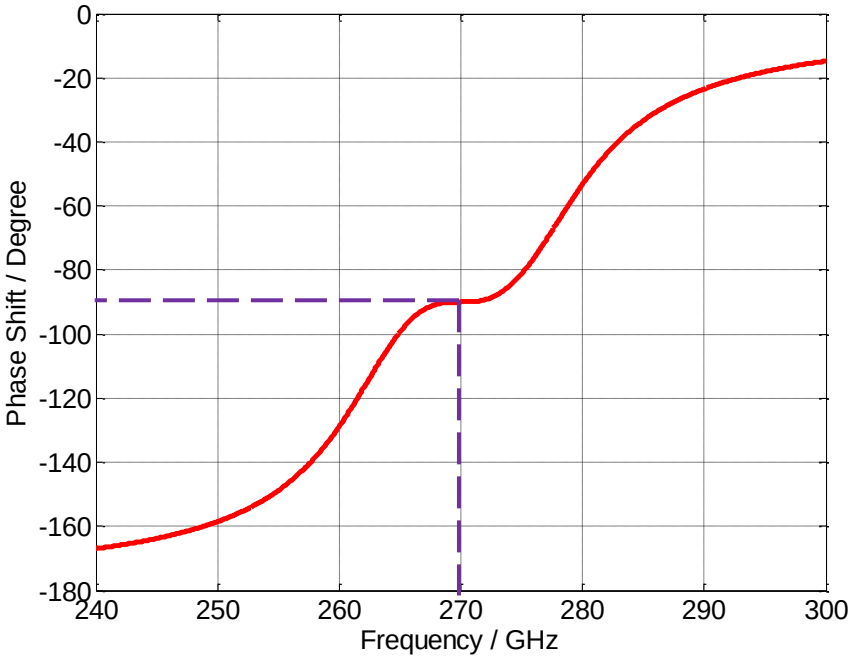

(b)

Figure 3.6 (a) Frequency Response of Magnitude for the 90 Degree Hybrid Coupler calculated from coupling matrix from Theory

(b) Frequency Response of Phase Shift between S_{21} and S_{31} for the 90 Degree Hybrid Coupler

From Figure 3.6 (a) above, S_{21} and S_{31} both reach the magnitude of -3dB at 270 GHz, which meets the requirement of splitting power equally at the centre frequency. Another important property of the 90 degree hybrid coupler is that, the phase shift between two output ports at the centre frequency should be 90 degree. This can be obtained by Figure 3.6 (b).

The coupling matrix is suitable for different bandwidths by calculating the coupling coefficients in the coupling matrix accordingly. Some examples of different bandwidths are taken and the frequency responses and phase shifts are plotted for comparison. The *FBW*s are: 5%, 10% and 15% separately.

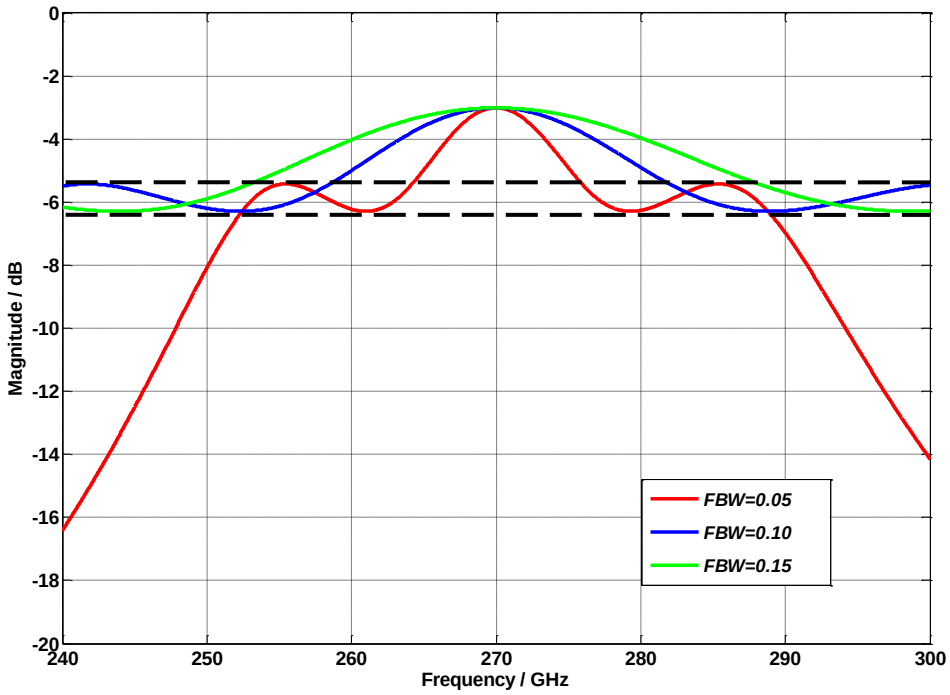

Figure 3.7 the S_{21} Parameter with Different Bandwidths from Theory

Figure 3.7 shows the S_{21} Parameter with different bandwidths for comparison. Here we get, it has one ripple on either side of the centre frequency. However, the ripples have the same amplitude of fluctuation for different bandwidths as labelled by the dash lines on the plot. When the bandwidth becomes narrower, the S_{21} Parameter decreases more rapidly on both sides out of the centre frequency.

Above all, by increasing the bandwidth, the level of ripples cannot be decreased, so that any bandwidth can be chosen according to the requirement of the design.

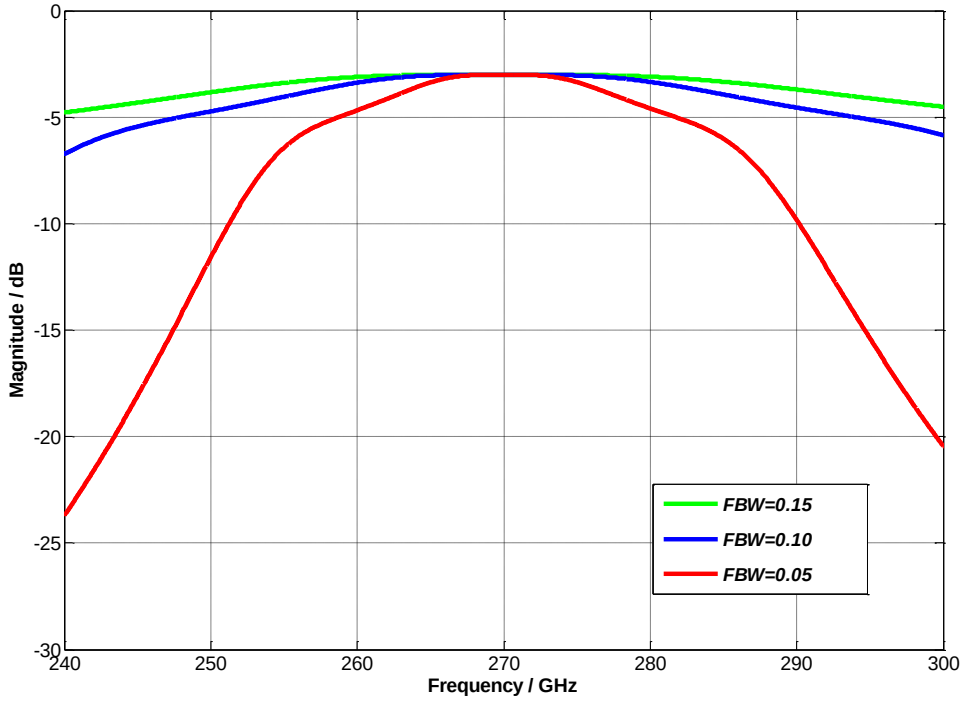

Figure 3.8 the S_{31} Parameter with Different Bandwidths from Theory

From the Figure 3.8 above, we can get that S_{31} Parameter will have the magnitude of -3 dB at the centre frequency regardless of the bandwidth. With the bandwidths decreasing, the S_{31} parameter decreases more rapidly on both sides out of the centre frequency. The plot of S_{31} Parameter is not a symmetrical curve, the magnitude at 240 GHz (30 GHz below the centre frequency) is about -23.5 dB while the magnitude at 300 GHz (30 GHz higher than the centre frequency) is around -20 dB. That is due to the inductive coupling between resonators of this design. The inductive coupling has the property that the left side of the frequency response is a little bit higher than the right side as illustrated in the figure above, which is opposite to the capacitive coupling.

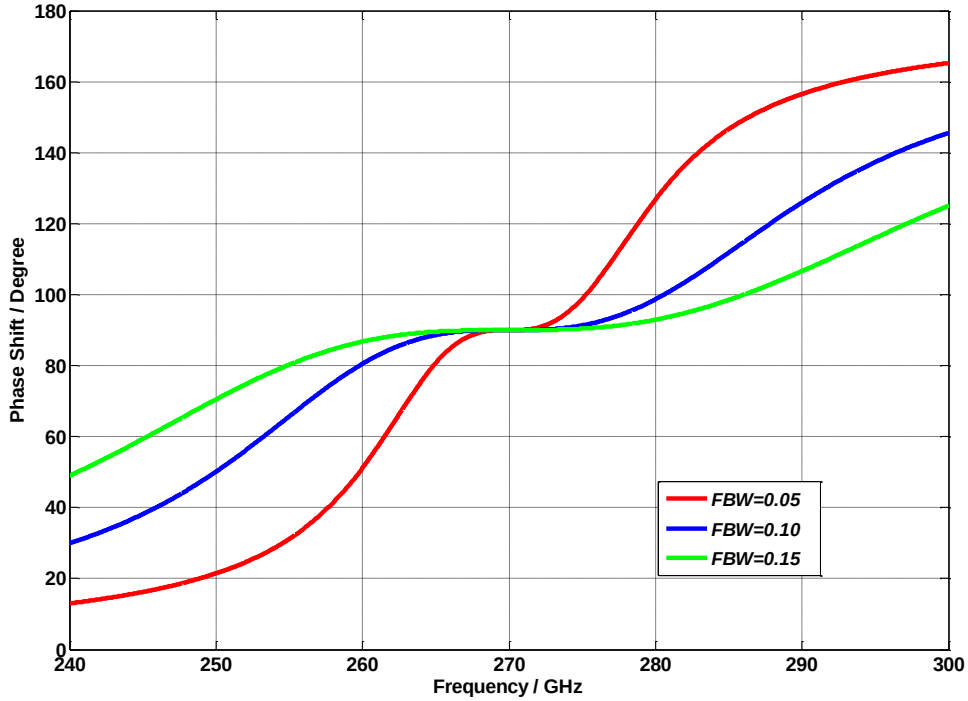

Figure 3.9 Phase Shift between Port 2 and Port 3 with Different Bandwidths from Theory

Figure 3.9 is the comparison of phase shift between port 2 and port 3 with different bandwidths, the phase shift remains at 90 degree at the centre frequency regardless of the bandwidth, but it changes more rapidly when the bandwidth decreasing.

Above all, the bandwidth will not change the number of ripples or the amplitude fluctuation of the ripples in the S_{21} parameter. The S_{21} and S_{31} parameters will keep at -3 dB and the phase shift will remain at 90 degree at the centre frequency, which implies that, the ripples cannot be weakened or removed by increasing the bandwidth. In this design, the fractional bandwidth is chosen to be 5% to fit for the coupling coefficients that could be achieved by the waveguide cavity resonators.

Chapter 4

Waveguide Resonator Implementation of the 90 Degree Hybrid Coupler

4.1 Properties of the Waveguide Cavity Resonators

The hollow waveguide is used in high-power systems, and millimetre wave systems, due to the loss is less compared with transmission lines. Figure 4.1 is the geometry of a hollow rectangular waveguide, μ and ε are the permeability and permittivity of the material filled in the hollow tube. In this project, it is a vacuum inside the rectangular waveguide, these two parameters are therefore: μ=1.2556x10^{-6} H/m and ε=8.85x10^{-12} F/m. In Figure 4.1, a and b are the dimensions of the waveguide cavity, it is a standard convention to put the longer side along the x-axis, so that we have $a > b$.

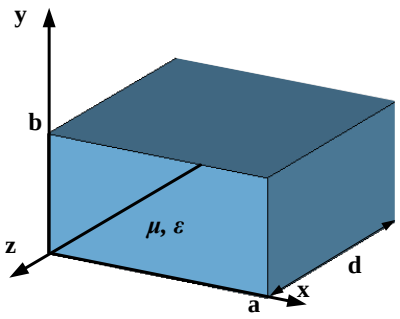

Figure 4.1 Geometry of a Rectangular Waveguide

This kind of waveguide can propagate TE mode or TM mode waves. TE mode is defined as fields with E_z=0, similarly, TM mode has the property as H_z=0. Each kind of the mode has a cut-off frequency below which the propagation is not possible. The cut-off frequency $f_{c_{mn}}$ of a TE$_{mn}$ mode or TM$_{mn}$ mode can be calculated by [12]:

$$f_{c_{mn}} = \frac{k_c}{2\pi\sqrt{\mu\varepsilon}} = \frac{1}{2\pi\sqrt{\mu\varepsilon}}\sqrt{\left(\frac{m\pi}{a}\right)^2 + \left(\frac{n\pi}{b}\right)^2} \tag{4.1}$$

The mode that has the lowest cut-off frequency is the dominant mode. TE$_{10}$ mode is the dominant mode for this design, which has the cut-off frequency of 174 GHz after calculation by

Equation (4.1). It is also the only mode available in the desired frequency range, since the TE_{20} mode has the second lowest cut-off frequency at 348 GHz, hence the definition of the single mode WR-3 frequency band (220 GHz - 325 GHz).

The transverse electric field (E_x, E_y) of the TE_{10} mode rectangular waveguide can be written as [12]:

$$\overrightarrow{E_t}(x,y,z) = \vec{e}(x,y)\left[A^+ e^{-j\beta_{10}z} + A^- e^{j\beta_{10}z}\right] \tag{4.2}$$

In which, $\vec{e}(x,y)$ is the transverse variation of the mode, and A^+, A^- are the amplitudes of the travelling waves propagated forward and backward inside the waveguide. β_{10} is the propagation constant for the TE_{10} mode, the general definition of the propagation constant β_{mn} is [12]:

$$\beta_{mn} = \sqrt{k^2 - \left(\frac{m\pi}{a}\right)^2 - \left(\frac{n\pi}{b}\right)^2} \tag{4.3}$$

Where $k = \omega\sqrt{\mu\varepsilon}$.

β_{mn} is also related to guided wavelength, λ_g:

$$\beta_{mn} = 2\pi / \lambda_g \tag{4.4}$$

By applying the boundary condition as $\overrightarrow{E_t}(x,y,z) = 0$ at $z = 0$ to Equation (4.2), we can get that $A^+ = -A^-$, which also implies the perfect reflection of the waveguide wall.

In order to get a waveguide cavity resonator from a waveguide, one thing needs to be considered about is the new constraints placed on the electromagnetic fields if end walls are placed on a waveguide. New boundary conditions must be applied, which means the transverse electric field must be zero at the end wall. At resonant frequency, assuming the waveguide cavity resonator has a length of d in the z-axis, also applying the boundary condition as $\overrightarrow{E_t}(x,y,d) = 0$ to Equation (4.2), which will lead to the equation:

$$\overrightarrow{E_t}(x,y,d) = -\vec{e}(x,y)A^+ \cdot 2j \cdot \sin(\beta_{10}d) \tag{4.5}$$

As $A^+ \neq 0$, the nontrivial solution occurs when:

$$\beta_{10} d = \frac{2\pi}{\lambda_g} d = n\pi, \quad n = 1, 2, 3\ldots \tag{4.6}$$

Which means the cavity length *d* should be a multiple of half guided wavelength at resonance.

One of the important property of the waveguide cavity resonator is the attenuation in a waveguide is small, hence producing a high Q resonator. The attenuation can be caused by either dielectric loss or conductor loss. α_d is the attenuation due to dielectric loss, while α_c is the attenuation due to conductor loss, the total loss is: $\alpha = \alpha_d + \alpha_c$. For the hollow waveguide, the dielectric loss can be neglected since the waveguide is filled with vacuum, so that only the conductor loss needs to be taken into consideration. It can be calculated by the following equation [12]:

$$\alpha_c = \frac{R_s}{a^3 b \beta k \eta} (2b\pi^2 + a^3 k^2) \quad Np/m \tag{4.7}$$

Translating the unit into decibels, the above equation has the following form:

$$\alpha_c = \frac{R_s}{a^3 b \beta k \eta} (2b\pi^2 + a^3 k^2) \times 8.686 \quad dB/m \tag{4.8}$$

In which, R_s is the surface resistivity of the conductor:

$$R_s = \sqrt{\frac{\omega \mu_0}{2\sigma}} \tag{4.9}$$

μ_0 is the permeability of the conductor, and σ is the conductivity of the conducting wall, ω is the angular frequency ($\omega = 2\pi f$). η is the intrinsic impedance of the material filling in the waveguide, given by $\eta = \sqrt{\frac{\mu}{\varepsilon}}$.

Another important characteristic for the waveguide cavity resonator is the unloaded quality factor Q_u. The unloaded quality factor Q_u of a resonant circuit is defined as the ratio of the stored energy over the energy dissipated in one cycle. The energy dissipation can be caused by either dielectric loss or electric wall loss, which can be performed by the following equation:

$$Q_u = \left(\frac{1}{Q_c} + \frac{1}{Q_d} \right)^{-1} \tag{4.10}$$

Q_c represents the loss of conducting walls, while Q_d represents the dielectric loss. For the waveguide cavity filled with air in this project, the unloaded quality factor of the cavity in TE_{10} mode is related to lossy conducting walls but lossless dielectric, so that it can be represented by Q_c [12]:

$$Q_u = Q_c = \frac{(kad)^3 b\eta}{2\pi^2 R_s} \frac{1}{(2l^2a^3b + 2bd^3 + l^2a^3d + ad^3)} \tag{4.11}$$

The parameters in that equation have already been defined previously.

4.2 Extraction of Waveguide Resonator Dimensions

The specifications of the 90 degree hybrid coupler in this project are:

- Centre frequency f_0: 270 GHz
- Fractional bandwidth (*FBW*): 5%

According to those specifications of the 90 degree hybrid coupler and using the method in Chapter 3, we can calculate the value of coupling coefficients: k_{E1} = 0.0707, k_{E2} = 0.05 and the external quality factors: Q_{e1}=Q_{e2}=Q_{e3}=Q_{e4}=20. The extraction of dimensions of the 90 degree hybrid coupler will be based on those parameters calculated by the specifications.

4.2.1 Calculation of the Waveguide Cavity Length

From section 4.1, the waveguide cavity resonator length *d* should be a multiple of half guided wavelength at resonance. The guided wavelength λ_g can be calculated by the equation below:

$$\lambda_g = \frac{2\pi}{\beta} = \frac{2\pi}{\sqrt{k^2 - \left(\frac{m\pi}{a}\right)^2 - \left(\frac{n\pi}{b}\right)^2}} = \frac{2\pi}{\sqrt{(\omega\sqrt{\mu\varepsilon})^2 - \left(\frac{m\pi}{a}\right)^2 - \left(\frac{n\pi}{b}\right)^2}} \tag{4.12}$$

In which, $\omega = 2\pi f$, μ=1.2556x10^{-6} H/m, ε=8.85x10^{-12} F/m, for the WR-3 band waveguide, a=0.864 mm, b=0.432 mm. After calculation, the guided wavelength (λ_g) is 1.449 mm. Thus, the waveguide cavity resonator has the initial length of 0.724 mm. This can be modified by coupling to the resonator and fine tuning will be discussed later.

4.2.2 Calculation of the External Quality Factor

The external quality factor is an indication of the 'damping' of the resonance due to the coupling between the resonator and external circuits [34]. Higher quality factor indicates lower rate of energy loss relative to the stored energy in the resonator. The quality factor also characterizes a resonator's bandwidth relative to its centre frequency according to Equation (3.14). The larger Q_e, the smaller *FBW*, which also means more damping due to the coupling to external circuit. The loaded quality factor Q_L, the external quality factor Q_e and the unloaded quality factor Q_u have the relationship as:

$$\frac{1}{Q_L} = \frac{1}{Q_e} + \frac{1}{Q_u} \tag{4.13}$$

The physical structure in a CST simulation can be used to determine the external quality factor Q_e, such a structure is shown in Figure 4.2, the waveguide cavity resonator is coupled to the input and output ports by apertures, this is a symmetrical structure, so that the couplings between the input port and the output port are the same, the apertures have the thickness denoted as *t* and width denoted as *W*.

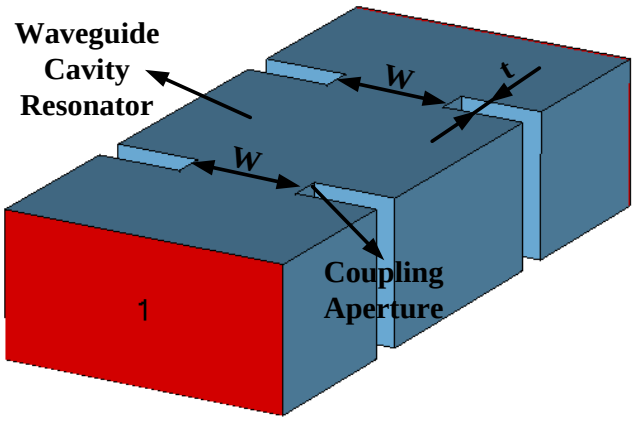

Figure 4.2 the Physical Structure in CST for External Quality Factor Determination

Figure 4.3 shows the S_{21} parameter for the structure in Figure 4.2. The external quality factor can be calculated using the centre frequency (f_0) divided by the 3 dB bandwidth (Δf_{3dB}) as shown in Figure 4.3.

$$Q_e = \frac{f_0}{\Delta f_{3dB}} \tag{4.14}$$

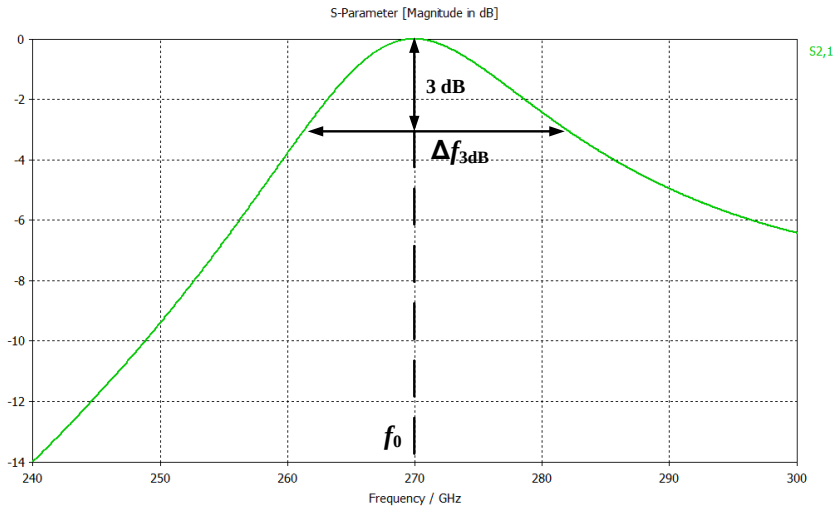

Figure 4.3 Frequency Response of S_{21} for the Structure in Figure 4.2 from Simulation

Due to the symmetrical structure, the external quality factors for input and output ports are the same, the quality factor derived from Figure 4.3 are therefore double the loaded external quality factor Q_e'[17]:

$$Q_e' = \frac{Q_e}{2} = \frac{f_0}{\Delta f_{3dB}} \tag{4.15}$$

By simply changing the size of the aperture, the value of external quality factor alters. Figure 4.4 is a plot of the external quality factor Q_e with changes of the aperture width *W*, while the thickness *t* keeps constant at 1 mm. It can be realized that the external quality factor decreases when the aperture width increases, that also implies with aperture size increasing, the coupling between resonator and external circuit becomes stronger.

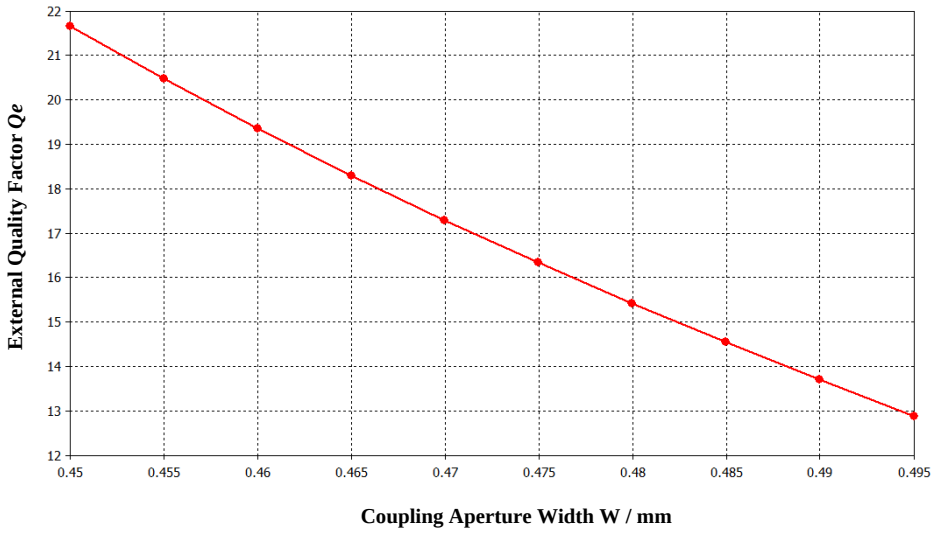

Figure 4.4 External Quality Factors Varying with Aperture Width W from Simulation

The aperture size will also affect the centre frequency a little, this is shown in Figure 4.5. Due to this reason, further optimisations will be needed when assembling all parts together to build the 90 degree hybrid after determining the size of each part separately.

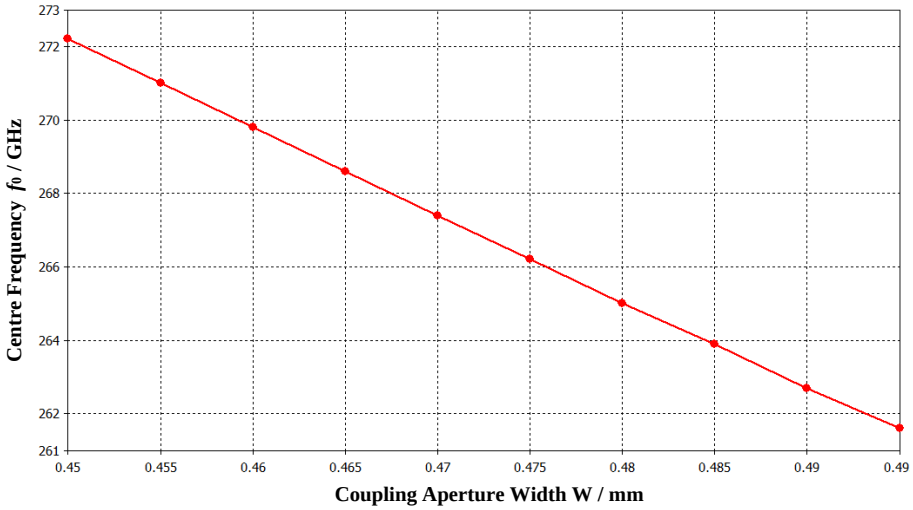

Figure 4.5 Centre Frequency Shift with the Aperture Width (*W*) from Simulation

4.2.3 Calculation of the Coupling Coefficients

Coupling coefficients, resonant frequencies and external quality factors are the based parameters in the resonator filter theory. The coupling coefficient of resonators is a dimensionless value that characterizes interaction between two resonators. In order to adjust the frequency response of the filter it is sufficient to optimise the coupling coefficients.

In general, the resonators may have different physical structures, thus have different resonant frequencies (illustrated in Figure 4.6). The coupling coefficient between these resonators can be defined on the basis of the ratio of coupled energy to stored energy. The coupling coefficient *k* can be mathematically calculated by Equation (4.16), while the first term on the right-hand side represents the electric coupling, and the second term represents the magnetic coupling [17].

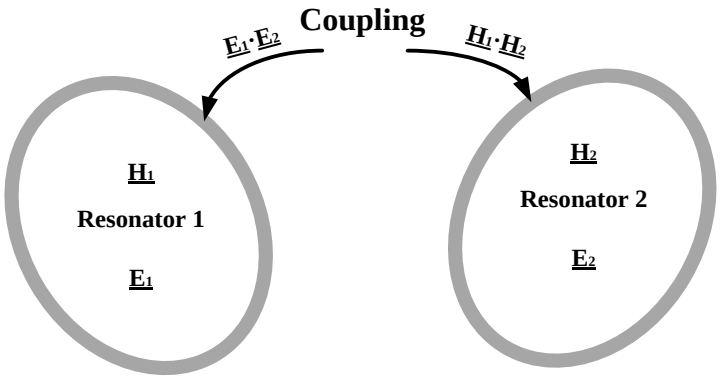

Figure 4.6 General Coupled Resonators with Different Structures [17]

$$k = \frac{\iiint \varepsilon \overline{E_1} \cdot \overline{E_2} dv}{\sqrt{\iiint \varepsilon \left|\overline{E_1}\right|^2 dv \times \iiint \varepsilon \left|\overline{E_2}\right|^2 dv}} + \frac{\iiint \mu \overline{H_1} \cdot \overline{H_2} dv}{\sqrt{\iiint \mu \left|\overline{H_1}\right|^2 dv \times \iiint \mu \left|\overline{H_2}\right|^2 dv}} \tag{4.16}$$

However, it would be much easier if we can find the relationship between the coupling coefficient and some characteristic frequencies. In this way, it can be much easier to determine the coupling coefficient instead of using physical structures, as the volume integrals in Equation (4.16) would be very difficult for calculation. An EM simulation will be necessary to establish the relationship between coupling coefficient and characteristic frequencies. CST Microwave Studio is used in this project and Figure 4.7 shows the model used in CST. However, there are two different coupling coefficients that need to be determined: one is the coupling coefficient between resonator 1 and resonator 2, denoted as kc_1, and the other is the coupling coefficient between resonator 2 and resonator 3, denoted as kc_2, Figure 4.7 is the model to determine kc_1, the ports are weakly coupled to an extent that energy can pass through, but all the couplings for the whole circuit are concentrated on the inter couplings between resonators. Figure 4.8 is the S_{21} frequency response after the simulation of the model in Figure 4.7.

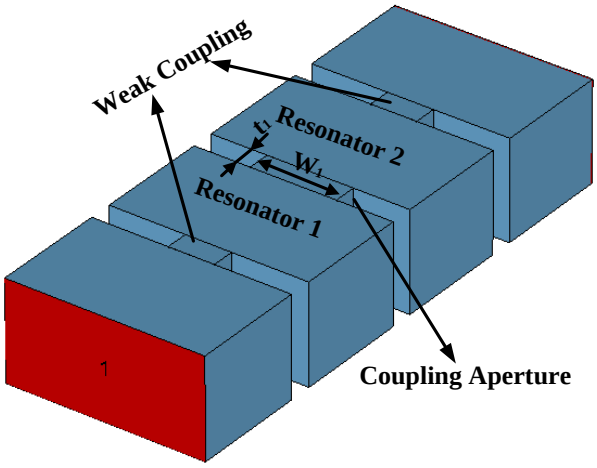

Figure 4.7 the Physical Structure in CST for Coupling Coefficient kc_1 Determination

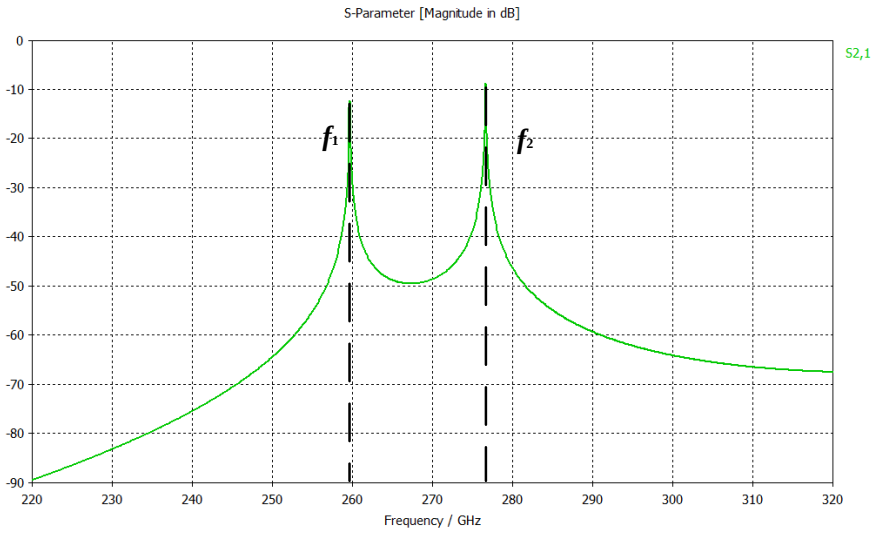

Figure 4.8 Frequency Response of S_{21} from Simulation for the Structure in Figure 4.7

The frequency response in Figure 4.8 has two peaks at frequencies f_1 and f_2. The coupling coefficient can be derived from those two characteristic frequencies:

$$kc = \frac{f_2^{\,2} - f_1^{\,2}}{f_2^{\,2} + f_1^{\,2}} \tag{4.17}$$

The above formula is applicable for both kc_1 and kc_2.

Figure 4.9 is the plot of coupling coefficient kc_1 changes with the coupling aperture width W_1; the aperture thickness is constant at 1 mm. The coupling is stronger with the aperture size increasing.

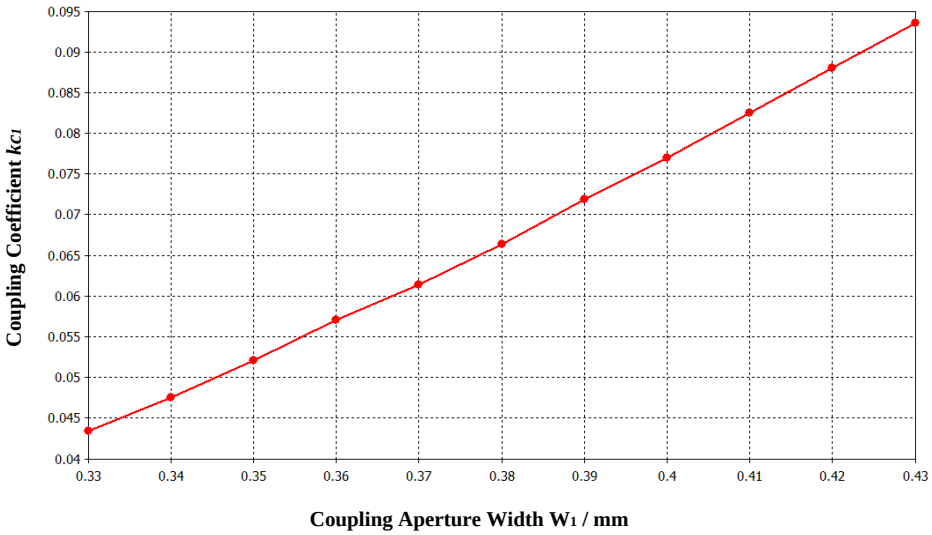

Figure 4.9 Coupling Coefficient kc_1 Varying with Aperture Width W_1 from Simulation

Figure 4.10 is the physical structure in CST to extract the coupling coefficient kc_2 between resonator 2 and resonator 3. This is realized by a four-port network. We only want signals propagate in a path through port 2, resonator 2, the coupling aperture, resonator 3 and port 4. Designing a very tiny gap between port 1 and resonator 2, port 3 and resonator 3 to make sure there is hardly any signal pass through port 1 or port 3. The coupling coefficient kc_2 can be extracted by the S_{42} parameter after simulating the model in CST. The plot of coupling coefficient varying with the aperture width W_2 is shown in Figure 4.11. The coupling is stronger with the aperture size increasing.

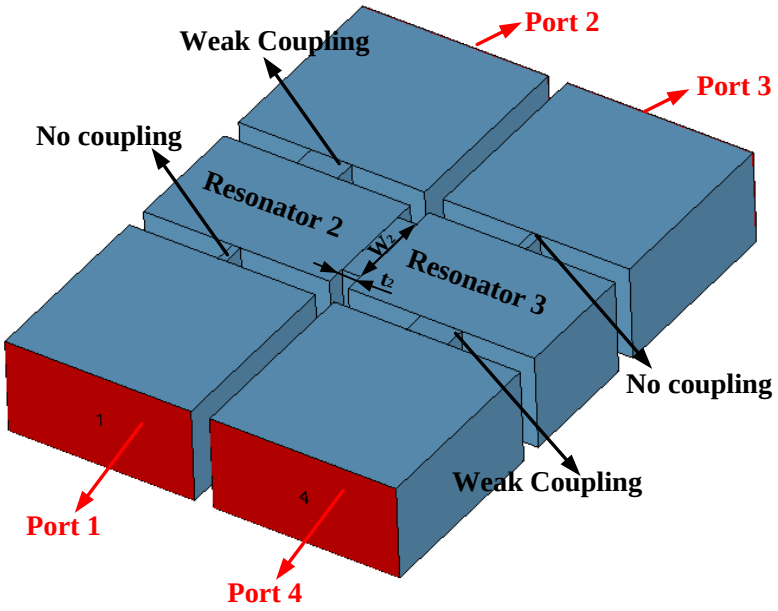

Figure 4.10 the Physical Structure in CST for Coupling Coefficient kc_2 Determination

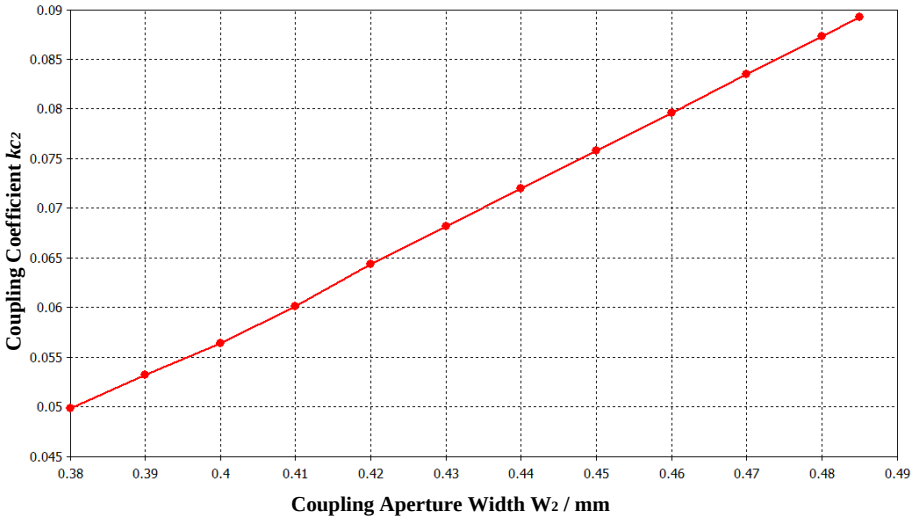

Figure 4.11 Coupling Coefficient kc_2 Varying with Aperture Width W_2 from Simulation

4.3 Waveguide Resonator Implementation

After determining the required coupling coefficients, external quality factors by the methods mentioned above, this 90 degree hybrid coupler is implemented by putting all parts together, it is constructed by waveguide cavity resonators, each with a length of half guided wavelength.

The design has been tailored to suit a simple fabrication for the SU-8 photo-resist technology. It is composed by only three layers, and clamped by two brass plates for assembly. However, the hybrid coupled itself is built on the second layer with a thickness of 0.432 mm. The layout of the 90 degree hybrid implemented with waveguide cavity resonators is shown in Figure 4.12.

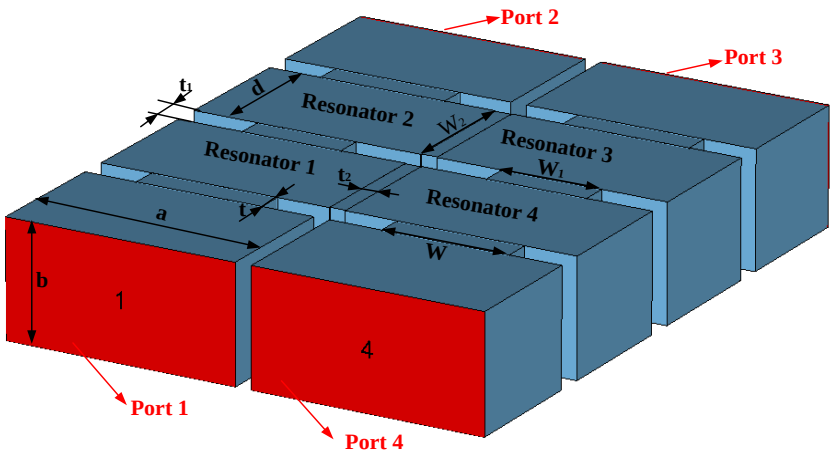

Figure 4.12 90 Degree Hybrid Coupler Implementation

4.4 Final Optimisation

After obtaining the initial values of the dimensions by the method in Chapter 4.2, the whole structure in Figure 4.12 has to be put into CST for further optimisation. Since the size of each aperture is obtained separately, they will have interactions with each other after assembly, thus the optimisation will deal with the problems caused by the undesired interactions. The main dimensions after final optimisation are listed in Table 4.1.

Waveguide Dimensions	a x b	0.864 mm x 0.432 mm
Waveguide Cavity Resonator Length	d	0.495 mm
Aperture Between Port and Resonator	W x t	0.475 mm x 0.100 mm
Aperture Between Resonator 1 and 2	W_1 x t_1	0.375 mm x 0.100 mm
Aperture Between Resonator 2 and 3	W_2 x t_2	0.485 mm x 0.060 mm

Table 4.1 Summary of Main Design Dimensions

The frequency responses after the optimisation are shown in Figure 4.12, as Figure 4.12 (a) is the *S* parameters, while Figure 4.12 (b) is the phase shift between port 2 and port 3.

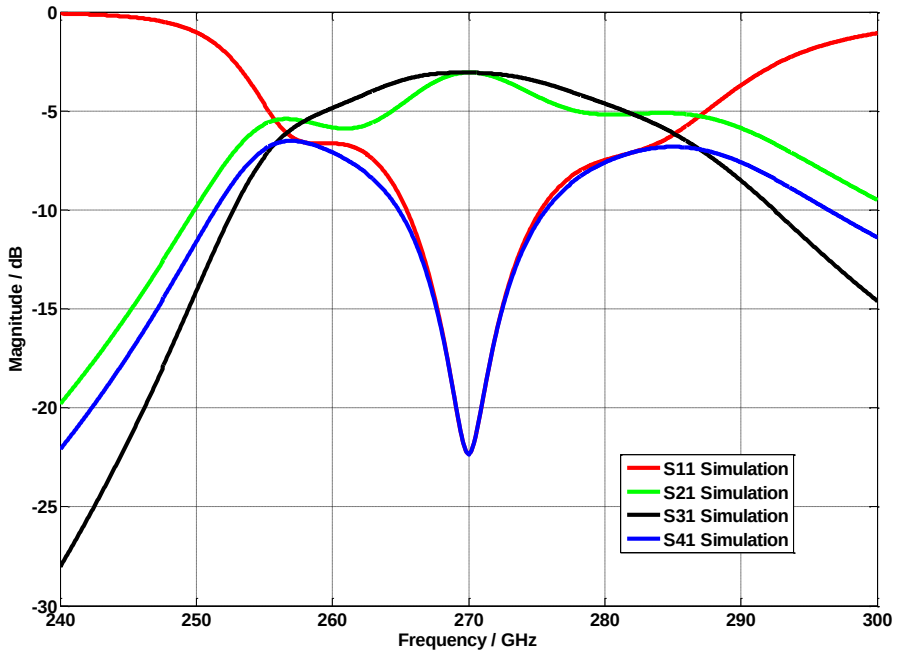

(a)

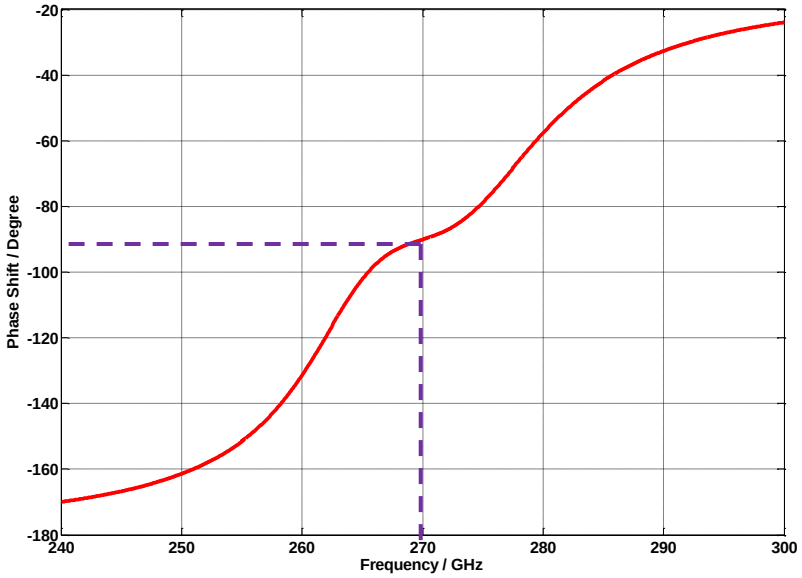

(b)

Figure 4.12 (a) Frequency Response of Magnitude for the 90 Degree Hybrid Coupler after Optimisation (b) Frequency Response of Phase Shift between S_{21} and S_{31} for the 90 Degree Hybrid Coupler after Optimisation from Simulation

The optimised frequency response by CST Microwave Studio (as shown in Figure 4.13 (a) by dashed lines) is compared with the response calculated by the coupling matrix in Chapter 3. It can be noted that the isolation between two output ports is -22.35dB, and the return loss (RL) is also larger than -30 dB. We can further optimise the design to get better RL and isolation, but this will degrade the responses of S_{21} and S_{31} to an extent that they cannot both get to exactly –3 dB at the centre frequency. Figure 4.13 (b) is a comparison of phase difference between port 2 and port 3. From those two figures, the simulation results agree well with the theoretical calculation. The signal fed into port 1 is divided equally at port 2 and port 3 with a phase different of 90 degree.

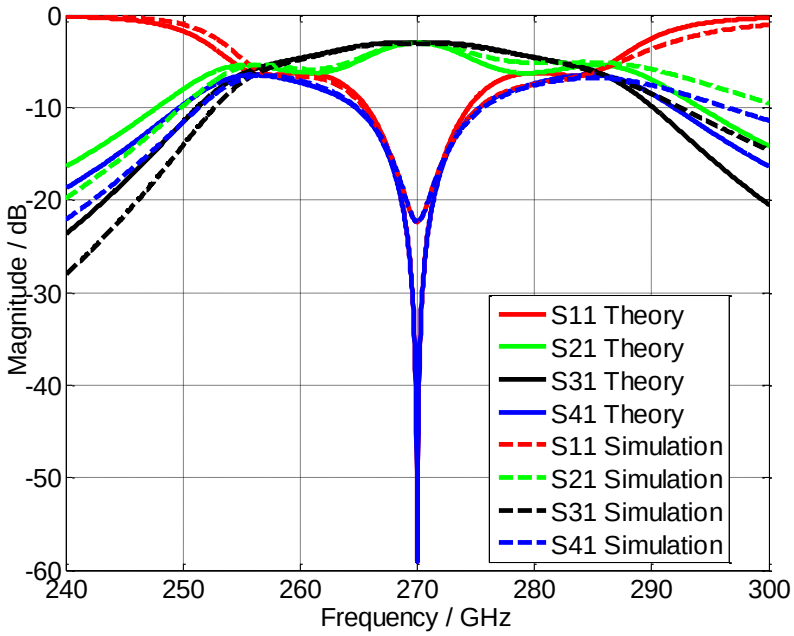

(a)

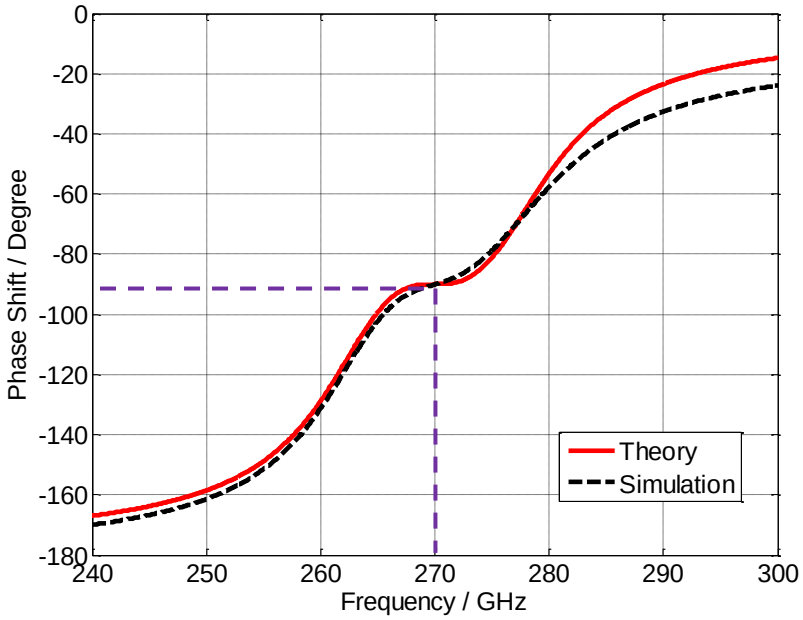

(b)

Figure 4.13 (a) Comparison of Frequency Response for the 90 Degree Hybrid Coupler with Coupled Waveguide Cavity Resonators (b) Comparison of Phase Shift between S_{21} and S_{31} for the 90 Degree Hybrid Coupler Coupled Waveguide Cavity Resonators

Chapter 5

Fabrication and Measurement of the Butler Matrix with Bends

5.0 Introduction of Micromachining

Terahertz electromagnetic radiation is from 100 GHz to 10 THz, which lies in a region between the microwave and infrared region of the spectrum. As the frequencies of the operating circuits go higher, conventional machining techniques are limited by the minimum size of the milling tool. In the past few years, several micromachined techniques have been investigated for the machining of THz-components, which include: electrical discharge machining (EDM), bulk silicon micromachining using dry and wet etching techniques, LIGA processes based on X-ray or UV exposure and thick photoresist (SU-8) techniques [2]. The SU-8 photoresist technology has the advantages of high aspect ratio (>15:1), easily processed, relatively low cost with high performance [3], so that it is used in this project.

The procedure of a general SU-8 photoresist processing is briefly introduced here. SU-8 is very difficult to remove when it is got onto something, so that it is important to use SU-8 ovens and SU-8 tweezers and SU-8 hotplates in the procedure, otherwise, the SU-8 will contaminate the processes that do not use SU-8. After the cleaning procedure, the SU-8 is firstly applied onto a 4-inch diameter silicon wafer with the desired thickness. Afterwards, soft-bake is taken at 65 °C for 20 min and then at 95 °C for 4.5 hours for the desired 432 μm thick layers before the SU-8 resist is exposed under UV light. To produce the cross-linking reactions, a post exposure bake is then required at 65 °C for 2 min and then 95 °C for 30 min. Finally, development is employed under the EC solvent to remove unwanted SU-8 and hard bake is undertaken to make sure it is robust enough. Realising it from the silicon wafer, the SU-8 is then coated with a 2 μm thick gold and chrome is used to bond all layers together [35]. It is worth mentioning that the SU-8 has a low thermal stability and a large thermal expansion coefficient [2], the whole procedure is undertaken in an acceptable low temperature and evaporation of the gold is done by multistage process.

5.1 Micromachined Butler Matrix with Bends

5.1.1 Purpose of Bend Design

For this design, the waveguide hybrid coupler itself is constructed by three SU-8 layers. However, the waveguide flange is too large compared with the hybrid coupler in size. Here we consider low loss curved bends to be connected to each port of the hybrid, so that it could be connected to the load and the flanges for measurement. In addition to this, the feeding waveguide flange cannot be connected to the side wall of multiple layers, so that a 90 degree bend is needed to turn the waveguide along its H-plane to enable connection.

5.1.2 Micromachined Bend Design

Due to the small size of the 90 degree hybrid coupler compared with the waveguide flange, four lossless curved bends are connected to each port of the hybrid as illustrated in Figure 5.1. The frequency response of a single curve is plotted in Figure 5.2, which has a return loss less than -80 dB between the operating frequency. Thus, these curved bends will have little influence on the frequency response of the 90 degree hybrid when connecting them together.

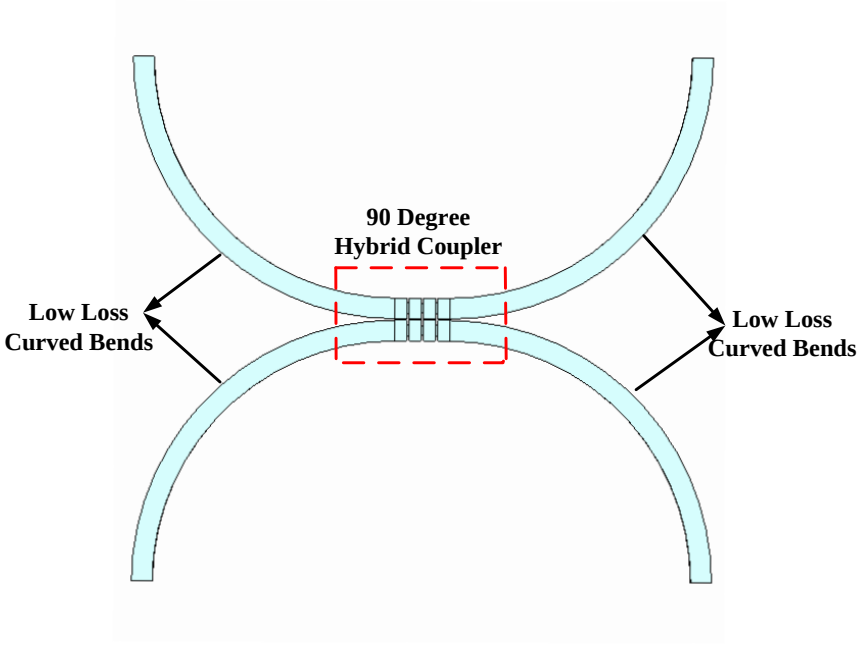

Figure 5.1 Configuration of the Hybrid Coupler Connected With Curved Bends

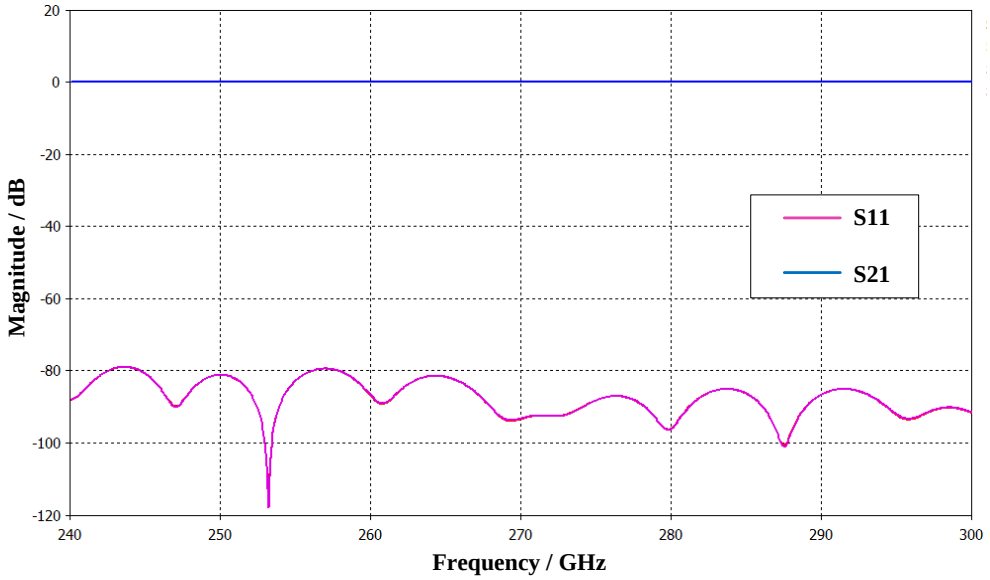

Figure 5.2 Frequency Response of a Single Curved Bend in Figure 5.1 from Simulation

In addition to this, the waveguide flange cannot be connected to the side wall of the layers, moreover, waveguide right-angle corners exhibit narrowband and mismatched response, so that a 90° bend is designed to turn the waveguide along its E-plane to the surface of the layers for connection. Conventionally, smooth transaction such as multi-stepped or multi-mitred corners can be connected between the two orthogonal waveguide arms to achieve a broadband matching [36]. However, neither of these is compatible with the SU-8 multi-layered structures presented here. Modified bends have been developed to meet the requirement for SU-8 micromachining technology. Curved and round edges have been applied at the junction region [37-38]. A novel waveguide 90° bend built on two layers of SU-8 for this design is presented in Figure 5.3. The blue part is vacuum, which is surrounded by perfect electric conductor (PEC) in the simulation, while the grey part in the figure is the PEC inserted into the vacuum. The dimensions of the bend are illustrated in this figure (dimensions are in millimetres). The appropriate dimensions are obtained after an optimisation process by CST Microwave Studio.

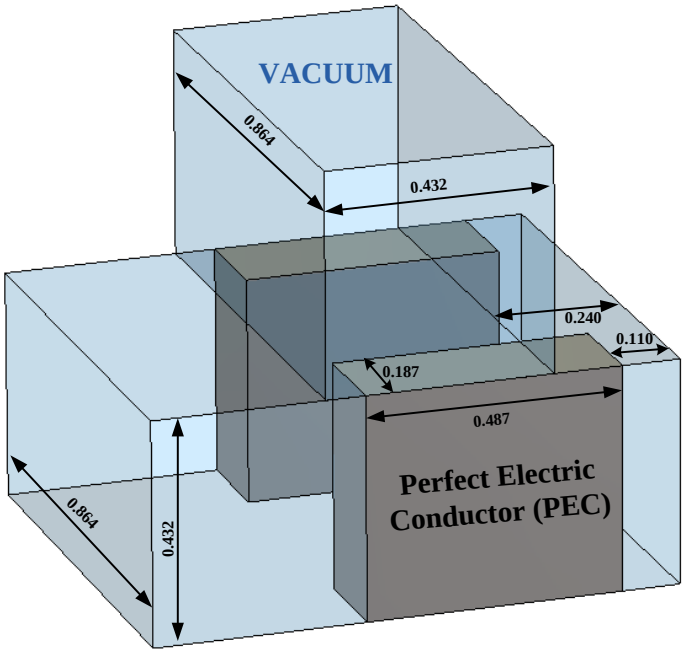

Figure 5.3 Structure of the 90° Bend

The simulation result of the model in Figure 5.3 is plotted in Figure 5.4. It shows a good matching between 250 GHz and 300 GHz and has a return loss better than -20 dB over the operating frequency range of the Butler Matrix.

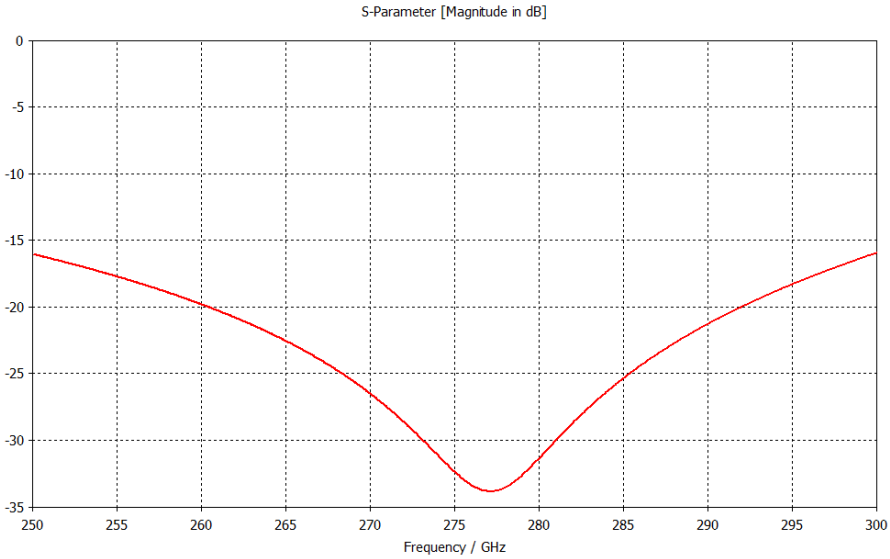

Figure 5.4 Frequency Response of the Optimised 90° Bend from Simulation

5.1.3 Realization of the Butler Matrix with Bends

The SU-8 photolithography process has been utilized to make the device. More descriptions of this technology could be found in Chapter 5.0 in detail. The configuration of the model simulated in CST is shown in Figure 5.5 (a), it has two pairs of back-to-back bends, and the blue part is vacuum, surrounded by PEC. The waveguide with the bends has been made of three layers of SU-8 with the same thickness of 0.432 mm, as shown in Figure 5.5 (b). Figure 5.5 (c) and (d) depict the top view of the first and second layers, in which the holes around the waveguide are fitted to screws and the alignment pins for a standard WR-3 waveguide flange. The size of each SU-8 layer is 48 mm x 48 mm. Finally, the device will be assembled and the layers are going to be aligned using pins.

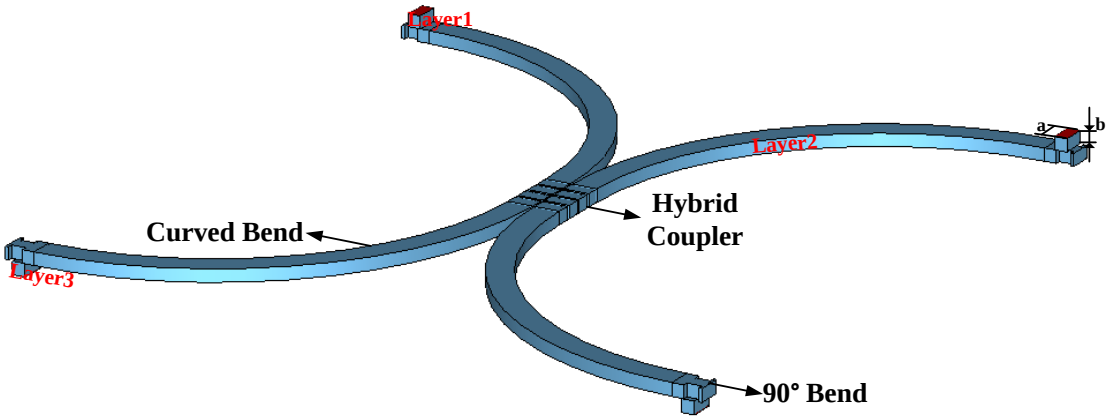

(a)

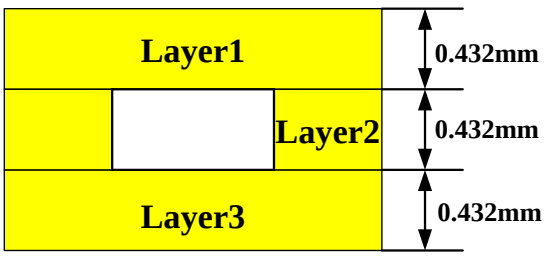

(b)

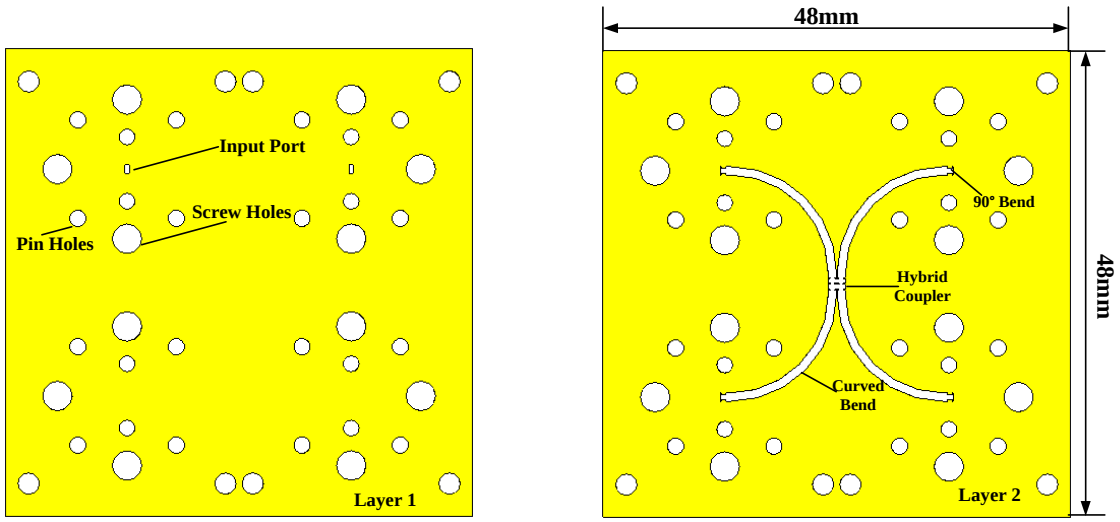

(c) (d)

Figure 5.5 Configuration of the Designed Waveguide with Bends

(a) Simulation Model in CST. (b) Cross-section View of the Micromachined Waveguide Structure. (c) Top View of the First Layer. (d) Top View of the Second Layer.

The three layers of SU-8 are clamped together using conventionally machined metal plates made from brass, shown in Figure 5.6 (a). The brass plates are designed to position the WR-3 waveguide flanges. The side view of the whole structure clamped by brass plates are shown in Figure 5.6 (b).

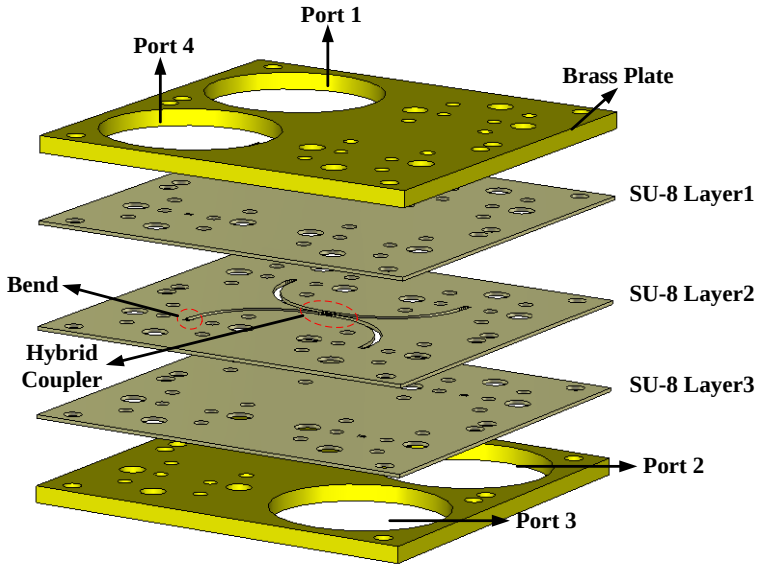

(a)

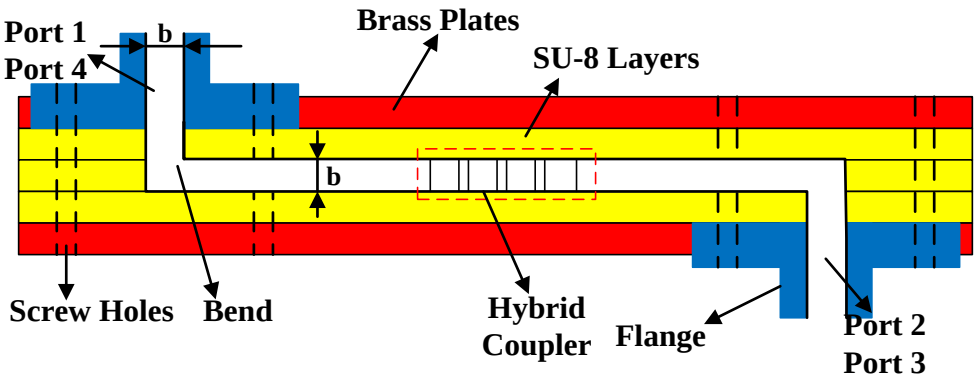

(b)

Figure 5.6 Side View of the Whole Structure Clamped with Brass Plates

The simulation result of the waveguide hybrid with bends built on multi-layer structure is shown in Figure 5.7, compared with the theoretical predictions from the coupling matrix in Chapter 3. Figure 5.7 (a) is the comparison of *S* parameters, (b) is a more detailed comparison of S_{21} and S_{31} parameters, (c) is the phase difference between the two output ports. From these plots, we can get that the centre frequency is shifted by about 0.5 GHz due to the impact of the bends. Some ripples occur on both sides out of the centre frequency and the fluctuations of these

ripples on left side are more obvious than those on the right side. This is due to the 90° bends have an asymmetrical frequency response over the operating bandwidth of the hybrid, the return loss is better in lower frequencies within the bandwidth. Form Figure 5.7 (b), S_{21} is about 0.1 dB higher than -3 dB and *S*31 is about 0.1 dB lower than -3 dB. In this way, 51% of the power incident into port 1 is transmitted through port 2, while the remaining 49% is transmitted through port 3, this can be calculated by Equation (2.10). The phase shift between the two output ports is 90 degree at the centre frequency.

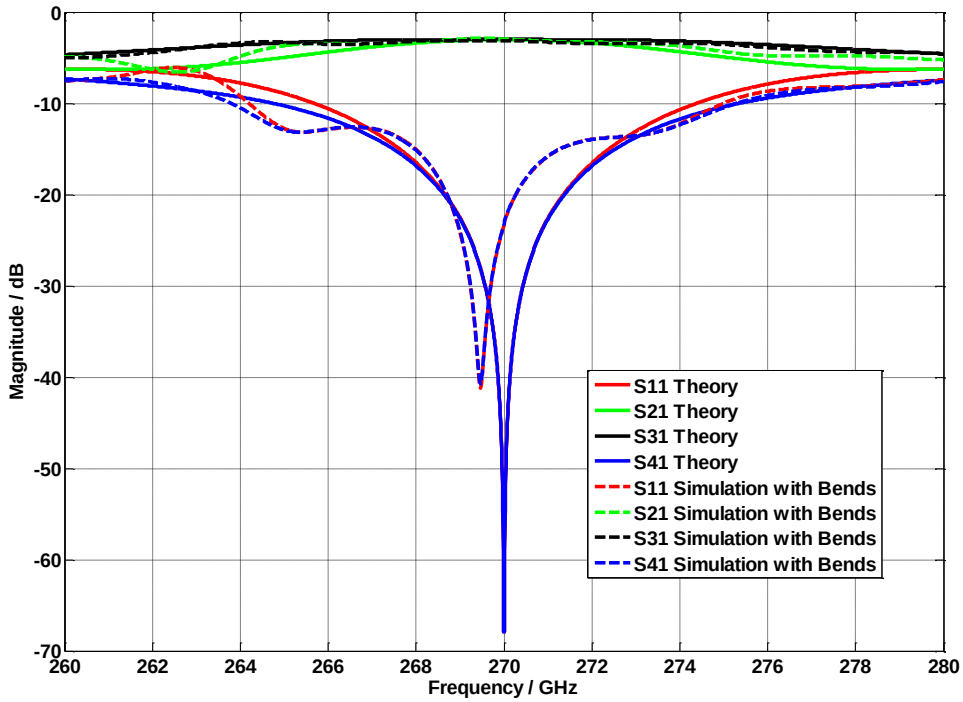

(a)

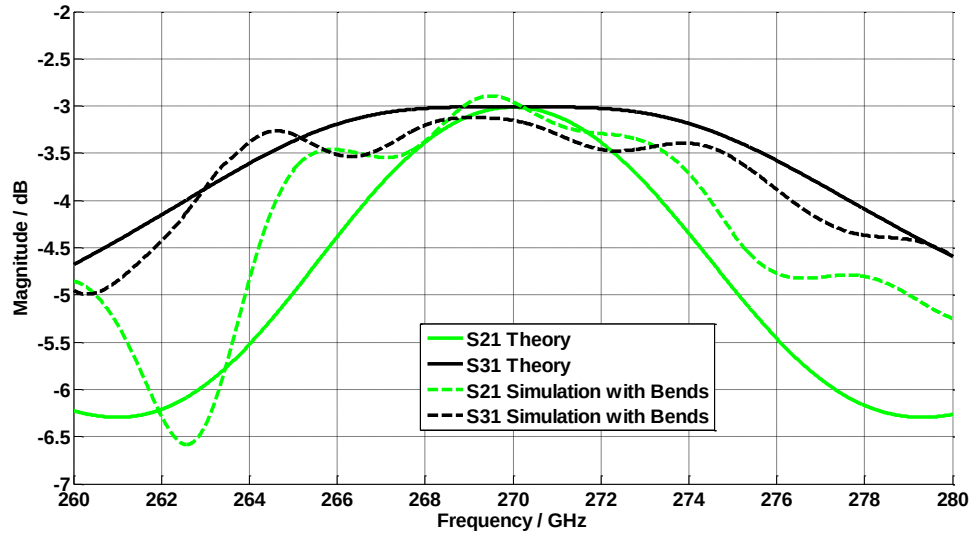

(b)

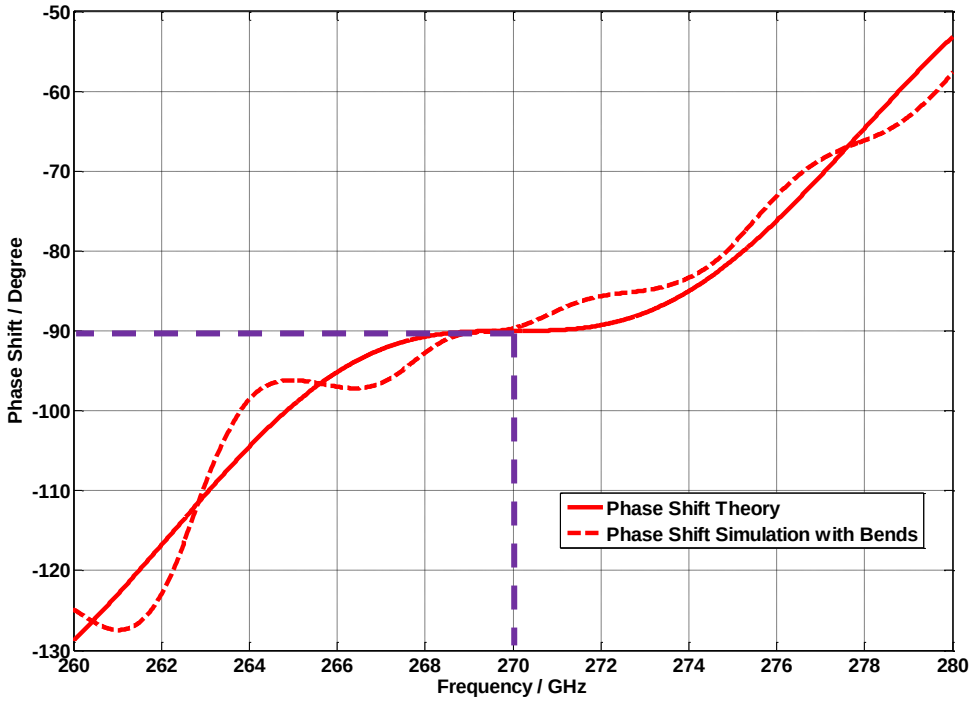

(c)

Figure 5.7 Simulated Frequency Response of Waveguide Hybrid Coupler with Bends Compared with Theoretical Calculations.

(a) Comparison of *S* Parameters. (b) More Detailed Comparisons of S_{21} and S_{31} around the centre frequency. (c) Phase Shift between S_{21} and S_{31} Compared with Theoretical Calculations.

5.2 Fabrication and Measurement

The WR-3 band waveguide Butler Matrix with bends is fabricated using the SU-8 micromachining technique explained in 5.0. The three SU-8 layers are aligned using the alignment pins after the metal coating process. The SU-8 layers are then clamped together using conventionally machined metal plates made from brass, during which screws are employed to tighten the brass plates and the SU-8 pieces and make a good contact between them. A photograph of the assembled device is shown in Figure 5.8.

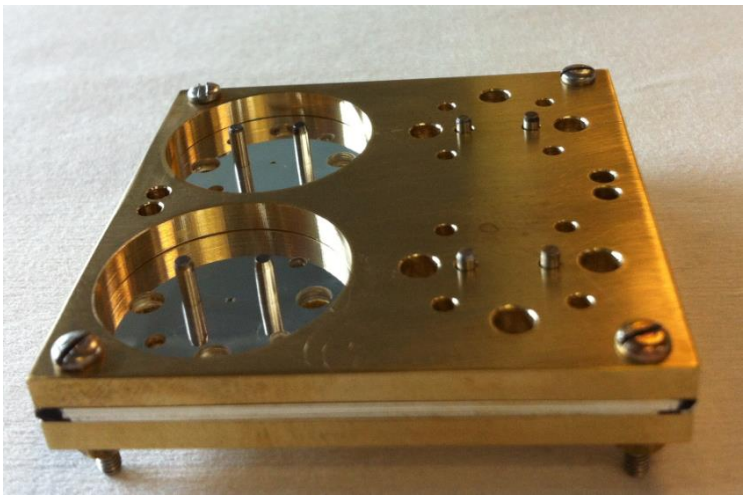

Figure 5.8 Final Assembled WR-3 Band SU-8 Waveguide Butler Matrix with Bends

The S parameter measurement of the WR-3 band Butler Matrix is carried out on an Agilent E8361A Network Analyser with a WR-3 extension T/R module at test port 1 and a T module (receive only) at test port 2. A photograph of the measurement setup of the Butler Matrix is shown in Figure 5.9.

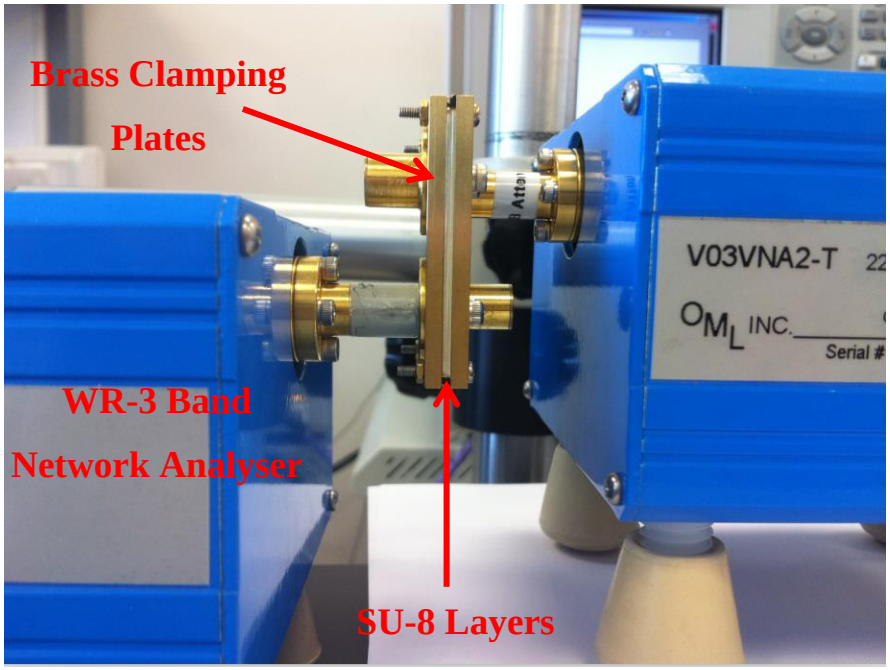

Figure 5.9 Measurement setup of the WR-3 Band Butler Matrix with Bends

A Short-Open-Load-Through (SOLT) calibration is taken before the measurement. During the measurement, port 1 and port 2 are connected to the Agilent E8361A Network Analyser, while port 3 and port 4 are connected to 50 Ω loads for impedance matching.

The measurement results show a very high reflection. Most of the power is reflected back. Several possible reasons may have caused this failure in the measurement. The three layers may not be aligned well, thus power will be reflected back when transmitted signal encounters the misalignments. The uneven surfaces caused by the fabrication process may lead to the power reflection between layers. The material will also absorb small amount of energy in the transmission. In the meantime, a bad calibration will also lead to a failure in the measurement. All the possible reasons will need future investigation on both the network analyser and the device itself.

Chapter 6

Micromachined Slotted Waveguide Antenna Array Design

The design of the slotted waveguide antenna array will be explained in this chapter. The theory of slot radiators will be introduced. Theoretical analysis of the antenna array will be given. These results are to be used as the initial values for the final optimisation of the antenna array.

The Butler Matrix is to be connected to a slotted waveguide antenna array to build the beamforming network. The slotted waveguide antenna is widely used in radar and communication systems [39]. It has the advantages that the radiating slots can be integrated into the feeding waveguide without a special matching network. The desired radiation pattern can be realized by controlling the dimensions and positions of the radiating slots. This type of antenna is easy for construction and is possible to be built with multi-layer structures. A slotted waveguide antenna designed to operate at 270 GHz is designed in this thesis. It is to be fabricated on metal-coated SU-8 thick resist and is designed to be built on three layers of SU-8 with an equal thickness of 0.432mm.

6.1 Theory of Slot Radiators

The electromagnetic field propagating inside the waveguide is associated with the surface current distributed over boundary of the waveguide [39]. The electric field, the magnetic field and the surface current distribution for a rectangular waveguide propagating TE_{10} mode are shown in Figure 6.1.

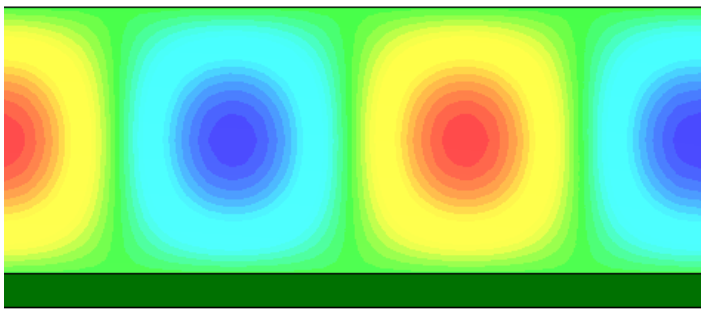

(a)

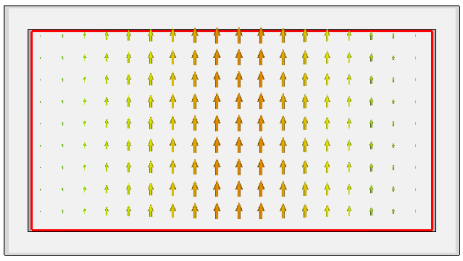

(b)

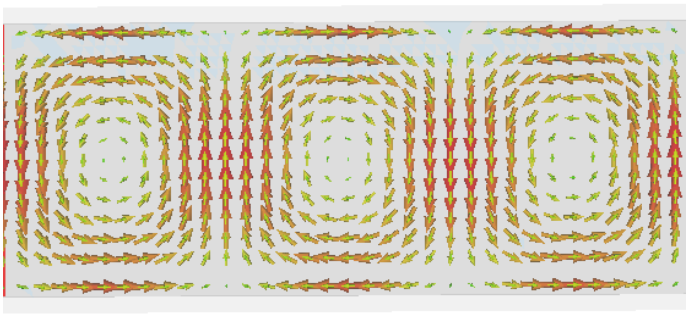

(c)

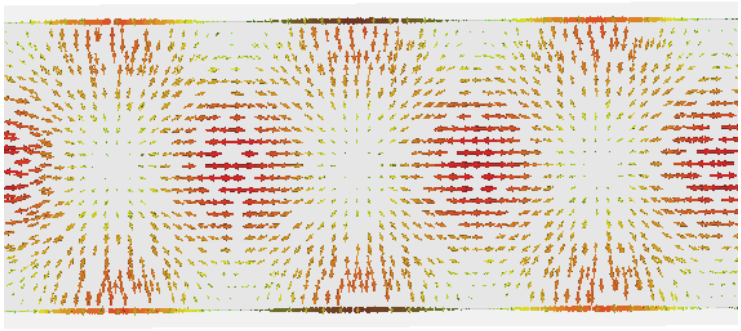

(d)

Figure 6.1 Fields and Currents of a TE_{10} Mode Rectangular Waveguide Simulated by CST

(a) Longitudinal View of the E-Field for a Rectangular Waveguide Propagating TE_{10} Mode. (b) Cross-Section View of the E-Field for a Rectangular Waveguide Propagating TE_{10} Mode. (c) Longitudinal View of the H-Field for a Rectangular Waveguide Propagating TE_{10} Mode. (d) Surface Current Distribution for a Rectangular Waveguide Propagating TE_{10} Mode.

The surface current is regarded as a shield preventing the electromagnetic field from radiating into the exterior region of the waveguide. To realize an antenna, the incident powers need to penetrate through the waveguide. A slot is introduced here to perturb the distribution of the

surface current, so that the power can radiate through free space. The strength of the radiating power depends on the intercepted current density. The slot that cuts in a direction transverse to the current lines will have a significant influence on the current distribution, forcing the current to flow around the slot. This type of slot is defined as a radiating slot. On the contrary, the slot cuts in the same direction along the current lines or in a direction that the current is zero will have little influence on the current distribution. This is defined as a non-radiating slot [41].

Figure 6.2 shows a series of slots cutting through the wall of a rectangular waveguide, according to the surface current distribution in Figure 6.1 and the radiation theory above, slot *c* and slot *e* cut along the current lines and are regarded as non-radiating slots, while the others all cut in the directions intercept the current lines, and these are regarded as radiating slots.

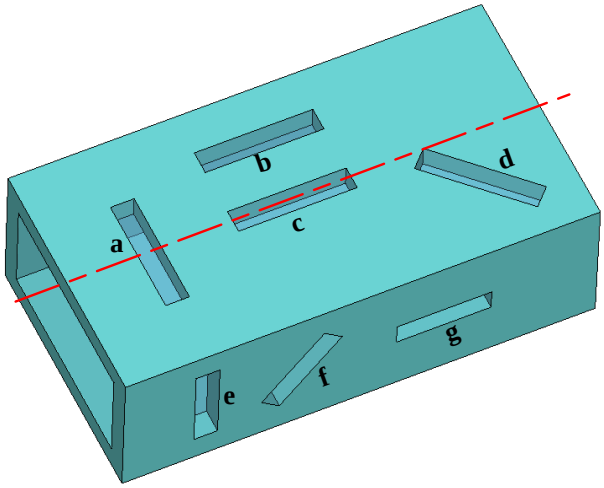

Figure 6.2 Slots in the Wall of a Rectangular Waveguide

6.2 Micromachined Slotted Waveguide Antenna Design

The slotted waveguide antenna discussed in this thesis is constructed by the type *b* slot in Figure 6.2. This slot cuts in the longitudinal direction of the rectangular waveguide. It also fits the orientation of the feeding waveguide connected with the Butler Matrix. The antenna is designed to be built on multi-layer structures. The feeding waveguide is built on one SU-8 layer while the slots are cut into the top SU-8 layer. A schematic diagram of the antenna is shown in Figure 6.3.

Each slot has a thickness of *t* which is 0.432mm for the SU-8. The length of the slot is *l* and the width is *w*, the offset of the slot from the centre line is *x*. The distance between adjacent slots is *d*. Calculations of these dimensions will be provided in details. The results will be used to build a model of the antenna in CST Microwave Studio and final optimisation gets the desired radiation pattern.

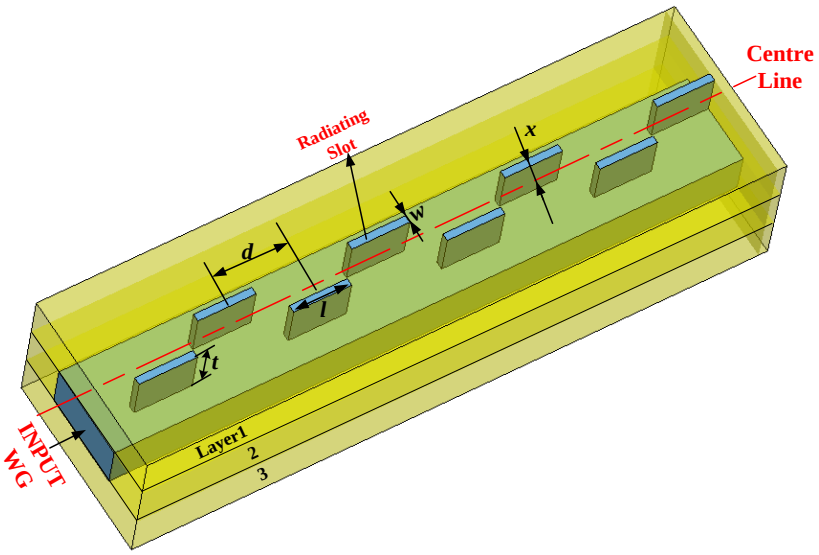

Figure 6.3 Schematic Diagram of the Slotted Waveguide Antenna

6.2.1 Theoretical Calculation of Slot Radiators

The basic theory of the slot radiators in the rectangular waveguide were given by Stevenson [42]. In general, the slot radiators are equivalent to the series or shunt elements in a transmission line. Instead of analyzing the field distributions around the slots, the equivalent circuit method is used here. The equivalent circuit of type *b* slot radiator is shown in Figure 6.4 [43].

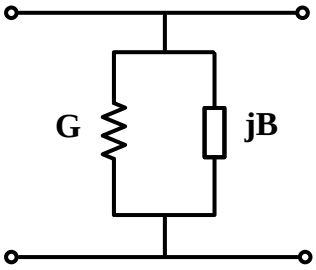

Figure 6.4 Equivalent Circuit of Type b Slot in Figure 6.2

The longitudinal slot is equivalent as a shunt admittance, which has both real part (conductance) and imaginary part (susceptance). If the admittance of the slot is real at the operating frequency, the total admittance of the slots will be the sum of each slot admittances added together. Both the conductance (G) and the susceptance (B) of the slot are determined by the resonant length of the slot according to [41]. The normalized conductance and susceptance versus the resonant length of slot is plotted in Figure 6.4 which is reproduced from [43], in which Gr is the normalized admittance factor define as 1/50.

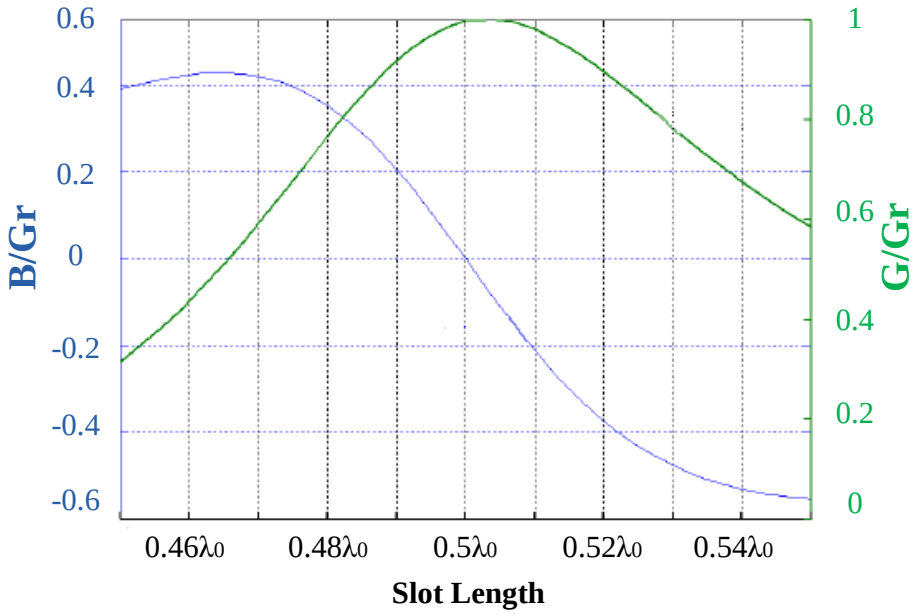

Figure 6.5 Normalized Admittance of a slot versus Slot Length (This figure is reproduced from [43])

From Figure 6.5, to make the admittance of the slot real at the operating frequency, the slot length should be around half wavelength, while the slot width should be at least five times smaller than the slot length [41].

Another problem to be considered in this design is the network matching. This type of antenna has the advantage that the radiating slots can be integrated into the feeding waveguide without a special matching network. By making the total admittance from all slots equal to the intrinsic admittance of the waveguide, the network will be matched and has lowest VSWR (Voltage Standing Wave Ratio) [44], given below:

$$\sum_{n=1}^{N} g_n = 1 \tag{6.1}$$

Where N is the total number of slots, g_n is the conductance of the nth slot normalized to the waveguide admittance, g_n is given by [44]:

$$g_n = \frac{G_{slot}}{G_{WG}} = [2.09 \frac{\lambda_g}{\lambda_0} \cdot \frac{a}{b} \cdot \cos^2 \frac{\pi \lambda_0}{2\lambda_g}] \sin^2 \frac{\pi x}{a} \tag{6.2}$$

a and b are the dimensions of the waveguide, which is 0.864mm and 0.432mm in this design. x is the offset of the slot from the centre line of the waveguide, λ_0 is the wavelength in free space and λ_g is the guided wavelength, given by [42]:

$$\lambda_g = \frac{\lambda_0}{\sqrt{1 - (\frac{\lambda_0}{2a})}} \tag{6.3}$$

Figure 6.6 shows the g_n versus the offset distance x.

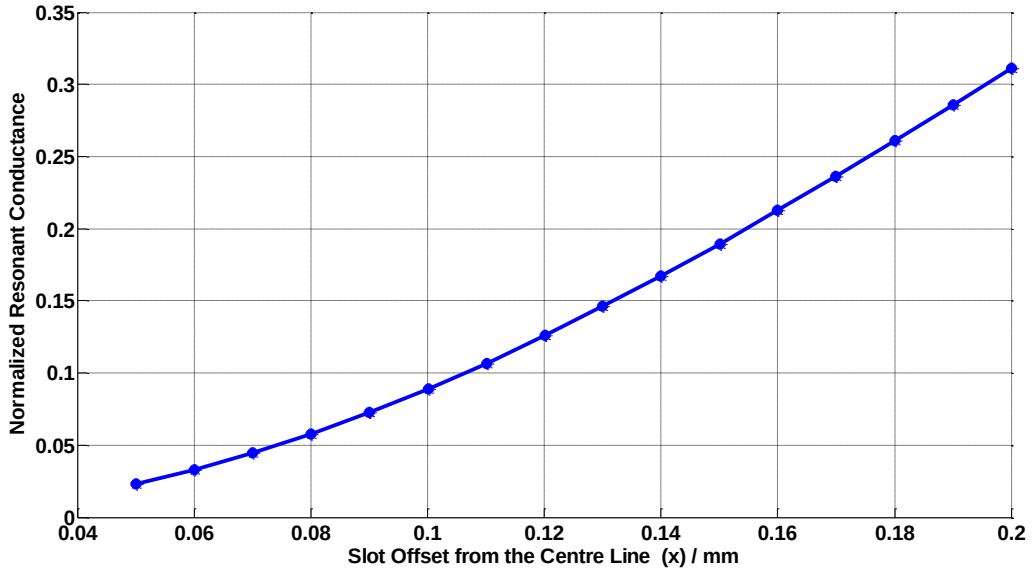

Figure 6.6 Normalized Conductance versus Slot Offset from Centre Line from Thoery

From Figure 6.6, the normalized conductance will be larger if the radiating slot is further away from the centre line. Assuming the total number of slots (N) in this antenna is eight, from Equation (6.1), the normalized conductance should be 0.125 for a matching network, and the offset distance x can be computed by Equation (6.2).

For an eight-slot antenna operating at 270 GHz, the theoretical dimensions of the slot radiator can be calculated by the equations above, and these values are listed in Table 6.1.

Slot length: l	0.555 mm
Slot width: w	0. 100 mm
Slot depth: t	0.432 mm
Slot displacement from centre line: x	0.119 mm

Table 6.1 Summary of the Slot Dimensions in Theory

6.2.2 Antenna Realization Using Slot Radiators

The antenna will be realized by these slot radiators explained above. After determining the dimensions of each slot, the distance between adjacent slots (*d*), the number of slots (*N*) and the radiation patterns of the antenna are to be considered. The spacing *d* between slots along the waveguide must be equal to half guided wavelength ($\lambda_g/2$) [42]. This will cause a 180° phase shift between slots. However, the slots are placed on the opposite sides of the centre line on the waveguide, by choosing the proper value of the offset distance *x*, it will cause another 180° phase shift, making them back in phase again. The slot number *N* has a relationship with the antenna gain and the beamwidth of the radiation pattern:

$$Gain = 10 \times \log(\frac{N \cdot d}{\lambda_0}) \ dB \tag{6.4}$$

$$Beamwidth = 50.7 \times \frac{\lambda_0}{\frac{N}{2} \cdot d} \ \ Degree \tag{6.5}$$

Figure 6.7 and Figure 6.8 are the plots of the relationship between the number of slots (*N*) and antenna gain / beamwidth.

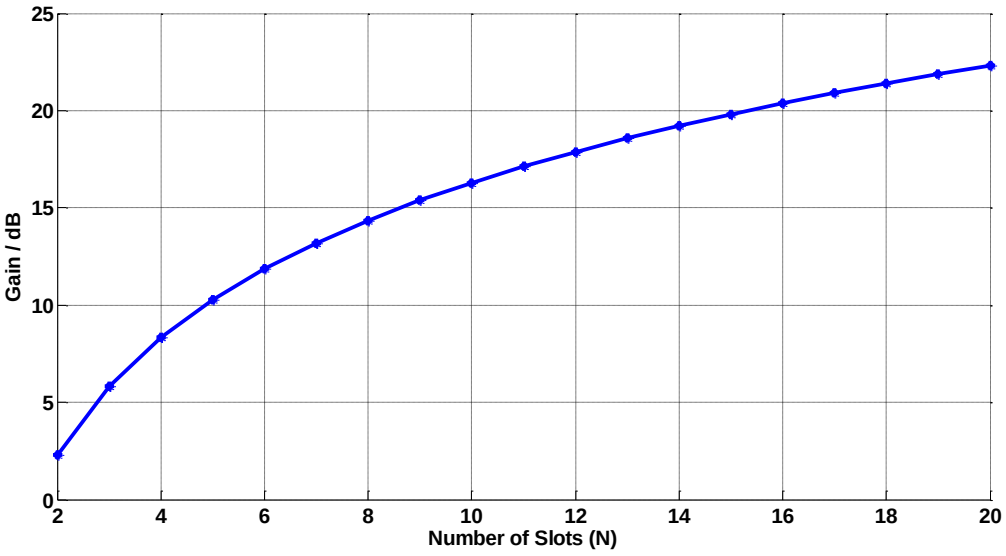

Figure 6.7 the Relationship between the Numbers of Slot and Antenna Gain from Thoery

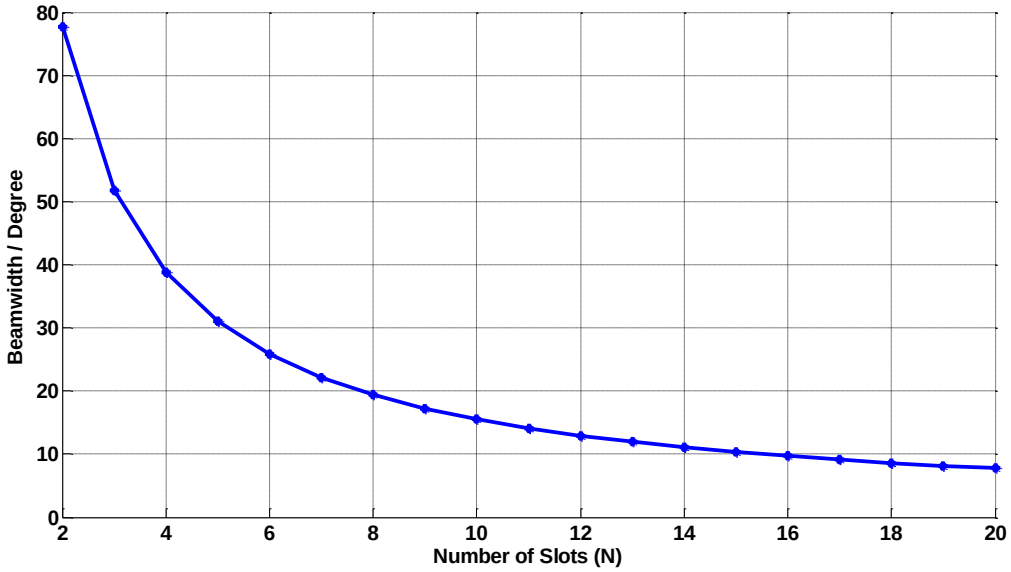

Figure 6.8 the Relationship between the Numbers of Slot and Antenna Beamwidth from Thoery

From Figure 6.7 and 6.8, it can be seen with the number of slots increasing, the antenna gain will increase. This will also cause a decrease in the beamwidth. The antenna gain should be large enough to make sure enough power has been radiated in the desired direction. Meanwhile, the beamwidth should be wide enough for the signals to be detected. In order to keep a balance between these two parameters, the number of slots (N) is chosen to be eight in this design.

Another thing to be considered is the termination of the antenna. To make sure the end of the waveguide will not affect the matching of the network, a short circuit condition is considered here. In this case, the distance between the centre of the last slot and the termination of the waveguide is $\lambda_g/4$ [44].

The calculated dimensions of the antenna are listed in Table 6.2 below.

Waveguide dimensions: a x b	0.864 mm x 0.432 mm
Number of slots: N	8
Slot length: l	0.555 mm
Slot width: w	0. 100 mm

Slot depth: t	0.432 mm
Separation between adjacent slots: d	0.725 mm
Slot offset from centre line: x	0.119 mm
Last slot to the termination: $\lambda_g/4$	0.362 mm

Table 6.2 Summary of the Antenna Design Dimensions by Calculation

6.2.3 Final Optimisation

The slotted waveguide antenna shown in Figure 6.3 is simulated by the CST Microwave Studio with the dimensions listed in Table 6.2. After the optimisation process of the CST, the simulation results are shown below in Figure 6.9.

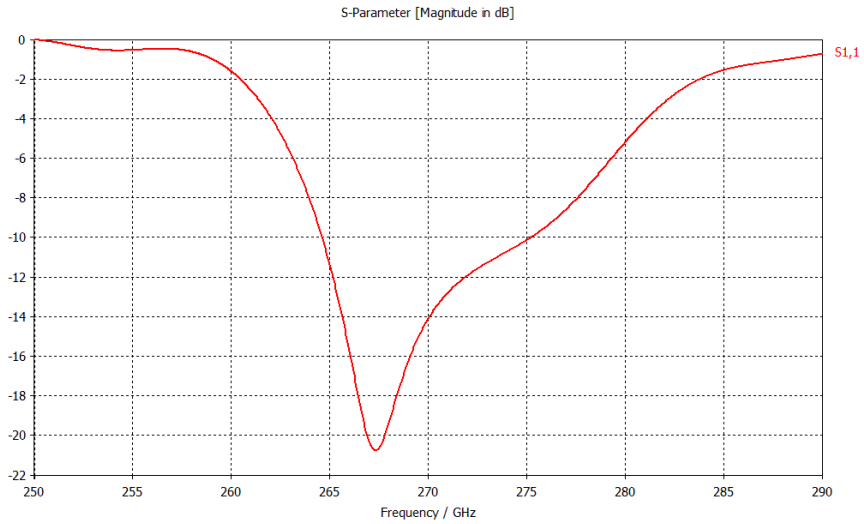

Figure 6.9 Simulated S_{11} Parameter

From this figure, the antenna radiates at about 268 GHz. The S_{11} parameter is better than -10 dB between 264 GHz and 275 GHz, indicating a good match in the operating frequency.

The simulated H and E plane radiation patterns are shown in Figure 6.10 and Figure 6.11 respectively.

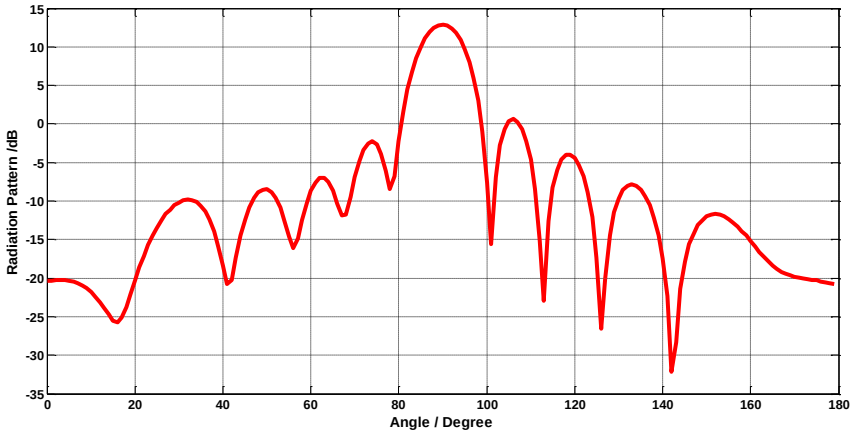

Figure 6.10 Simulated H Plane Radiation Pattern

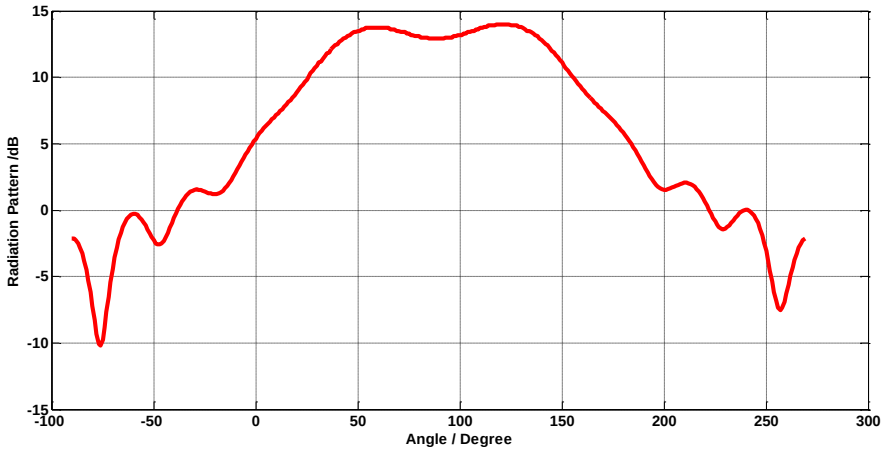

Figure 6.11 Simulated E Plane Radiation Pattern

An H-plane radiation pattern with a 12.9 dB realized gain and a low Side Lobe Level (SLL) of -12.3 dB are achieved. The 3 dB beamwidth of this antenna is 9.8 degree. From these simulation parameters above, this type of antenna will be appropriate for connection to the Butler Matrix to build whole beamforming network. The main dimensions of the antenna after the optimisation is shown in Table 6.3

Waveguide dimensions: *a* x *b*	0.864 mm x 0.432 mm
Number of slots: *N*	8
Slot length: *l*	0.546 mm

Slot width: w	0.070 mm
Slot depth: t	0.432 mm
Separation between adjacent slots: d	0.730 mm
Slot offset from centre line: x	0.110 mm
Last slot to the termination: $\lambda_g/4$	0.360 mm

Table 6.3Summary of the Antenna Design Dimensions after Optimisation

This chapter mainly deals with the design of the micromachined slotted waveguide antenna. It can be built using multi-layer structure. Theoretical calculations and analytical optimisations are both taken. This antenna will be used to build a 2-element antenna array and connected with the Butler Matrix. More details of the whole beamforming network will be explained in the next chapter.

Chapter 7 Micromachined Butler Matrix with Antenna Arrays

7.0 Introduction

This chapter deals with the beamforming network using the Butler Matrix configuration. The coupled resonator waveguide Butler Matrix presented in the previous chapters is to be connected with the slotted waveguide antenna array. The schematic diagram of the network is shown in Figure 7.1. In which, Port 1 and port 4 are input ports, while port 2 and port 3 are connected with the antenna array.

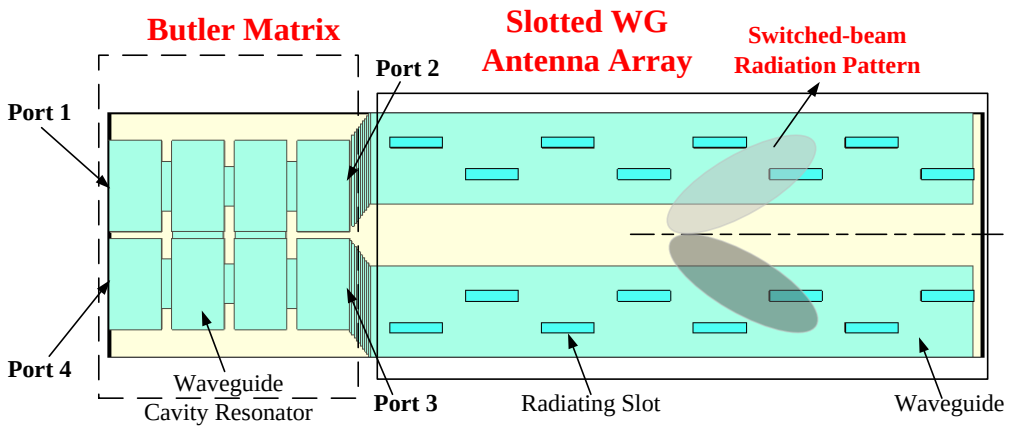

Figure 7.1 Schematic Diagram of the Butler Matrix with the Antenna Array

This beamforming network has the feature of transmitting signals at different angles when exciting it at different input ports. The distance between the antennas is designed to implement the desired beams. The Sidelobe Level (SL) needs to be controlled to a minimal value.

By applying the signal at each input port (port 1 and port 4 in Figure 7.1), the *N* x *N* Butler Matrix will produce output signals with equal power and a phase shift between adjacent output ports the phase shift is given by [15]:

$$\delta_i = 2\pi i / N \tag{7.1}$$

For i = ± 1/2, ± 3/2, ± 5/2… ± (N-1)/2.

As a result, the Butler Matrix can produce *N* orthogonal beams at the outputs when it is connected to the antenna array. Figure 7.2 is the schematic diagram of a 4x4 Butler Matrix with an antenna array included on the right of the figure.

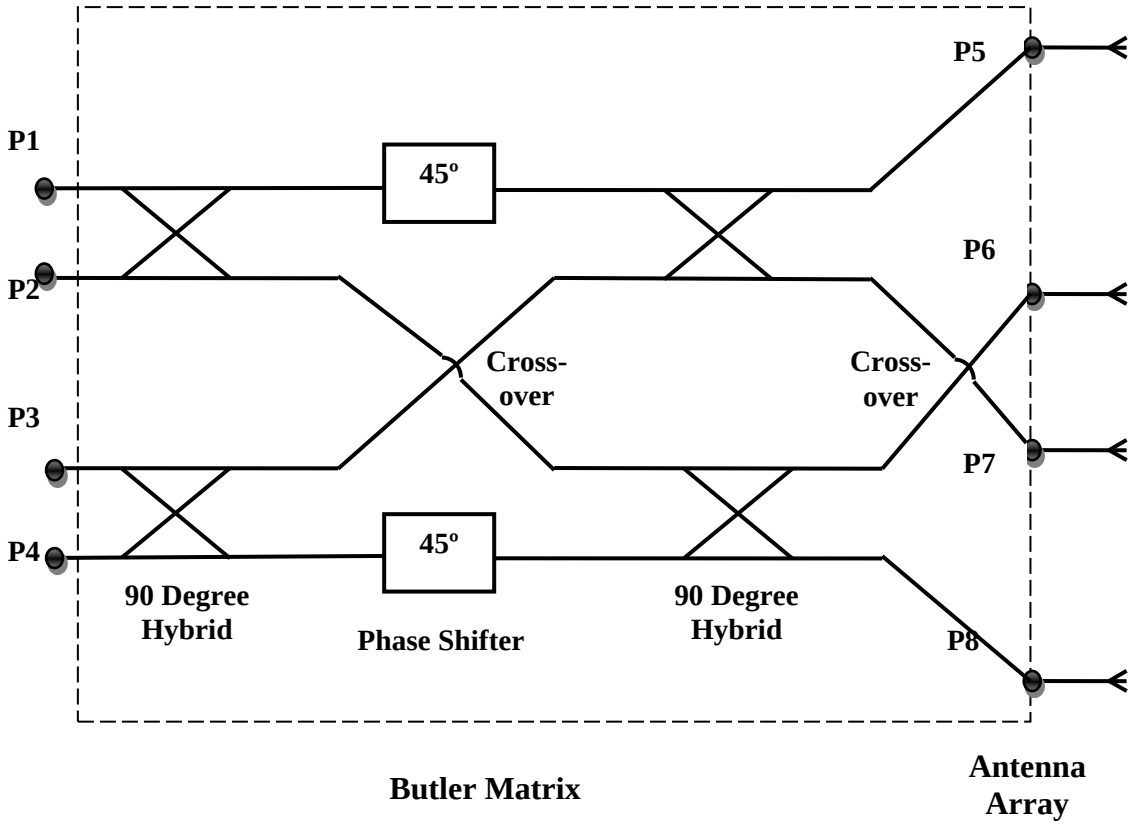

Figure 7.2 Schematic Diagram of a 4x4 Butler Matrix with Antenna Array

The phase difference of the 4x4 Butler Matrix computed by Equation (7.1) is listed in Table 7.1.

	Input P1	**Input P2**	**Input P3**	**Input P4**
Output P5	-45º	-135º	-90º	-180º
Output P6	-90º	0º	-225º	-135º
Output P7	-135º	-225º	0º	-90º
Output P8	-180º	-90º	-135º	-45º
phase shift between adjacent	-45º	135º	-135º	45º

output ports				

Table 7.1 Theoretical 4x4 Butler matrix phase difference between input and output

A design of a 2 x 2 Butler Matrix is presented in this thesis. The system is built by a single coupler as shown in Figure 7.1. The phase difference at two different ports according to Equation (7.1) is ±90º. The phase difference is listed in Table 7.2.

	Input P1	**Input P4**
Output P2	0º	0º
Output P3	90º	-90º
phase shift between adjacent output ports	90º	-90º

Table 7.2 Theoretical 2x2 Butler matrix phase difference between input and output

The radiation patterns of the antenna array will be discussed in the next section before simulating it with the Butler Matrix to describe the whole antenna system.

7.1 Computed Radiation Pattern with Antenna Array

The radiation pattern of the antenna array can be found by the pattern multiplication [45]:

Array pattern = Single unit pattern x Array Factor (AF) (7.2)

In which, the single unit pattern is identical and has been presented in the previous chapter, the normalized array factor (AF) can be calculated by [46]:

$$\mathrm{AF}=\left|\frac{\sin(N\pi\frac{d}{\lambda}(\sin\theta-\sin\theta_0))}{N\pi\frac{d}{\lambda}(\sin\theta-\sin\theta_0)}\right| \quad (7.3)$$

Where N is the number of antenna elements, d is the distance between adjacent elements, and λ is the wavelength at the free space. θ_0 is the beam angle which can be calculated by the following equation [46]:

$$\theta_0 = \sin^{-1}(\frac{\beta\lambda}{2\pi d}) \qquad (7.4)$$

Where β is the propagation constant and $\beta = 2\pi / \lambda$. It has been discussed in the previous chapter. The array factor of a two element array with a distance of half wavelength plotted by the equations above is shown in Figure 7.3.

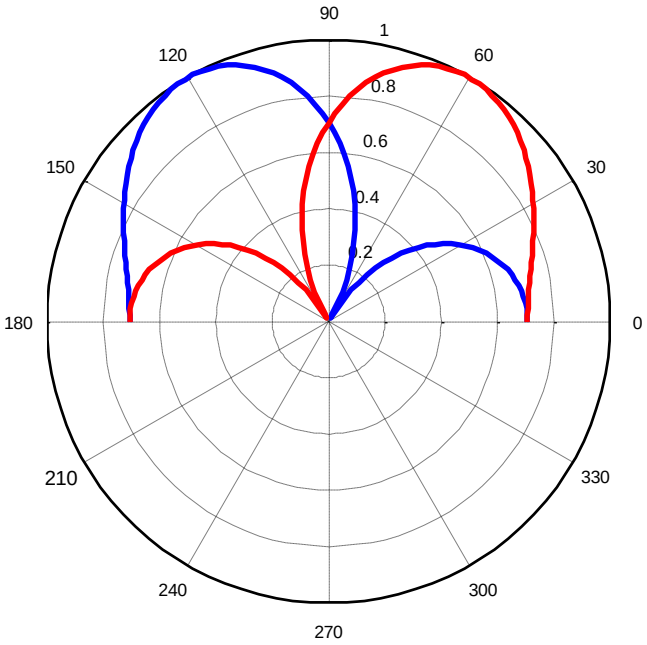

Figure 7.3 Calculated Array Factor of 2 Element Array Separated by $\lambda/2$

The red curve is the array factor of the radiation pattern when feeding in port 1, while the blue curve is the array factor when feeding the signal in port 4.

The half wavelength distance for the system operating at 270 GHz is 0.555 mm. This is smaller than the WR-3 band rectangular waveguide dimension, which is 0.864 mm for the longer side. Due to this, the distance between the antennas needs to be increased to fit the waveguide dimensions. The array factor of a two element array with a distance between the waveguides of 0.75λ, 0.875λ and 1λ are plotted using Equation (7.3) in Figure 7.4 (a), (b),

(c) respectively. Here, the red curve is the array factor of the radiation pattern when feeding in port 1, while the blue curve is the array factor when feeding the signal in port 4.

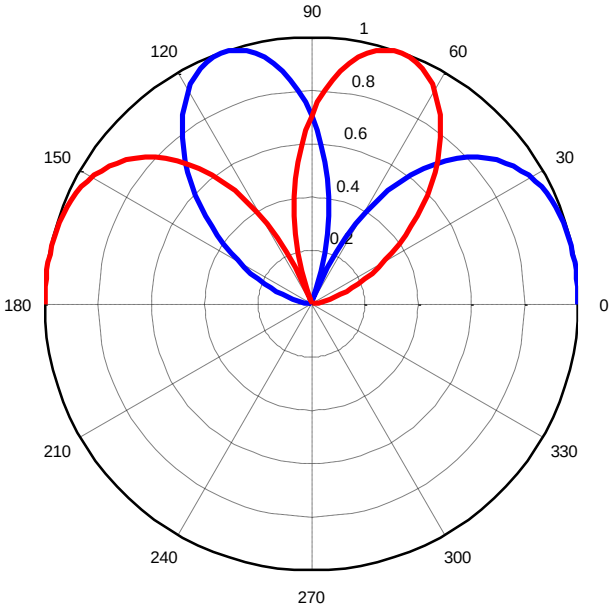

Figure 7.4 (a) Calculated Array Factor of 2 Element Array Separated by 0.75λ

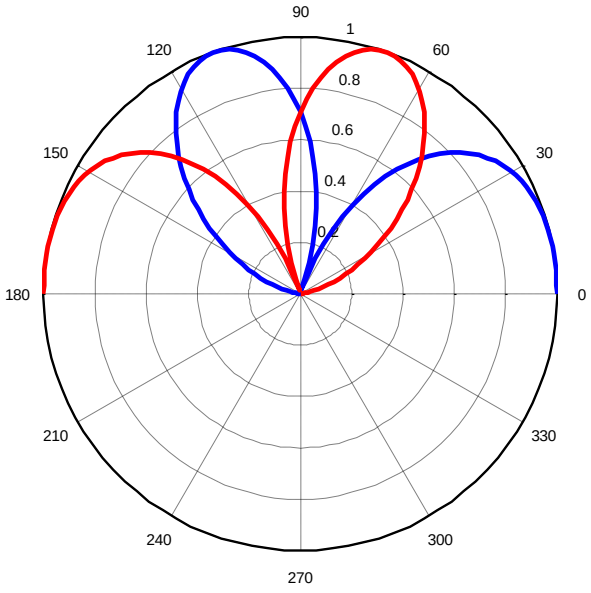

Figure 7.4 (b) Calculated Array Factor of 2 Element Array Separated by 0.875λ

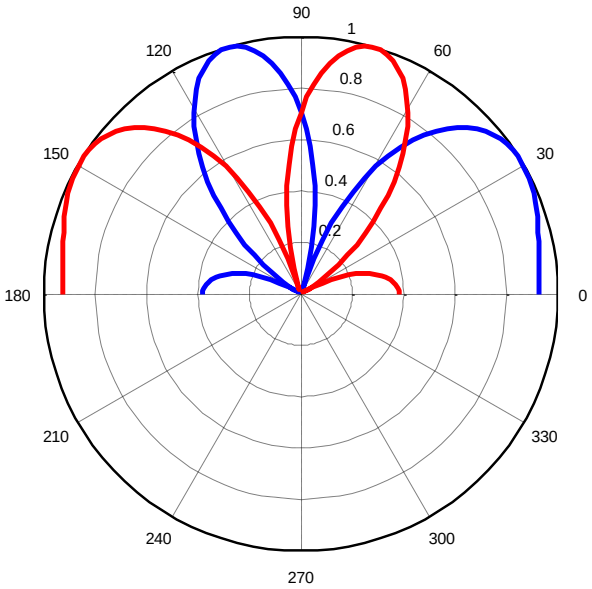

Figure 7.4 (c) Calculated Array Factor of 2 Element Array Separated by 1λ

In Figure 7.4, a grating lobe is induced due to the increasing distance between the antennas. As the distance increased further, the grating lobe effect will be more obvious. So as the two waveguide slot antennas cannot be place a half wavelength apart we need to increase the spacing and choose a convenient spacing larger than half a wavelength. Thus, a way to decrease the grating lobes as well as the sidelobe level needs to be considered. The method of sidelobe reduction and the improvement of the radiation patterns will be discussed in the next sections.

7.2 Sidelobe Reduction

According to antenna array theory [47], the optimum sidelobe level of an n uniform array is about 13.6 dB [48]. However, there are effects of mismatch between the antenna and the feeding network as well as the mutual coupling between the radiating elements. In reality, it is difficult to reach a sidelobe level of less than 10 dB [48]. Figure 7.5 (a) and (b) are the 3D radiation

patterns of the beamforming system before any sidelobe reduction process. The distance between two antennas is one wavelength. In which Figure 7.5 (a) is the radiation pattern when feeding from port 1, while Figure 7.5 (b) is the radiation pattern when feeding from port 4. Figure 7.6 (a) and (b) are the corresponding radiation patterns in 2D version. Figure 7.6 (a) is the pattern feeding from port 1and Figure 7.6 (b) is the pattern feeding from port 4.

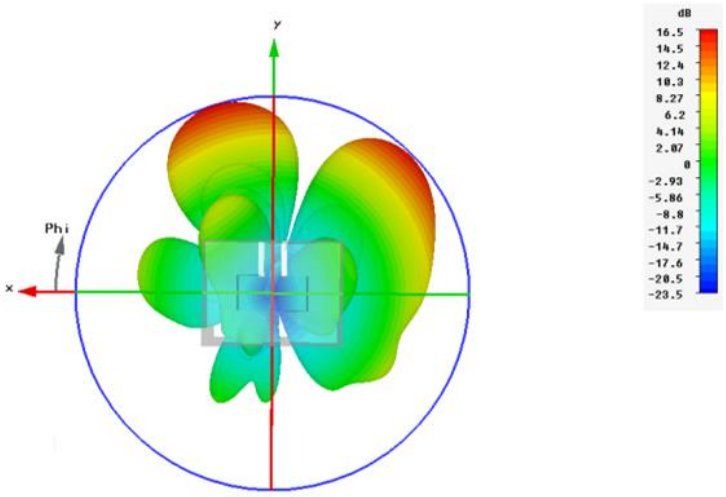

Figure 7.5 (a) Simulated 3D Radiation Pattern of the Beamforming Network Feeding From Port 1

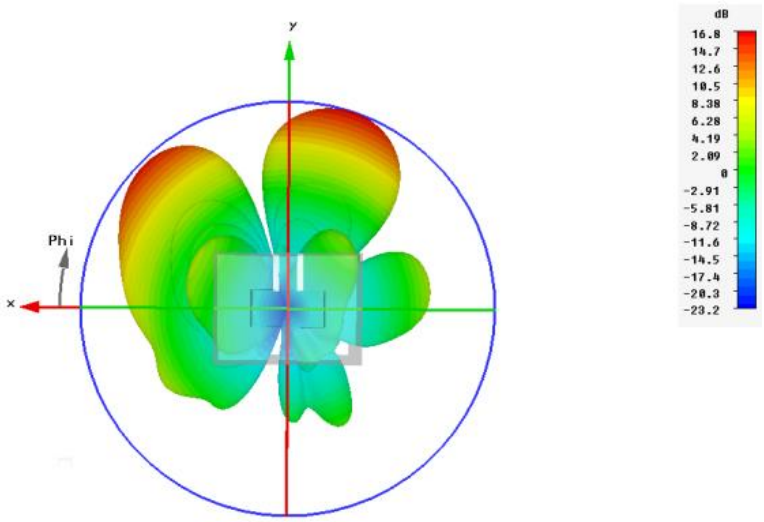

Figure 7.5 (b) Simulated 3D Radiation Pattern of the Beamforming Network Feeding

From Port 4

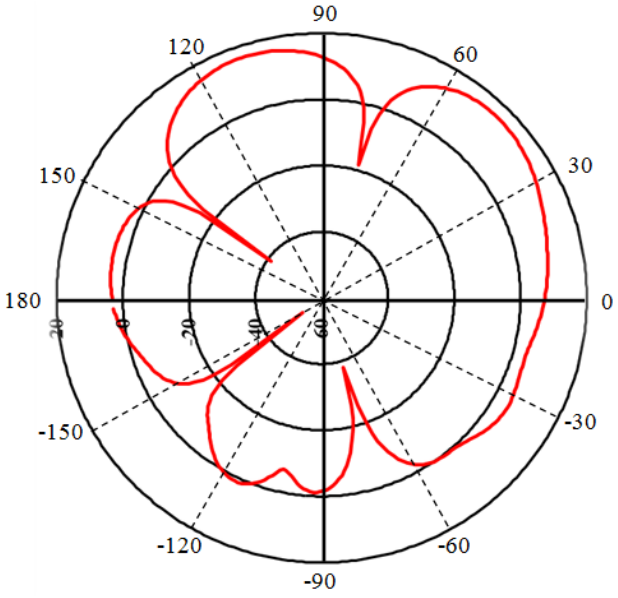

Figure 7.6 (a) Simulated 2D Radiation Pattern of the Beamforming Network Feeding

From Port 1

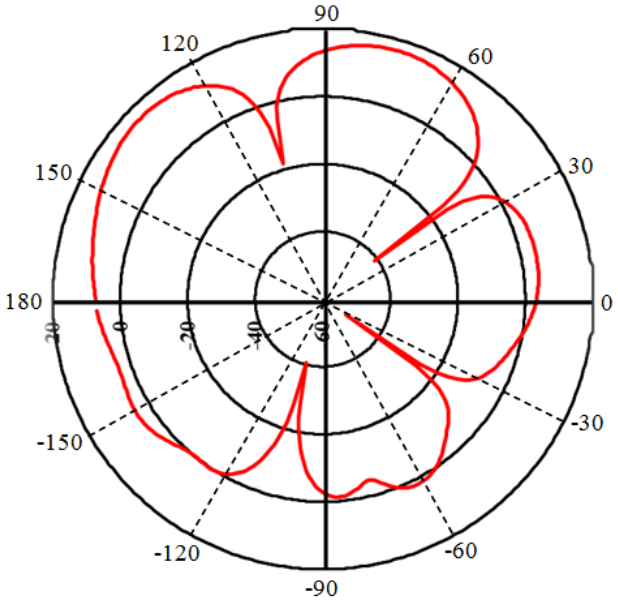

Figure 7.6(b) Simulated 2D Radiation Pattern of the Beamforming Network Feeding From Port 4

Form Figure 7.6 (a) above, when feeding from port 1 and separating the two antennas by a distance of one wavelength, the mainlobe has a realized gain of 16.8 dB at an angle of 110°, the grating lobe has a realized gain of 17.5 dB at an angle of 58°, and the sidelobe has a realized gain of 8 dB at an angle of 25°. The grating lobe and the sidelobe are too high compared with the mainlobe, thus sidelobe reduction has to be taken.

Several different ways of sidelobe reduction has been considered. A method of reducing the sidelobe level by non-uniform spacing between the antenna elements is introduced in [49]. However, this method has the drawbacks as: the half power beamwidth broadening at the expense of small reduction in the sidelobe level. Other methods such as improving the waveguide feeding network [50] has been applied to microstrip antennas, however it cannot be used in this design since the Butler Matrix has already been optimised first. In this thesis, we solve this problem by increasing the number of the radiating elements as shown in Figure 7.7.

The main dimensions of the antenna array after the optimisation is shown in Table 7.3. The results of the radiation patterns after sidelobe reduction will be shown in the section 7.3.

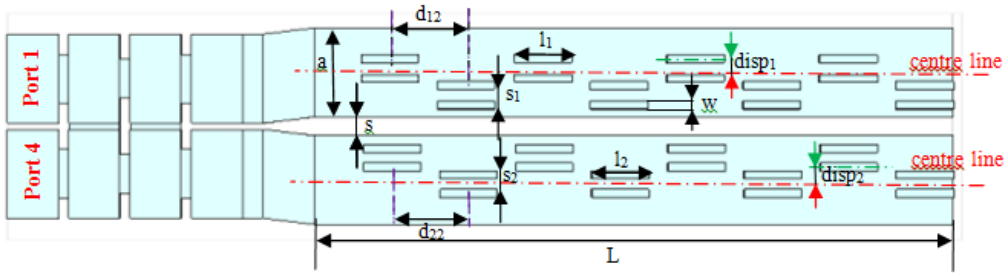

Figure 7.7 Schematic Diagram of the Butler Matrix with the Antenna Array after Sidelobe Reduction

Waveguide dimensions: a x b	0.864 mm x 0.432 mm
Number of slots: N	8
Slot length: l_1	0.559 mm
Slot length: l_2	0.557 mm
Slot width: w	0.078 mm
Separation between adjacent slots: d_{12}	0.741 mm
Separation between adjacent slots: d_{22}	0.738 mm
Separation between two arrays: s	0.189 mm
Slot offset from centre line: $disp_1$	0.090mm
Slot offset from centre line: $disp_2$	0.086mm
Separation between new radiating element and the original element: s_1	0.120 mm
Separation between new radiating element and the original element: s_2	0.169 mm
Total length: L	6.2 mm

Table 7.3 Summary of the Antenna Array Design Dimensions after Sidelobe Reduction

The slot number *N* has a relationship with the antenna gain and the beamwidth of the radiation pattern according to Equation (6.4) and (6.5) in chapter 6. The antenna gain should be large enough to make sure enough power has been radiated in the desired direction. Meanwhile, the beamwidth should be wide enough for the signals to be detected. In order to keep a balance between these two parameters, the number of slots (N) is chose to be eight in the design.

The initial values in the optimisation was taken from the dimensions in Table 6.2 with only one series of slot radiators. When adding the second series of radiating elements, the distance between these two series need to be adjusted first to get a desired sidelobe level. The other parameters will be slighted changed for further optimisation.

7.3 Improved Radiation Pattern with Antenna Array

The beamforming network using the Butler Matrix configuration in Figure 7.7 was simulated by CST Microwave Studio, and the return loss of this network is shown in Figure 7.8. At the operating frequency of 270 GHz, the return loss is about -20.5 dB, which is acceptable in the design of the antenna array. Although there also power transmitted at about 255 GHz, 258 GHz and at 287 GHz, these can be ignored when comparing with the power transmitted at the operating frequency.

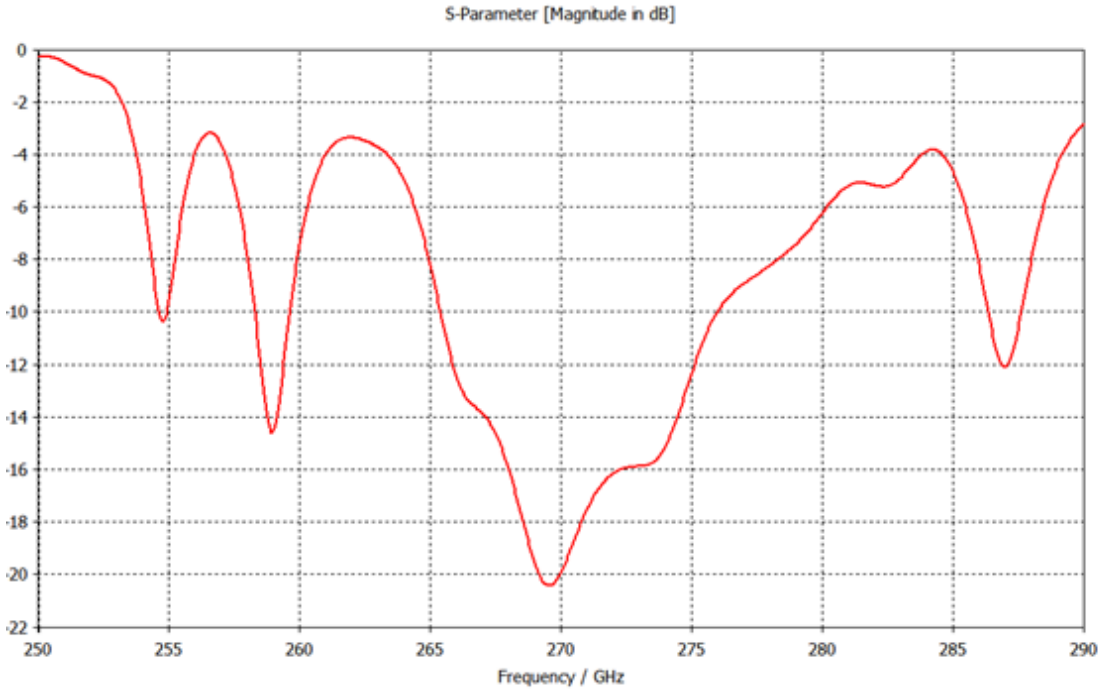

Figure 7.8 Return Loss of the Beamforming Network from Simulation

The 3D view radiation patterns of the beamforming network after the sidelobe reduction are shown in Figure 7.9 (a) and (b). Here Figure 7.9 (a) is the radiation pattern when feeding from port 1, while Figure 7.9 (b) is the radiation pattern when feeding from port 4. In order to get the numerical value of the sidelobe level, the farfield radiation pattern has also been plotted in the y-z plane (ϕ=90°), which are shown in Figure 7.10 (a) and (b). In which Figure 7.10 (a) is the radiation pattern when feeding from port 1, while Figure 7.10 (b) is the radiation pattern when feeding from port 4.As we can see, the sidelobe has been significantly reduced.

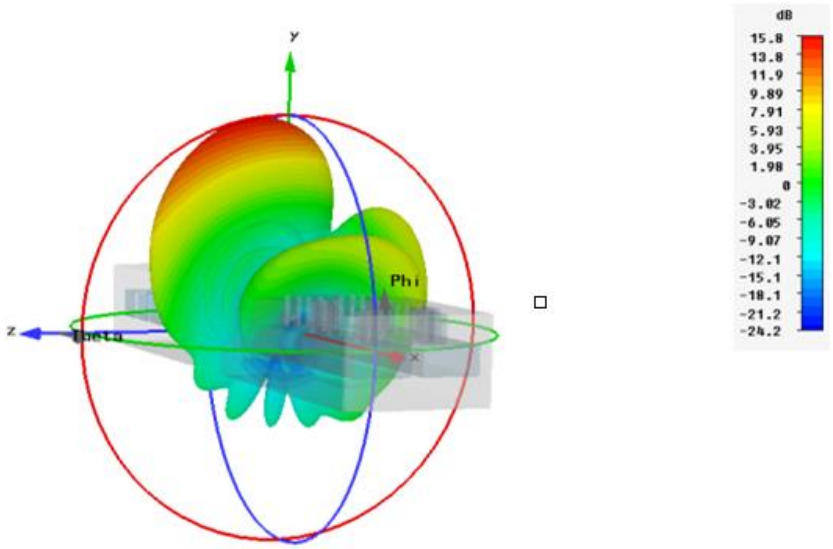

Figure 7.9 (a) Simulated 3D View Radiation Pattern of the Beamforming Network Feeding From Port 1

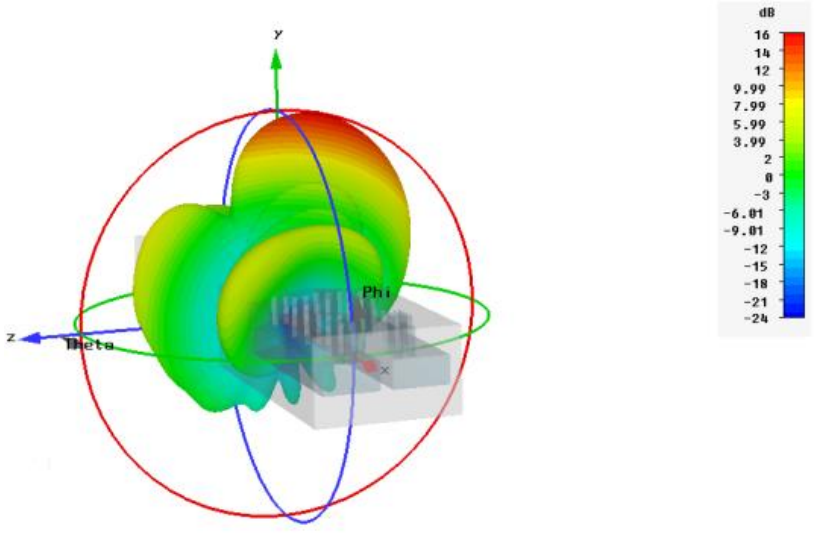

Figure 7.9 (b) Simulated 3D View Radiation Pattern of the Beamforming Network Feeding From Port 4

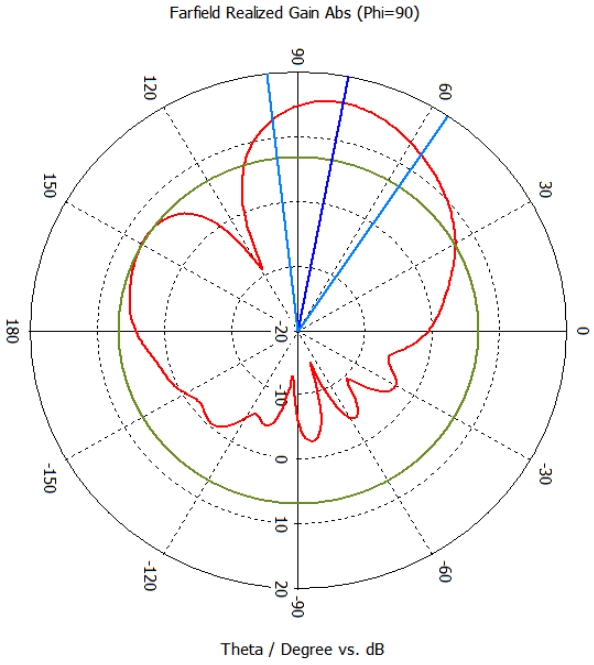

Figure 7.10 (a) Simulated Farfield Radiation Pattern in the y-z Plane of the Beamforming Network Feeding from Port 1

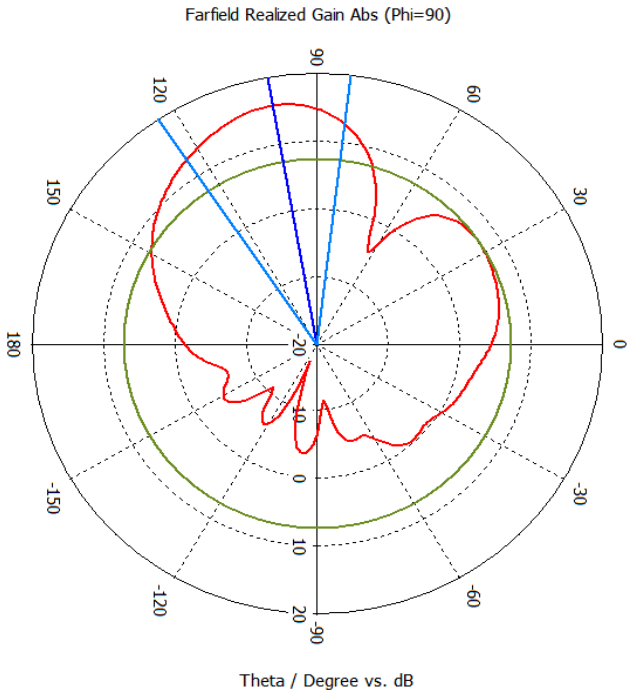

Figure 7.10 (b) Simulated Farfield Radiation Pattern in the y-z Plane of the Beamforming Network Feeding from Port 4

Compare the sidelobe level of Figure 7.10 with the previous simulation results in Figure 7.6. In Figure 7.10 (a), When feeding from port 1, the mainlobe reaches a level of 15.8 dB and in the direction of θ=100°, the sidelobe has a realized gain of 7.3 dB, the sidelobe level is -8.5 dB below the mainlobe and the half power beamwidth (HPBW) is 40.8°. The HPBW could be figured out by the radial lines in the plots above, the centre one points to the angle at mainlobe while the other two point to the angles of half power bandwidth. When feeding from port 4, the mainlobe reaches a level of 15.8 dB and in the direction of θ=79°, the sidelobe has a realized gain of 6.9 dB and the sidelobe level is -8.9 dB and the half power beamwidth (HPBW) is 40.8°. While in Figure 7.6, the mainlobe has a realized gain of 16.8 dB, the grating lobe has a realized gain of 17.5 dB and the sidelobe has a realized gain of 8 dB. One can see that, the grating lobe

has been eliminated by this method and the sidelobe has been reduced. Compare the simulated result with the theoretically calculated result in Figure 7.4 (c), the mainlobe from theory should be at 80° and 100°, which is very close to the simulation results. In the meantime, the sidelobe has been significantly reduced to realize the requirements of the beamforming network.

In this chapter, the beamforming network using the Butler Matrix configuration has been explained. Sidelobe level problems have been encountered and are solved by increasing the number of radiating elements. However, the results can be further optimised to decrease the sidelobe more significantly. Other methods of the sidelobe reduction may be considered. The manufacturing of the antenna array will be discussed in the part of future work in next chapter.

Chapter 8 Conclusions and Future Work

8.1 Conclusions

The work presented in this thesis focused on the design on a WR-3 band Butler Matrix feeding a two-element slotted waveguide antenna array. The Butler Matrix is implemented by the coupled resonator structure. It is a technique based on the appropriate couplings between the inner couplers and the couplings between the couplers and the external ports. This technique has the advantage of being applied to any type of resonator despite its physical structure. In this thesis, the type of the resonator being used is the waveguide cavity resonator. The SU-8 photo-resist micromachining technology is implemented in the fabrication process.

This thesis can be divided into three major parts, which are resonator design, waveguide design and the antenna design. The first part explains the method of coupled resonator technique to implement the 90 degree hybrid coupler. The coupling matrix concept is explained in details. The coupling coefficients and external quality factors are derived from basic circuit theories. The scattering parameters of this coupled resonator 90 degree hybrid coupler are theoretically plotted for various fractional bandwidths. The theoretical plot of the scattering matrix demonstrated the coupling matrix concept to build a hybrid coupler.

The second part of the thesis explains the waveguide implementation of the coupled resonator 90 degree hybrid coupler in WR-3 band. The work presented in this thesis focused on the design of micromachining structures, thus the waveguide cavity resonator is chosen in this design due to its low attenuation during the propagation and high performance in millimetre-wave applications. The methods of extraction of coupling coefficients and external quality factors for this kind of structure are provided in details. Simulations of the Butler Matrix are taken by CST Microwave Studio. The simulation results match well with the theoretical predictions, which proves the coupled resonator technique to build the Butler Matrix. Thick SU-8 photo-resist micromachining technology is explained in this part and the bend design has to be introduced in

the realization of the whole structure on SU-8 layers. The micromachined coupled resonator Butler Matrix is fabricated and taken into measurement.

The last part of the thesis explains the design of the two-element micromachined slotted waveguide antenna array and the implementation of the beamforming network. The principles of slot radiators and the realization of the waveguide antenna by these slot radiators are discussed in details. The methods of sidelobe reduction are taken into consideration in the assembly of the beamforming network with the antenna array. Final optimised results are given after taking the sidelobe reduction.

8.2 Future Work

The work on the fabrication of the Butler Matrix should be pursed further. The air gap between bonded layers are likely to lead to increased insertion losses due to the energy leakage. For single SU-8 layer fabrication process, the layers are processed in the photolithographic procedure, then released from silicon substrate and silver coated separately. In practice, the surfaces of the SU-8 layers are not perfectly flat, when bonded together, there will be air gap between the layers, which will increase the insertion loss. Better fabrication process needs to be taken to get a better measurement result.

References

[1] Hosako I., Sekine N., Patrashin M., *et al*, 'At the Dawn of a New Era in Terahertz Technology,' *Proceedings of the IEEE*, vol. 95, no. 8, pp.1611-1623, 2007.

[2] Biber S., Schur J., Hofmann A., Schmidt L. P., 'Design of New Passive THz Devices Based on Micromachining Techniques,' *MSMW Symposium Proceedings*, vol. 1, pp. 26-31, 2004.

[3] Lancaster M.J., Zhou J., Ke M., *et al*, 'Design and High Performance of a Micromachined K-Band Rectangular Coaxial Cable,' *IEEE Transactions on MTT*, vol. 55, no. 7, 1548-1553, 2007.

[4] Wincza K., Gruszczynski S., Sachse K., 'Ultrabroadband 4 x 4 Butler Matrix with the Use of Multisection Coupled-line Directional Couplers and Phase Shifters,' *Microwaves, Radar and Remote Sensing Symposium*, pp. 118-122, 2011.

[5] Ho M., Stuber G.L., Austin M. D., 'Performance of Switched-Beam Smart Antennas for Cellular Radio Systems,' *IEEE Transactions on Vehicular Technology*, vol. 47, no. 1, pp. 10-19, 1998.

[6] Nedil M., Denidni T.A., Talbi L., 'Novel Butler Matrix Using CPW Multilayer Technology,' *IEEE Transactions on MTT*, vol. 54, no. 1, pp. 499-507, 2006.

[7] Wincza K., Gruszczynski S., Sachse K., 'Integrated four-beam dual-band antenna array fed by broadband Butler matrix,' *Electronics Letters*, vol. 43, no. 1, pp. 7-8, 2007.

[8] Derneryd A., Johannisson B., 'Adaptive base-station antenna arrays,' *Ericsson Review*, no. 3, pp. 132-137, 1999.

[9] Zak T., Sachse K., 'An integrated Butler matrix in multi-layer technology for multi-port amplifier applications,' *Proc. 14th International Conference on Microwaves, Radar & Wireless Communications*, vol. 1, pp. 59-62, 2002.

[10] Angelucci A., Audagnotto P., Corda P., Piovano B., 'Multiport power amplifiers for mobile-radio systems using microstrip Butler matrices,' *Proc. Antennas and Propagation International Symposium Digest*, vol. 1, pp. 628-631, 1994.

[11] Lipsky S. E., *Microwave Passive Direction Finding*, New York: John Wiley & Sons Inc., 1987.

[12] Pozar D. M., *Microwave engineering (*3rd ed.) New York: John Wiley & Sons Inc., 2005.

[13] Elliott R. S., *an Introduction to Guided Waves and Microwave Circuits*, New Jersey: Prentice-Hall, Inc., 1993.

[14] Maas S. A., *Microwave mixers*, Boston: Artech House, Inc., 1993.

[15] Mailloux R. J., *Phased array antenna handbook*, Boston: Artech House, Inc., 2005.

[16] Corona A., Lancaster M. J., 'A High-Temperature Superconducting Butler Matrix,' *IEEE Transactions on Applied Superconductivity*, vol. 13, no. 4, pp. 3867-3872, 2003.

[17] Hong J. S. and Lancaster M. J., *Microstrip filters for RF/microwave applications*, New York: John Wiley & Sons Inc., 2001.

[18] Sanadi A.B., Ramesh M., Kalghatgi A.T., 'Simplified Design and Analysis Method for a Waveguide Iris Filter,' *International Journal of RF and Microwave Computer-Aided Engineering*, vol. 9, iss. 2, pp. 150-154, 1999.

[19] Accatino L., Bertin G. and Mongiardo M., 'A Four-Pole Dual Mode Elliptic Filter Realized in Circular Cavity Without Screws,' *IEEE Transactions on MTT*, vol. 44, no. 12, pp. 2680-2687, 1996.

[20] Hong J. S. and Lancaster M. J., 'Couplings of Microstrip Square Open-loop Resonators for Cross-coupled Planar Microwave Filters,' *IEEE Transactions on MTT*, vol. 44, no. 12, pp. 2099-2109, 1996.

[21] Hong J. S. and Lancaster M. J., 'Theory and Experiment of Novel Microstrip Slow-wave Open-loop Resonator Filters,' *IEEE Transactions on MTT*, vol. 45, no. 12, pp. 2358-2665, 1997.

[22] Hong J. S. and Lancaster M. J., 'Cross-coupled Microstrip Hairpin-resonator Filters,' *IEEE Transactions on MTT*, vol. 46, no. 1, pp. 118-122, 1998.

[23] Shang X., Wang, Y., Nicholson, G. L. and Lancaster, M. J., 'Design of multiple-passband filters using coupling matrix optimisation,' *IET Microw. Antennas Propag.*, vol. 6, iss. 1, pp. 24-30, 2012.

[24] Skaik T., Lancaster M. J., Ke M. and Wang Y., 'A Micromachined WR-3 band Waveguide Diplexer based on Coupled Resonator Structures,' *Proceedings of the 41st European Microwave Conference (EuMA)*, pp. 770-774, 2011.

[25] Tseng C. H., Chen C. J., Chu T. H., 'A Low Cost Switched-Beam Patch Antenna Array with Butler Matrix Network,' *IEEE antenna and wireless propagation letters*, vol. 7, pp. 432-435, 2008.

[26] Murad N. A., Lancaster M. J., Wang Y., Ke M., 'Micromachined Millimetre-Wave Butler Matrix with Patch Antenna Array,' *Microwave Symposium (MMS)*, pp. 1-4, 2009.

[27] Wang Y., Ke M., Lancaster M. J., 'A Ka-Band Butler Matrix with Antenna Array Based On Micromachined Rectangular Coaxial Structures,' *Proceedings of the 39th European Microwave Conference (EuMA)*, pp. 739-742, 2009.

[28] Mongia R., Bahl I., Bhartia P., *RF and Microwave Coupled-Line Circuits*, Artech House Microwave Library, 2nd Edition, 1999.

[29] Fusco V. F., *Microwave Circuits Analysis and Computer-Aided design*, Prentice-Hall International, 1987.

[30] Lu Private Communication, to be published in PhD thesis, the University of Birmingham

[31] Caulton M., Hershenov B., Knight S. P., and DeBrecht R. E., 'Status of Lumped Elements in Microwave Integrated Circuits---Present and Future,' *IEEE Transactions on MTT*, vol. 19, no. 7, pp. 588-599, 1971.

[32] Matthaei G. L., Young L., and Jones E. M. T., *Microwave filters, impedance-matching networks, and coupling structures*, Artech House Books, 1980.

[33] Uchida H., Yoneda N., Konishi Y., and Makino S., 'Bandpass Directional Couplers with Electromagnetically-Coupled Resonators,' *IEEE MTT-S International*, pp.1563-1566, 2006.

[34] Russer P., *Electromagnetics Microwave Circuit and Antenna Design for Communications Engineering*, Artech House, Inc., 2003.

[35] Wang Y., Ke M., Lancaster M. J. and Chen J., 'Micromachined 300 GHz SU-8-Based Slotted Waveguide Antenna,' *IEEE Antennas and Wireless Propagation Letters*, vol. 10, pp. 573-576, 2011.

[36] Casanueva A., Pereda J. A., and Mediavilla A., 'Optimum compact H and E-plane corners in rectangular waveguide,' Microwave and Optical Technology Letters, vol. 42, iss. 6, pp. 494-497, 2004.

[37] Skaik T., Wang Y., Ke M., Qian S. and Lancaster M.J., 'A Micromachined Wr-3 Waveguide With Embedded Bends for Direct Flange Connections,' *Proceedings of the 40th European Microwave Conference (EuMA)*, pp.1225-1228, 2000.

[38] Shang X., Ke. M, Wang Y. and Lancaster M.J., 'Micromachined W-band waveguide and filter with two embedded H-plane bends,' *IET Microw. Antennas Propag.* ,vol. 5, iss.3, pp. 334-339, 2011.

[39] Richardson P. N., Lee H. Y., "Design and analysis of slotted waveguide arrays," *Microwave Journal*, pp. 109-125, 1988.

[40] Constantine A. Balanis., *Advanced Engineering Electromagnetics*, John Wiley, Inc., New Jersey, 2nd Edition, January 2012.

[41] Silver S., "Microwave Antenna Theory and Design", Boston Technical Publishers, 1964.

[42] Stevenson A. F., "Theory of slots in rectangular waveguides," *Journal of Applied Physics*, vol. 19, pp. 24-38, 1948.

[43] Bhatti R.A., Park B.Y., Park S.O., "Design of a Planar Slotted Waveguide Array Antenna for X-band Radar Applications", *Journal of The Korean Institute of Electromagnetic Engineering And Science*, vol. 11, no. 2, pp. 97-104, 2011.

[44] Volakis J.L., *Antenna Engineering Handbook*, New York: the McGraw-Hill Company, 4th Edition, 2007.

[45] C. A. Balanis, *Antenna Theory Analysis and Design*, John Wiley, Inc., New Jersey, pp. 299, 2005.

[46] R. Tang, R. W. Bums, "Phased Array" in R. C. Johnson, *Antenna Engineering Handbook*, McGraw Hill, Inc., New York, pp. 20-5, 1993.

[47] Stutzman W.L. and Thiele, G.A., *Antenna theory and design*, John Wiley & Sons, 2nd edition, 1998.

[48] Pozar D.M., and Kaufman B., "Design considerations for low sidelobe microstrip arrays", *IEEE Trans. Antennas Propag*., AP-38, pp. 1176–1185, 1990.

[49] Hodjat F. and S. Hovanessian, "Nonuniformly spaced linear and planar array antennas for sidelobe reduction", *IEEE Transactions on Antennas and Propagation*, vol. 26, no. 2, pp.198-204, 1978.

[50] Hirokawa, J., Ando, M., "Sidelobe Suppression in 76-GHz Post-Wall Waveguide-Fed Parallel-Plate Slot Arrays", *IEEE Transactions On Antennas And Propagation*, vol. 48, no. 11, November 2000.

Appendix: Publications

WR-3 Band Butler Matrix Design Using SU-8 Photo-Resist Technology

Shuli Li, Shani Lu, Michael J. Lancaster
School of Electronic, Electrical and Computer Engineering, The University of Birmingham, U.K.

Abstract
A design of WR-3 band 2x2 Butler Matrix feeding a 2-element slotted waveguide antenna array is presented in this paper. The whole design is based on an SU-8 multi-layer structure, which is expected to be fabricated by metal-coated SU-8 thick resist technology [1]. Each layer of the SU-8 wafer has a thickness of 0.432mm, which matches the narrow-wall height of a WR-3 (220-325GHz) waveguide. To examine the performance of the proposed Matrix, prior to adding antennas, a simulation on the 90 degree resonator based hybrid coupler was carried out using the CST Microwave Studio [2]. The simulation results agree well with the theoretical predictions, validating the proposed design.

I. Introduction

The Butler Matrix is a very attractive beamforming system due to its ability to form orthogonal beams in a simple design. This system can limit the interference of signals in order to increase the channel capacity of communication systems [3].Conventional planar structure microstrip Butler Matrices have been demonstrated [4-5]. As the development of high performance millimeter wave and sub-millimeter wave components and systems, terahertz micromachined circuits have been increasingly utilized [6]. A schematic diagram of the WR-3 band 2x2 Butler Matrix is shown in Fig1. (a). This whole structure is constructed by one 90 degree hybrid coupler and a 2-element slotted waveguide antenna array. This Butler Matrix can be extended to a 2^nx2^n Butler Matrix by increasing the number of 90 degree hybrid couplers and crossovers. The whole structure is to be fabricated on metal-coated SU-8 thick resist and is designed to be built by three layers of SU-8. Such an assembly for the Butler Matrix is illustrated in Fig.1 (b). The antenna has been realized by slotted waveguide antenna array. This antenna array structure has two elements that are spaced by λ_0 at 270GHz in order to fit the WR-3 band waveguide dimensions and get orthogonal beams at the same time. The coupler is shown in Fig1. (b) and is based on four resonators coupled together.

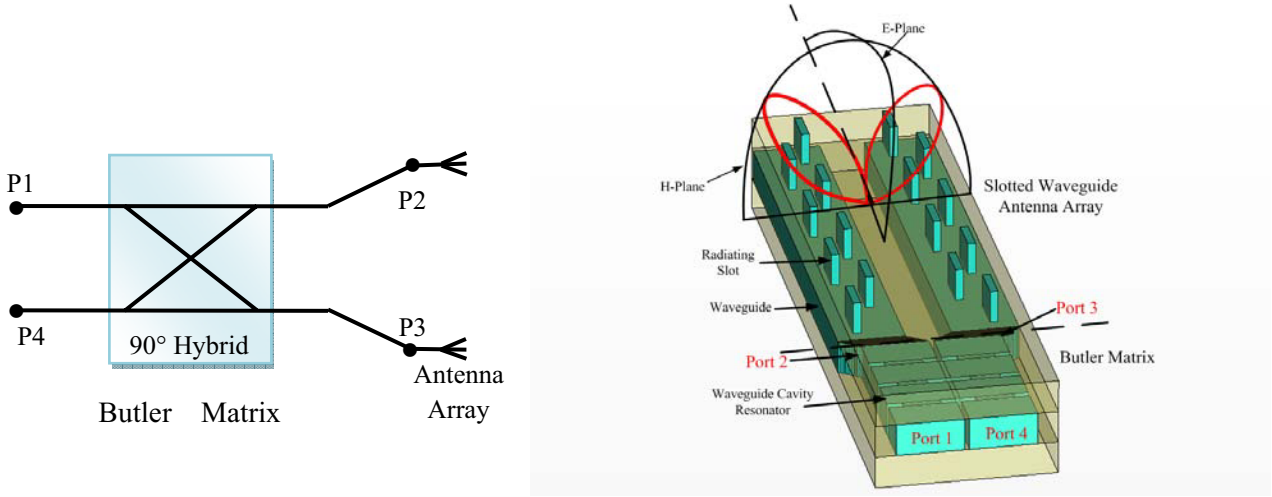

(a) (b)

Fig1. (a) Schematic Diagram for a 2x2 Butler Matrix (b) Assembly of the 2x2 Butler Matrix feeding a 2-element Slotted Waveguide Antenna Array

II. Resonator Design

The 90 degree hybrid coupler in this design is based on waveguide cavity resonators. It is developed from the conventional branch-line coupler as shown in Fig.2, which consists of two quarter-wavelength transmission line sections of characteristic impedance Z_{01}.The two transmission line sections are connected by two shunt branches, which are both quarter-wavelength transmission lines of characteristic impedance Z_{02} at both ends. The branch-line coupler has four ports with the terminal impedance Z_0. By properly choosing the values of Z_{01} and Z_{02} asZ_{01}=0.707Z_0 and Z_{02}=Z_0 separately, this circuit can operate as a 90 degree hybrid coupler with equal power split at ports 2 and 3 [7].

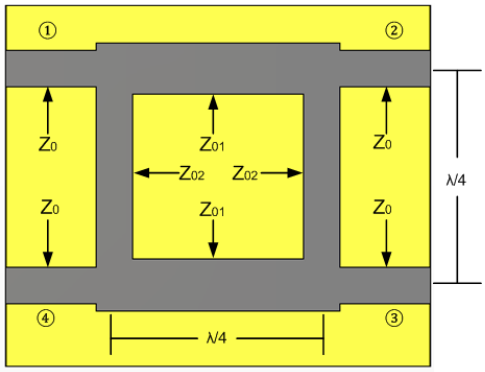

Fig.2 Branch-line Directional Coupler in Microstrip

To implement the resonator based 90 degree hybrid coupler, four resonators with appropriate couplings between each other are introduced [8]. The correct external quality factor (Qe) between ports and resonators also need to be taken into consideration. The topology of this hybrid coupler is shown in Fig.3, as circles of this represent the resonators, while the couplings are depicted by the lines between the circles.

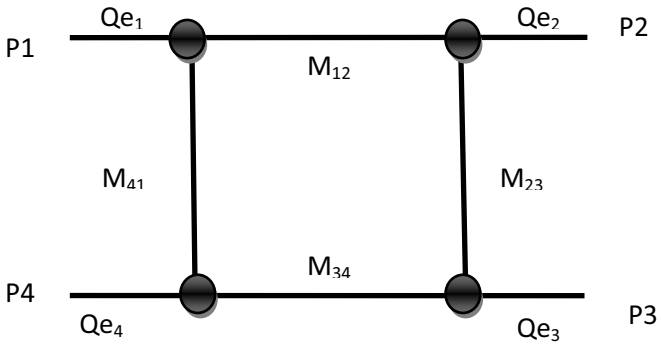

Fig.3 Topology of the Coupled Resonator 90 Degree Hybrid Coupler

For a 90 degree hybrid coupler with a center frequency of 270GHz, and a fractional bandwidth (FBW) of 0.05, the coupling matrix and external quality factors can be calculated as [8-9]:

$$[M]=\begin{bmatrix} M_{11} & M_{12} & M_{13} & M_{14} \\ M_{21} & M_{22} & M_{23} & M_{24} \\ M_{31} & M_{32} & M_{33} & M_{34} \\ M_{41} & M_{42} & M_{43} & M_{44} \end{bmatrix}=\begin{bmatrix} 0 & 0.0707 & 0 & 0.05 \\ 0.0707 & 0 & 0.05 & 0 \\ 0 & 0.05 & 0 & 0.0707 \\ 0.05 & 0 & 0.0707 & 0 \end{bmatrix}$$

$$Q_{e1}=Q_{e2}=Q_{e3}=Q_{e4}=20$$

Fig.4 (a) shows the frequency response of this 90 degree hybrid coupler with the center frequency 270GHz, and FBW=0.05. Fig4. (b) is the phase difference between port2 and port3, it is 90 degree at the center frequency.

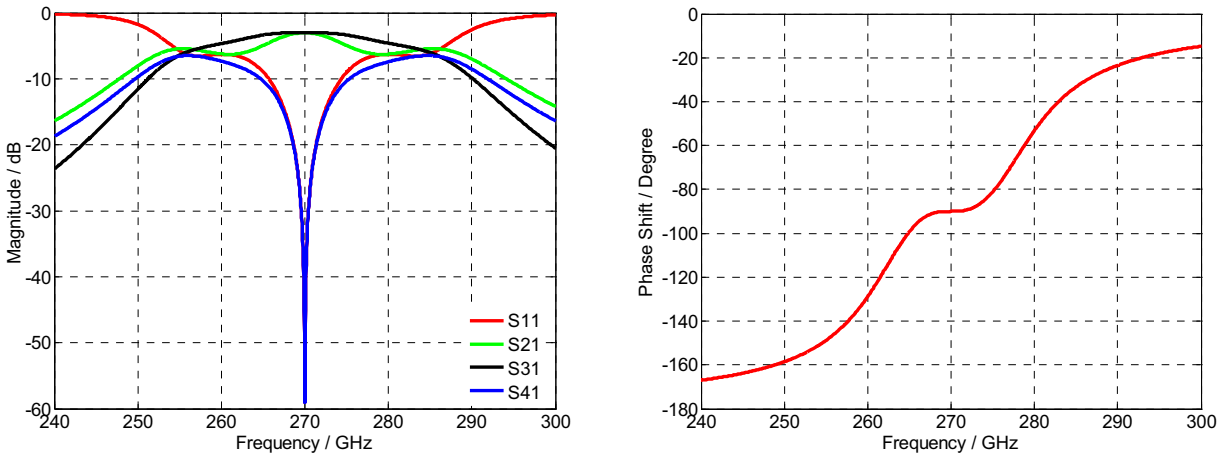

(a) (b)

Fig4. (a) Frequency Response of Magnitude for the 90 Degree Hybrid Coupler calculated from coupling matrix. (b) Frequency Response of Phase Shift Between S21 and S31 for the 90 Degree Hybrid Coupler

III. Waveguide Design

This 90 degree hybrid coupler is implemented by cavity resonators [8], each with a length of half guided wavelength [10], the design has been tailored to suit a simple fabrication for the SU-8 photo-resist technology, for this WR-3 band hybrid coupler, it is constructed by only one layer of SU-8 wafer with a thickness of 0.432mm as shown in Fig.5. The main dimensions for the structure are illustrated in Table 1.

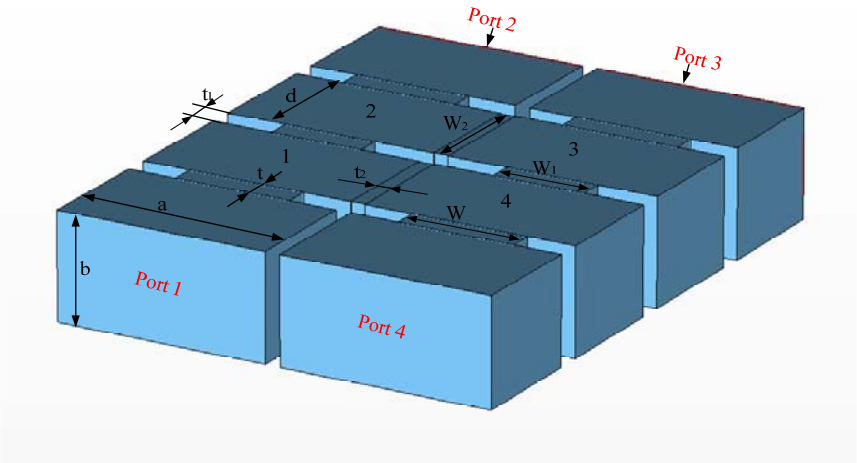

Fig.5 90 Degree Hybrid Coupler with Coupled Waveguide Cavity Resonators

Waveguide Dimensions	a x b	0.864mm x 0.432mm
Waveguide Cavity Resonator Length	d	0.495mm
Aperture Between Port and Resonator	W x t	0.475mm x 0.100mm
Aperture Between Resonator 1 and 2	W_1 x t_1	0.375mm x 0.100mm
Aperture Between Resonator 2 and 3	W_2 x t_2	0.485mm x 0.060mm

Table 1 Summary of Main Design Dimensions

The optimised frequency response simulated by CST Microwave Studio (as shown in Fig.6 (a) by dashed lines) is compared with the response calculated by the coupling matrix mentioned in Part II. It can be noted that the isolation between two output ports is -22.35dB, and the return loss (RL) is also larger than -30 dB. We can further optimize the design to get better RL and isolation, but this will degrade the responses of S21 and S31 to an extent that they cannot both get to exactly –3dB at the center frequency. Fig.6 (b) is comparison of phase difference between port 2 and port 3. From these two figures, the simulation results agree well with the theoretical calculation. The signal fed into port 1 is divided equally at port 2 and port 3 with a phase different of 90 degree.

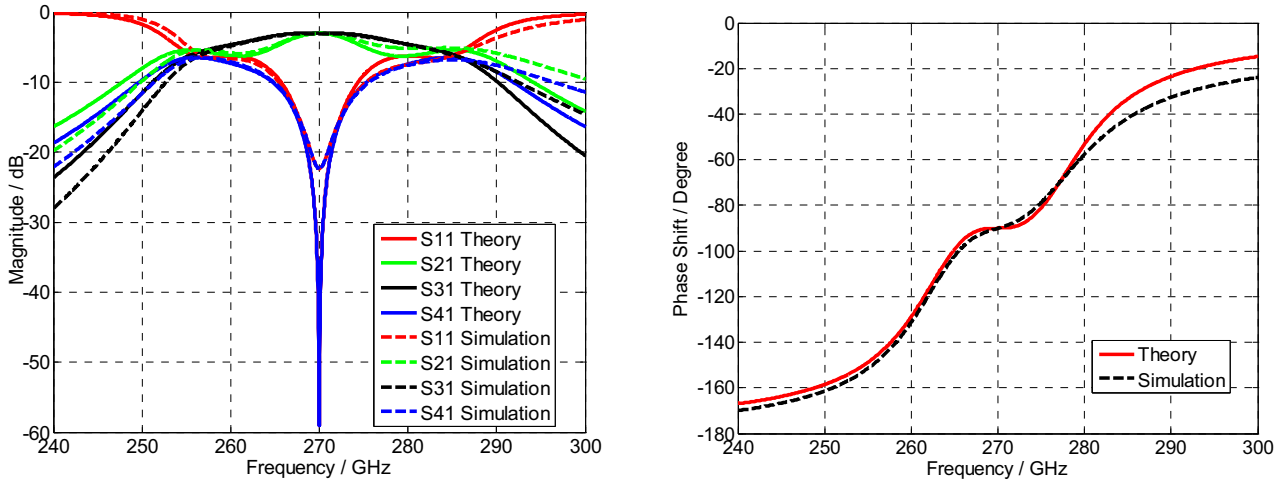

(a) (b)

Fig.6 (a) Comparison of Frequency Response for the 90 Degree Hybrid Coupler with Coupled Waveguide Cavity Resonators (b) Comparison of Phase Shift between S21 and S31 for the 90 Degree Hybrid Coupler Coupled Waveguide Cavity Resonators

IV. Future Work and Conclusion

In this paper, the idea of a WR-3 band Butler Matrix constructed by a resonator-based 90 degree hybrid coupler feeding a 2-element slotted waveguide antenna array has been implemented. All the structure is built on multi-layers and is tailored to suit the SU-8 photo-resist technology. The simulated results agree well with the theoretical calculation, which will lead to a more accurate measurement result after construction. The optimization of the 8-slot waveguide antenna will continue. Theoretical predictions of radiation patterns will be predicted in order to compare with the optimization result by CST. Experimental measurements will be carried out on this system, and the obtained results will be presented and discussed in the future.

References

[1] Jiang K, Lancaster MJ, Llamas-Garro I , "SU-8 Ka-band filter and its microfabrication", *et al. Journal of Micromechanics and Mocrpengineering*, vol. 15, pp.1522-1526, Aug.2005

[2]CST Microwave Studio Germany, CST GmbH, 2006

[3] Ming-Ju Ho, Stuber,G.L., Austin, M.D., "Performance of switched-beam smart antennas for cellular radio systems" , *IEEE Trans. Veh. Technol.*, vol.47, no. 1, pp. 10-19, Feb. 1998

[4]Denidni,T.A., Libar, T.E., "Wide band four-port butler matrix for switched multibeam antenna arrays", *IEEE Proc. PIMRC 2003*, vol. 3, pp. 2461-2464, Sep.2003

[5] C.Tseng, C.Chen, T.Chu, "A Low-Cost 60-GHz Switched-Beam Patch Antenna Array With Butler Matrix Network", *IEEE Antennas Wirless Propag. Lett.*, vol. 7, pp. 432-435, 2008

[6] I. Llamas-Garro, A. Corona-Chavez, "Micomachined Transmission Lines for Millimetre-wave Applications", *2006 Int. Conf. on Electronics, Communications and Computers*, pp. 15, Feb. 2006

[7]Rajesh Mongia, Inder Bahl , Prakash Bhartia, "RF and Microwave Coupled-Line Circuits", Artech House Microwave Library, 2nd Edition, May. 1999

[8] Lu Private Communication, to be published in PhD thesis, the University of Birmingham

[9]Hong, J., and Lancaster, M.J.: "Microstrip Filters for RF/Microwave Applications", John Wiley & Sons, Inc, 2001

[10] Robert S. Elliott, "An introduction to Guided Waves and Microwave Circuits". Prentice-Hall International Editions, 1993

WR-3 Band Butler Matrix Design Fabricated with SU-8 Photo-Resist Technology

Shuli Li, Shani Lu, Michael J. Lancaster

School of Electronic, Electrical and Computer Engineering
The University of Birmingham

Introduction

- The Butler Matrix is a beamforming system able to form orthogonal beams which is highly used in communication systems.
- Due to the development of terahertz micromachined circuits, a WR-3 Band (220-325 GHz) Butler matrix feeding a 2-element slotted waveguide antenna array is designed.

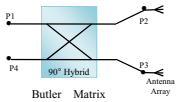

Schematic Diagram

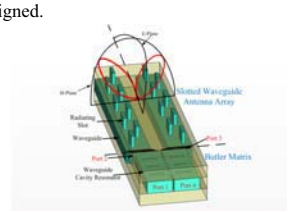

Assembly of the Butler Matrix Feeding antenna array

Design Procedure

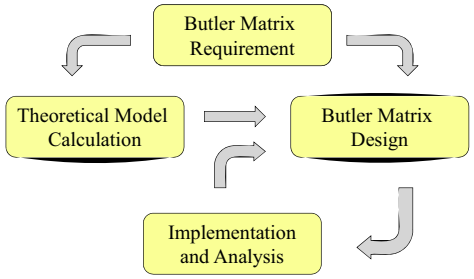

Design Procedure

Butler Matrix Requirements

- 2x2 Butler Matrix feeding a 2-element slotted waveguide antenna array.
- The Butler Matrix is constructed by a 90 degree hybrid coupler, which is based on waveguide cavity resonators.
- The Butler Matrix is designed in the WR-3 Band (220 GHz-325 GHz), with a centre frequency of 270 GHz and will be fabricated with SU-8 Photo-Resist Technology.

Design Procedure

Theoretical Model Calculation

The whole structure is constructed by a 90 degree hybrid coupler, which is based on waveguide cavity resonators.

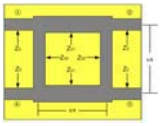

Conventional Branch-line Directional Coupler in Microstrip

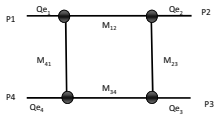

Topology of the Coupled Resonator 90 Degree Hybrid Coupler

Design Procedure

Theoretical Model Calculation

$$[M] = \begin{bmatrix} 0 & 0.0707 & 0 & 0.05 \\ 0.0707 & 0 & 0.05 & 0 \\ 0 & 0.05 & 0 & 0.0707 \\ 0.05 & 0 & 0.0707 & 0 \end{bmatrix} \quad Q_{e1}=Q_{e2}=Q_{e3}=Q_{e4}=20$$

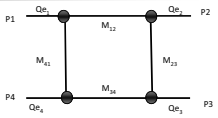

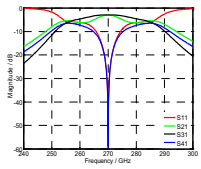

Frequency Response of Magnitude for the 90 Degree Hybrid Coupler

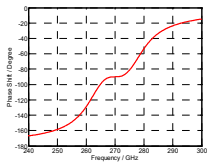

Frequency Response of Phase Shift Between S21 and S31 for the 90 Degree Hybrid Coupler

Design Procedure

Butler Matrix Design

The 90 degree hybrid coupler is implemented by cavity resonators and the design has been tailored to suit a fabrication for the SU-8 photo-resist technology.

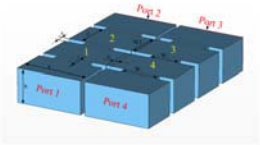

Waveguide Dimensions	a x b	0.864mm x 0.432mm
Waveguide Cavity Resonator Length	d	0.495mm
Aperture Between Port and Resonator	W x t	0.475mm x 0.100mm
Aperture Between Resonator 1 and 2	W_1 x t_1	0.375mm x 0.100mm
Aperture Between Resonator 2 and 3	W_2 x t_2	0.485mm x 0.060mm

Design Procedure

Implementation and Analysis

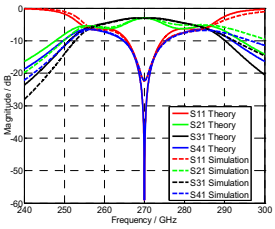

Comparison of Frequency Response for the 90 Degree Hybrid Coupler with Coupled Waveguide Cavity Resonators

- The simulation results agree well with the theoretical predictions.
- The S21 and S31 both reach the magnitude of –3 dB at the centre frequency (270 GHz).
- The return loss (S11) is larger than -30 dB, we can further optimize the design to get better S11, but will degrade the responses of S21 and S31.

Design Procedure

Implementation and Analysis

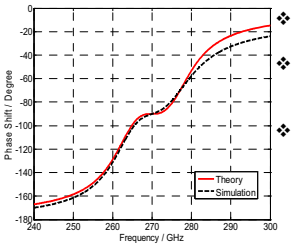

Comparison of Phase Shift between S21 and S31 for the 90 Degree Hybrid Coupler Coupled Waveguide Cavity Resonators

- The simulation results agree well with the theoretical calculation.
- The phase shift between port 2 and port 3 is exactly 90 degree at the centre frequency (270 GHz).
- The signal fed into port 1 is divided equally at port 2 and port 3 with a phase shift of 90 degree.

Future Work

- The Butler Matrix constructed by a resonator-based 90 degree hybrid coupler has been designed and the simulated results agree well with the theoretical calculation which will lead to a more accurate measurement result after construction.
- The optimization of the 90 degree hybrid coupler and the slotted waveguide antenna array will be continued.
- The theoretical predictions of radiation patterns of the antenna will be used to compare with the optimization result by CST Microwave Studio.
- Experimental measurements will be performed on this system, and the obtained results will be presented in the future.

Thank You!

SXL971@bham.ac.uk